DIGITAL COMMONS
@ UNIVERSITY OF SOUTH FLORIDA

University of South Florida
Digital Commons @ University of South Florida

USF Tampa Graduate Theses and Dissertations

USF Graduate Theses and Dissertations

February 2020

Microfluidically Reconfigurable Millimeter-Wave Switches, Antenna Arrays and Filters with Fast-Actuation Using Movable Metallized Plates and Integrated Actuation

Enrique J. Gonzalez Carvajal
University of South Florida

Follow this and additional works at: https://digitalcommons.usf.edu/etd

 Part of the Electrical and Computer Engineering Commons

Scholar Commons Citation

Gonzalez Carvajal, Enrique J., "Microfluidically Reconfigurable Millimeter-Wave Switches, Antenna Arrays and Filters with Fast-Actuation Using Movable Metallized Plates and Integrated Actuation" (2020). *USF Tampa Graduate Theses and Dissertations.*
https://digitalcommons.usf.edu/etd/8934

This Dissertation is brought to you for free and open access by the USF Graduate Theses and Dissertations at Digital Commons @ University of South Florida. It has been accepted for inclusion in USF Tampa Graduate Theses and Dissertations by an authorized administrator of Digital Commons @ University of South Florida. For more information, please contact digitalcommons@usf.edu.

Microfluidically Reconfigurable Millimeter-Wave Switches, Antenna Arrays and Filters with Fast-Actuation Using Movable Metallized Plates and Integrated Actuation

by

Enrique J. González Carvajal

A dissertation submitted in partial fulfillment
of the requirements for the degree of
Doctor in Philosophy in Electrical Engineering
Department of Electrical Engineering
College of Engineering
University of South Florida

Major Professor: Gokhan Mumcu, Ph.D.
Nathan Crane, Ph.D.
Jing Wang, Ph.D.
Thomas Weller, Ph.D.
Jiangfeng Zhou, Ph.D.

Date of Approval:
March 24, 2020

Keywords: integrated actuation, frequency tunability, piezoelectric actuation, microfluidics, power handling

Copyright © 2020, Enrique J. González Carvajal

Dedication

To my mother, sister and Jessica. Thank you for all your love and support.

Acknowledgments

I deeply appreciate all the help provided by my advisor Dr. Gokhan Mumcu for the long hours of discussion and assistance around the research challenges. His guidance throughout my research was extremely valuable to tackle each adversity that presented itself along the road. Similarly, I am extremely grateful to all the hard work that Dr. Weller and Dr. Wang have put over the years into creating and maintaining the WAMI research center. It is thanks to their vision and continuous improvement that I was able to be a part of such an amazing research team. I would also like to thank Dr. Crane and Dr. Zhou for being a significant part of my evaluation committee, their valuable input all but enhances the quality of this work. Special thanks to all the staff at the Nanotechnology Research and Education Center (NREC) at USF; Rich, Rob, Sclafani, thank you. Without their constant work in maintaining and operating the laboratory facilities, it would not have been possible to fabricate all these devices. Furthermore, the time I spent working as a cleanroom assistant at NREC was extremely valuable for me; and NREC staff definitely made me feel like having a second family while being at USF. Finally, I appreciate all the assistance and discussions from the rest of the WAMI research group students. It has been one of the most gratifying life experiences to be a part of such an amazing team.

Table of Contents

List of Tables

List of Figures

Abstract

Microfluidic reconfiguration of microwave devices has emerged as a potentially attractive alternative to integrated semiconductor (ICs/MMICs) and microelectromechanical systems (MEMS) based technologies. On the one hand, MMICs suffer from low power handling capabilities, high IL, non-linear effects, and elevated costs; on the other hand, MEMS are limited by their complex packaging requirements, and relatively low reliability from stiction-based effects. However, microfluidic reconfiguration provides low insertion loss (IL) due to its mechanical nature and it is not limited by power saturation effects. These attributes are especially valuable for applications at mm-waves, potentially reducing costs and increasing power efficiency capabilities. Microfluidic reconfiguration of microwave devices is possible by repositioning a volume of liquid metal or a metallized plate near the component geometry. Initial research within our group introduced microfluidically reconfigurable focal plane arrays (MFPAs) to demonstrate microfluidic beam-steering applications at 30 GHz. The first concept involves a patch antenna that was microfluidically positioned along the focal plane of a lens. However, the total movement for this design is ~40 mm, providing long reconfiguration times. Moreover, available bandwidth was limited by array size due to the use of resonant transmission lines. This dissertation solves these limitations by introducing a metallized plate inside a microfluidic channel and exploiting capacitive coupling effects to produce RF short-circuit conditions. The capacitive coupling is investigated via microfluidically switched microstrip lines that demonstrate RF switching operation from 20 GHz to 40 GHz. The coupling provides low-loss (<0.2 dB) and wideband (~20

GHz) performance. Furthermore, the RF switching concept is implemented in a 30 GHz 8-element MFPA. The MFPA exhibits ~12 GHz bandwidth and reconfiguration time of ~270 ms (as compared to ~1 GHz and 5 s respectively in previous work). Nevertheless, a remaining setback of microfluidic reconfiguration was the need for external micropumps to enable fluid motion. Such pumps are bulky as compared to the microwave components, or hard to integrate within the device. Therefore, miniaturization is necessary to achieve higher reconfiguration speeds and reliable operation. To achieve these goals, this work presents a novel integrated actuation mechanism in the form of piezoelectric bending actuators, eliminating the need for pumps. With the integrated actuation a miniaturized single-pole single-throw microfluidically reconfigurable switch is demonstrated, and it is scalable to single-pole four-throw configurations. The miniaturized switch performs with low losses (i.e. ~ 0.7 dB) and wide bandwidth (i.e. >20 GHz). The integrated actuation allows for reconfiguration speed and reliability tests that were not possible before with external micropumps. Experiments demonstrated reconfiguration times of 1.1 ms and reliable operation of the device over 3 million cycles. Moreover, the switch is expected to handle up to 30 W of continuous RF power, with experimental verification performed up to 2 W at 32 GHz. Successful realization of this compact actuation mechanism provided a path for mm-wave microfluidically reconfigurable filters with improved reconfiguration speeds and integrated microfluidic actuation. Specifically, a microfluidically reconfigurable bandpass filter that exhibits relatively low loss (i.e. up to 3.1 dB), reconfiguration speeds of 285 ms/MHz, and reliable operation up to 12 million cycles is demonstrated. The filter is reconfigurable both in frequency (from 38 GHz down to 28 GHz) and bandwidth (from 7.6% up to 16.8%) and is expected to handle up to 5 W of continuous RF power.

Chapter 1: Motivation

Bandwidth limitations, a crowded frequency spectrum, and an increased market for electronic devices have created the need for wireless systems operating at millimeter-wave (mm-wave) frequencies. However, radio frequency (RF) signal transmission/detection at these wavelengths introduces challenges due to increased effects of diffraction, attenuation and material non-linearity. Therefore, efficient technologies that provide a solution to these problems are highly desirable and greatly needed.

Specific hardware that helps mitigate these issues are beam steering antenna arrays. Similarly, reconfigurable filters provide a solution to interference and non-linearity issues that become detrimental at these wavelengths. Common technologies used to design such hardware rely upon the use of semiconductors in the form of RF integrated circuits (RFICs), monolithic microwave integrated circuits (MMICs), RF silicon over insulator (RF SOI); or through micro-scale mechanical actuation in micro electro-mechanical systems (MEMS). Yet, both semiconductors and MEMS require the assessment of different trade-offs. On the one hand, semiconductor technology has the advantage of mass scale manufacturing techniques and benefits from fast reconfiguration speeds (i.e., tenths of ns or less), making it a widely popular and attractive solution for beam-steering applications [1-3]. Still, semiconductors suffer from non-linear effects and material limitations that lead to higher losses and low power handling as frequency increases [4]. On the other hand, MEMS technology offers improvements due to its micro-scale mechanical actuation mechanisms (i.e., high efficiency and low loss) [5], but it presents stiction related effects

that limit device reliability and slower reconfiguration times as compared to semiconductors [6]. Furthermore, both technologies need additional design considerations such as additional RF components and/or DC bias/control lines that further increase costs and limit design flexibility. All these limitations become more prominent as the device's operating frequency increases, especially close to and above mm-wave bands. Macro-scale mechanical beam-steering solutions have been introduced as well as an alternative to electronic scanning of semiconductors or MEMS. These solutions involve the integration of actuators that spatially re-position the antenna by utilizing gimbaled assemblies [7, 8], and yet, this results in bulky structures and considerably slow reconfiguration times. To address these problems, this dissertation focuses on investigating a promising novel alternative that potentially solves the loss, costs, power handling and design complexity problems faced by current state-of-the-art mm-wave devices. Specifically, a solution can be found by using the concept of microfluidic technology to provide reconfiguration of beam-steering antenna arrays and filters.

Microfluidic loading of RF devices has emerged as a low-cost, all-passive and versatile technology alternative for component reconfiguration by offering relatively cheap base materials, highly linear behavior and potentially high-power handling capabilities [9]. The concept of microfluidic reconfiguration of RF devices is to utilize fluidic channel walls that contain a dielectric and/or conductive material, which in turn loads (or modifies) the RF component geometry. Several devices such as filters [10-12], antennas [13, 14], antenna arrays [15, 16] and switches [17-20], already proved the feasibility of microfluidic reconfiguration of RF components by utilizing some form of liquid metal (e.g., mercury or Galinstan). However, the long-term use of liquid metals presents major drawbacks such as health/environmental risks and oxidization; limiting the applicability of liquid metal loaded RF devices [21]. Additionally, recent literature has

shown limited uses of liquid-metal to no more than 15 GHz for loaded antennas [22] and to 26 GHz for switches in waveguide applications [23]. To address the limitations imposed by liquid metals, our group has proposed the introduction of metallized plates inside microfluidic channels [24]. Different components such as reconfigurable filters [25] and antennas [26] have been demonstrated using the metallized plate approach. By taking advantage of standard PCB photo-lithography it is possible to design selective metallization patterns on these moving plates, thus providing extra degrees of freedom on component design [14, 25]. Reconfigurable antennas and filters utilizing the selectively metallized plate (SMP) approach have proven to provide high power capabilities for antennas [26] and filters [27].

Promising advances in beam-steering applications of microfluidic reconfiguration at mm-waves have also been done by our group through recent publications. Specifically, by introducing microfluidic based focal plane arrays (MFPAs) in [16]. The initial MFPA design offered beam-steering capabilities without the need of active RF devices, potentially reducing costs and providing higher efficiency performance. The MFPA concept of [16] was demonstrated by microfluidically positioning a patch antenna at the focal plane of an extended hemispherical dielectric lens. This MFPA performs with low insertion loss (IL) (e.g. IL < 3 dB for an 8-element MFPA) and 5.25 s beam-steering time to cover the ~60° field of view (FoV). As expected, it performs with very low loss as compared to traditional beam-steering implementations. However, a slow reconfiguration time and limited bandwidth was observed as the trade-off.

1.1. Research Goals and Contributions

In this work, the concept of microfluidic switching of microstrip lines utilizing selectively metallized plates (SMPs) at mm-wave frequencies is presented. Specifically, a microfluidically switched microstrip line utilizing the SMP approach is designed and experimentally verified from

15 GHz up to 40 GHz. This demonstrated the potential of this technology to improve switching and bandwidth capabilities of the first generation of MFPAs that relied upon antenna movement instead of feed network switching operations. Then, the design and implementation of a wideband low-loss feed network for a 30 GHz microfluidic focal plane array (MFPA) are given. It will be shown that by introducing a novel, microfluidically switched feed network it is possible to maintain a wideband performance (~38%) and accommodate >32 antenna elements in a 1D 30GHz Ka-band focal plane array setting. In addition, the required microfluidic motion range is significantly reduced (~10x) for higher beam-steering speeds and a compact layout is maintained for enabling realization of 2D MFPAs when compared to previous publications.

To further advance the practical applications of microfluidic technology at mm-waves, low-loss miniature single-pole multi-throw switches are introduced. Additionally, this work provides the first compact piezoelectrically actuated microfluidic device working at mm-waves in one single package. A single-pole single-throw (SPST) switch is used to demonstrate miniaturization capabilities of SMP-based microfluidic devices and implement the piezoelectric actuation mechanism. Experimental results show that wide-band (~20 GHz) and low-loss (<0.3 dB) performance in maintained by the switch. Experiments demonstrated reconfiguration times of 1.12 ms and reliable operation of the device over 3 million cycles. Moreover, the switch is expected to handle up to 15 W of continuous RF power, with experimental verification performed up to 2 W at 32 GHz. Consequently, the SPST switch is expanded into single-pole four-throw (SP4T) configuration and it is included in a beam-forming network to demonstrate beam-steering applications and potentially provide high power-handling capabilities.

Finally, after having successfully integrated the piezoelectric actuation mechanism into a compact microfluidic device, a reconfigurable filter with frequency and bandwidth tuning is

designed at mm-waves. Specifically, a microfluidically reconfigurable bandpass filter with low loss (i.e. up to worst-case 3.1 dB IL), a reconfiguration speed of 285 ms/MHz, and reliable operation up to 12 million cycles is demonstrated. The filter is reconfigurable both in frequency (from 38 GHz down to 28 GHz) and bandwidth (from 6.8% up to 16.8%) and is expected to handle up to 5 W of RF power. All these advances position microfluidic technology for reconfiguration of microwave devices in an advanced terrain enabling faster reconfiguration speeds, the ability of performing reliability and repeatability tests, and provide a solid path for expanding the technology into mm-wave applications.

1.2. Content Outline

This dissertation is organized as follows:

i. Chapter 2 offers a brief review of the state-of-the-art technologies utilized for reconfiguration of microwave devices.

ii. Chapter 3 presents a microfluidically switched microstrip line and the development of its equivalent circuit model. Specifically, a microfluidically switched microstrip line is designed and characterized to exhibit <0.3 dB IL and wideband (>20 GHz) performance.

iii. Chapter 4 implements the microfluidic switching concept via a selectively metallized plate in a microfluidically reconfigurable focal plane array. The switching operation and its equivalent circuit model are employed for designing a feed network for a focal plane array at 30 GHz that performs with 38% bandwidth and low loss. Additionally, the circuit model is used to demonstrate the scalability of the design for antenna arrays with up to 64 elements with no bandwidth performance degradation.

iv. Chapter 5 introduces a miniaturized version of the microfluidically switched microstrip line, along with its expansion to a single-pole four-throw configuration. In addition,

integrated piezoelectric actuation is utilized for the first time in a microfluidically reconfigurable device. The switch performs with 0.3 dB IL, 1.12 ms reconfiguration time, up to 15 GHz bandwidth, and is actuated up to 3 million times with no noticeable degradation in performance. Furthermore, the switch is expanded into a single-pole multi-throw operation. Specifically, a single-pole four-throw switch is designed and experimentally verified to provide <0.9 dB IL while maintaining the wideband performance (i.e. >18 GHz bandwidth) as the SPST. The SP4T is then implemented into a compact beam-steering array design within a 4×4 Butler matrix beam-forming network.

v. Chapter 6 describes the application of integrated piezoelectric actuation into the first bandwidth and frequency reconfigurable bandpass filter at mm-wave frequencies. Specifically, a band pass filter with independent frequency and bandwidth tuning capabilities is designed at mm-wave frequencies. The filter can be reconfigured from 38 GHz initially, down to 28 GHz, and its bandwidth can be increased from 6.8% up to 16.8% at 38 GHz and from 7.6% up to 12.8% at 28 GHz. This bandpass filter implementation represents the first application of microfluidic reconfiguration for a filter at mm-wave frequencies.

vi. Chapter 7 offers the final remarks or this dissertation.

Chapter 2: Review of Reconfigurable RF/Microwave Devices

Recent advances in wireless communications requirements has generated a greater need for faster data rates, increased bandwidths for high data throughput between devices, and components that perform efficiently and provide multiple functionalities. These features demand reconfigurable microwave devices that are able to operate with advanced performance at multiple frequencies, and that have the capability to re-direct its electromagnetic energy towards specific/multiple locations [28]. These types of reconfigurable devices are required to exhibit:

- ➡ Dynamic reconfiguration with the minimum possible number of additional components.
- ➡ Seamless operation either through a diverse range of frequencies allocated next to each other or in different non-continuous frequency bands.
- ➡ Maintain or improve their performance after reconfiguration.
- ➡ Achieve a satisfactory change between states in the shortest amount of time.

This translates in devices that can provide frequency reconfiguration, dynamic redirection of their electromagnetic energy, improved/adjusted performance via feedback control (e.g. temperature change compensation), seamless switching (ON/OFF) operations, and dynamic signal phase change; to name a few of the required features. All of this, while offering small unified packaging, exhibiting low-loss (i.e. high efficiency) performance, and being able to handle high amounts of electrical power.

Several methods have been proposed, investigated and characterized to present solutions to the reconfiguration challenge. Among these, one can mention the physical modification of a

device's structure via mechanical actuation, the use of semi-conductor (SC) and integrated circuits (IC) elements [29], micro-scaled mechanical techniques making use of micro electro-mechanical systems (MEMS) components [30] and –more recently– the introduction of hydraulic actuation in fluids that modify device characteristics [21]. To this extent, it is possible to group these solutions in two main classes:

- ➡ Active electronic reconfiguration, i.e. the use of SC technology to provide an electronic input and modify an electrical variable.
- ➡ Mechanical (passive) reconfiguration, by introducing mechanical actuation to modify a passive electrical component through mechanical or electrical inputs.

Between the suggested methods, the most popular to-date is the use of active electronics to realize switching or loading mechanisms. With the caveats of added design complexity, extra components, increased power consumption and non-linear behavior in the microwave device (μWD) response. By utilizing IC technology, it is possible not only to achieve extremely fast reconfiguration speeds (i.e. tenths of ns), but also to offer unified packaging, scalability and have a single connection interface for signals and control in a compact chip. Due to the development of advanced fabrication techniques that made monolithic microwave integrated circuits (MMICs) relatively cost-effective and more reliable, it is possible to have mostly all the μWD 's components integrated into a single package. With all these advancements, IC/MMIC technology has proven to be dependable in the design of switches [31-34], active electronically scanned arrays (AESA) [35, 36], tunable frequency selective surfaces (FSS) [37] that can be used as reflectors/absorbers, among other applications.

It is possible now to design a complete TX/RX element (up/down converter, amplifier, filters and antenna) for an AESA radar in a single chip, needing only biasing voltage for the DC

part and, an intermediate frequency (IF) input/output and an external local oscillator (LO) signal on the RF side [38]. However, in the realm of mm-wave frequencies, low output impedances that limit matching capabilities, considerably high insertion loss (IL), reduced antenna efficiency (i.e. $\eta < \sim 35\%$), non-linearities and extremely high testing costs are the main drawbacks in the realization of these fully integrated chips [39-41]. Even though efforts are being made to bring the manufacturing and testing costs down and increase their power efficiency.

Passive reconfiguration is the alternative that has none of the added problems of the active method (i.e. reduced power consumption, highly linear behavior and simpler design) at the cost of slower response times (from tenths of ms to tenths of μs), and up until a few years ago, reduced scalability and device integration [42]. The development of MEMS actuator devices (micro-scaled mechanical components that benefit from the micro-fabrication process utilized in IC technology) introduced linear and highly power efficient elements that could do the same operations –although at a slower speed– performed by most of their electronic counterparts, while having the possibility to provide component integration [43]. The use of MEMS has been proven feasible on designing RF switches [39, 44-46], antennas and phased arrays [47, 48], and reconfigurable FSS [49], to name a few applications. However, problems on: operation reliability, device packaging and the high voltage range sometimes needed to provide actuation; added to the improvements achieved in SC technology with silicon on insulator (SOI) and silicon on sapphire (SOS), have held back the full adoption of MEMS devices (despite their low IL and high linearity as compared to SCs) as a replacement for active-non-linear components [40, 43]. Thus, it is important to offer an overview on the current state-of-the-art of microwave device reconfiguration using active technologies such as RFICs, and passive methods such as MEMS. This will offer additional insight when these technologies are compared to the alternative of microfluidic reconfiguration that is

proposed in this dissertation. Specifically, current methods for developing RF switches and beam steering arrays will be discussed.

2.1. State of the Art of Reconfigurable Microwave Devices Using MMIC and MEMS Technology

Among the most relevant literature to-date related to active reconfiguration of microwave devices, the designs proposed by Rebeiz *et al.* in their different publications present themselves as the most viable approaches when unified packaging is desired [50]. Besides their research, one can find published literature that spans across the fields of MMIC and MEMS, and in some cases, hybrids between both [42, 51]. These publications have repeatedly demonstrated the possibility of providing complete device functionality in one package, such as complete transmit/receive units with integrated up/down conversion, filtering, amplifying and antenna elements. Since the work done in this area is extensive, only the most recent and relevant publications that have demonstrated significant advances on MMIC and MEMS applied for switches, antenna arrays and filters will be discussed. However, it is worth mentioning that for many MMIC applications, most of the operational principles of reconfigurable devices rely on one of the most basic actuator components in electrical engineering: the switch. Per its simplest definition, a switch is a device that makes or breaks and electrical connection; and the way to achieve that effect at microwave frequencies has been a matter of research for many years.

2.1.1. Active Electronic Switching of RF Signals

Due to the nature of high-frequency harmonic signals (i.e. electromagnetic coupling between nearby, non-touching conductors), a mechanical disconnection between two conductive materials does not guarantee a satisfactory open-circuit condition. Thus, achieving ON and OFF

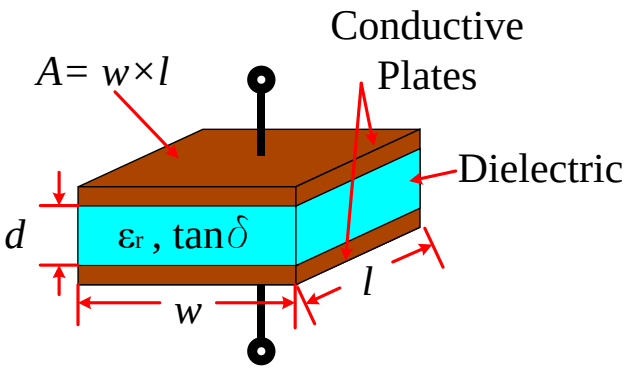

Figure 2.1. Parallel plate capacitor representation.

states in RF devices needs to be studied from the perspective of electromagnetic interaction of charges between the two conductive surfaces.

A simple way to represent an RF switch is by studying its inherent capacitance. One can investigate the electrostatic field between two conductive surfaces (let us call them 1 and 2) of area A and separated a distance d by a dielectric material of relative permittivity ε_r (as seen in Figure 2.1), that have superficial charge distribution ρ_s and, find the electric potential between the two as [52]:

$$V_{12} = -\int_{l=0}^{d} \bar{E} \cdot \bar{dl} \tag{2.1}$$

If one considers the solution of Equation 2.1 by neglecting fringing fields at the plate edges and then finds the ratio from the net amount of stored charge between the plates (Q) and the electric potential (V_{12}), it can be proved that the capacitance (C), can be defined as:

$$C = \frac{\varepsilon A}{d}$$

This result is known as the capacitance of a parallel plate capacitor [52]. Now, since the impedance for a capacitive load Z_c changes with frequency by the form:

$$Z_c = \frac{1}{j\omega C}$$

For any given frequency, it is possible to design a capacitive load with high enough impedance to be considered an open-circuit (i.e. small capacitance) or low enough to be considered a short-circuit (i.e. large capacitance). This is possible by designing for a certain dielectric constant or by modifying the component geometry. This approach allows for modeling RF switches through equivalent capacitive loads and gives additional insight on the limitations of SC devices –that is, the frequency dependent impedances affect device performance as frequency increases[1].

2.1.2. PIN Diodes

A simple way to realize a controllable capacitance (and with it an RF switch) is through a diode. A PIN diode can be forward biased to achieve conduction (ON state) or it can be reversed biased to prevent it (OFF state), thus by placing such component in either a series or parallel configuration, it is possible to form a single-pole, single-throw RF switch [53]. Its behavior can be studied from an equivalent circuit model which contains the equivalent impedance of the diode in either state. When ON, the diode impedance can be represented as

$$Z_{dON} = R_{ON} + j\omega L_i$$

and when OFF, diode impedance can be written as

$$Z_{dOFF} = R_{OFF} + j\left(\omega L_i - \frac{1}{\omega C_j}\right)$$

where the inductance L_i and the capacitance C_j model the parasitic behavior at the junction in the semi-conductive material. Observing that the equivalent impedance for a diode is frequency dependent, and its underlying relation to the material behavior of the component, helps to understand the limitations of SC technology when it comes to RF device design and to infer which

[1] For an in-depth discussion on these topics the reader can refer to [52, 53].

are the parameters that ultimately affect diode performance at microwave frequencies (i.e. inherent inductive and capacitive effects present at the diode junction).This capacitive behavior of the diode can be advantageous when one considers that by reverse biasing this component, conduction of current is prevented. This implies electrical charge build-up at the SC junction and results in the possibility of designing a voltage-controlled capacitor by modifying the bias voltage applied to the diode. However, it is important to mention that the simplified model and explanation offered earlier are considering, for simplicity, a linear behavior for the diode. Since diode current behaves in a non-linear fashion (which in turn means a non-linear diode impedance), these types of devices carry an inherent limitation on the amount of power they can handle. The higher the RF power transmitted through the diode, the stronger the non-linear effects will be. These effects mostly translate to charge saturation within the devices, which means limits on transmitted power and sometimes breakdown of the diode substrate material. Trying to mitigate these effects have led to a wide range of RF switch designs. In practice, transistors are cascaded in several configurations to realize more efficient, faster, wideband and reliable RF switches. But they are still governed by the same material and non-linear restrictions as the simple PIN diode.

2.1.3. Current RF/Microwave Switching Technology

An MMIC device with 0.25 μm GaN HEMT technology was recently proposed by Kaleem *et al.* in [54]. They report a 40 dBm $P_{1\mathrm{dB}}$ compression point at 20 GHz, isolation above 28 dB and IL <1 dB for a 17 to 22 GHz band. It is worth noting the return loss at just 10 dB values across most of the band, highlighting the matching limitation of SC devices.

Howell *et al.* have presented a new approach that offers reduced losses and improved bandwidth for SC-based RF switches [32, 55]. They report a design that allows formation of multiple parallel current paths on a field effect transistor (FET) channel. By this method, it seems

possible to decrease the ON resistance of the RF switch while limiting the impact on the OFF capacitance. The median ON resistance measured by this group is 0.38 Ω-mm and an OFF capacitance of 0.21 pF/mm. This translates to switch performance of <0.3 dB IL and >30 dB isolation, cut-off frequency of 2 THz and response time faster than 100 ns. All this while being able to handle over 10 W at 10 GHz without presenting compression.

In other work, Cho *et al.* introduced a wideband active double-pole double-throw (DPDT) switch for applications from 2 through 22 GHz [34]. The interesting approach taken by this group is the introduction of gain in the ON state of the switch. However, this seems to come with the cost of reduced return loss since they report a measured figure of 9 dB in the operation band. Measured isolation is over 15 dB and output $P_{1\mathrm{dB}}$ at -6.2 dBm.

2.1.4. Active Phased-Arrays

MMIC technology has allowed for unified chip integration of RF devices, although elevated costs, unique requirements in each design and non-linear behavior keep limiting this technology. Major advancements have been made in this field and some of the most recent designs are proposing an aggressive approach with a full system-on-chip integration.

Kang *et al.* present a single-element and four-element phased arrays that are capable to operate at both transmit and receive mode with 5-bit phase and amplitude control [56]. They utilize a 4:1 power combining/dividing network along with amplifying and phase shifting stages, all integrated in one chip. These arrays perform with an average gain of 0 dB per channel along with a noise figure of 9 dB. In receiving mode, they present a $P_{1\mathrm{dB}}$ of -16 dBm per channel and third-order intercept of -5.9 dBm while consuming 142 mW, and in transmission mode the output $P_{1\mathrm{dB}}$ is between 4 to 5 dBm across the 35-36 GHz band with 171 mW power consumption.

A single-chip approach by Ku *et al.* in [57] present a 16-element phased array receiver at W-band for automotive radar applications. The SiGe chip is attached to a linear microstrip array by bond wires and results in a 29.3 dB antenna directivity and 18 dB gain at 77-81 GHz [57]. The system presents beam-steering capabilities in a 100° sweep by 1° steps thanks to their integrated phase shifter elements. As a receiver, the chip exhibits 7 dB gain with variable gain amplifiers that compensate gain error vs. phase states when it is matched to a 50 Ω load, while being capable to achieve 22.5 dB for higher load impedances. Overall chip power consumption is 1.2 W in a 5.5×5.8 mm^2 area and the simulated noise figure is 18 dB.

2.1.5. Applications of MEMS Technology on Switching Elements and Beam-Steering Devices

Most of RF MEMS devices have been proven to operate seamlessly from RF to mm-wave frequencies (i.e. 0.1 to 100 GHz) and several studies demonstrated operation with considerably better performance than MMIC components. And even though the adoption of this technology is still lacking, due to several reasons laid out earlier, research groups continue to propose new ideas and innovative designs.

Sterner *et al.* demonstrate through their switching approach [58] the low loss capabilities of MEMS devices by measuring 0.08 dB IL at 20 GHz and isolation above 25 dB for the two-port configuration. For a three-port switch, they show 0.31 dB and 0.68 dB IL at 1 and 10 GHz respectively, with isolation of 43 and 22 dB. The switches are actuated by voltage ranges from 23 to 89 V with negligible power consumption.

Another design presented by Zhu *et al.* in [46], reports operation up to 40 GHz with less than 0.5 dB IL with 22.5 dB isolation. One of the main goals of this project was to offer improved isolation at the OFF state while aiming to reduce the actuation voltage. The authors proposed the use of a bi-directional motion actuator that operates by thermal effects, in a three-state switch

design. Thanks to this electrothermal actuation approach, the drive voltage for the switch is reduced to 0.5 V.

An antenna array design demonstrated in [59] proposed a mm-wave lens-array antenna with 2-bit programmable antenna-filter-antenna (AFA) unit cells. The fabricated device is composed of 2420 switching elements scattered among 484 AFA elements (22×22 array). The fabrication is realized in quartz wafers utilizing adhesive bonding for packaging. Beam-steering is achieved by micro-positioning of each lens element towards specific locations, which in turn redirects the beam of the main feed (i.e. a horn antenna). The measured gain of this array is around 9.2 dB, however, a reported IL for the beam-steering lens array is noted as 8 dB. The group indicates that the high losses are mostly due to the low yield obtained during fabrication (~50%) and that by improving this metric, reduction of the IL up to 2 dB is possible.

In other work, Luo *et al.* propose an interesting approach for the use of MEMS cantilevers for phase modulation [60]. The idea is to design a tunable periodic structure which allows for phase control of the propagating wave inside the material. Tuning is achieved by actuation of a set of MEMS structures (referred to as J-units) that modify the impedance of each of unit cell, thus allowing for beam-steering capabilities since the antennas are integrated within the unit cells themselves. Beam-steering is demonstrated between ±15° as the J-units are sequentially actuated.

2.2. Microfluidically Reconfigurable Microwave Devices

As an alternative to both MEMS and MMICs, fluidic reconfiguration of microwave devices either through liquid or solid metals –or through dielectric materials contained inside a fluidic channel, has proved promising in applications where component flexibility or low-loss and high efficiency is required. While dielectric loading of RF components has been investigated, the preferred method for tunability is the use of liquid or solid metals due to its inherent advantage as

conductive material. Microfluidic loading of microwave devices has emerged as a low-cost, fully passive and versatile alternate technology [21] due to the limitations presented by SC/MMIC and MEMS technology, the increasing demand for additional system flexibility on wireless devices and the current need for wireless wearable gadgets. The concept of microfluidics applied on RF reconfiguration is simple: fluidic channels walls (at the mm and micron scale) that contain certain quantity of dielectric or conductive (in fluid or solid form) material loads or modifies the RF component geometry. In the same manner as MEMS, the field of microfluidics has flourished as an alternative to active reconfiguration with different groups investigating liquid metal loaded filters [61-63], antennas [15, 64-66], antenna arrays [67-69], reflectarrays [70, 71] and switches [17, 18, 72]. However, liquid metal has shown to have some major drawbacks such as being harmful for human health and the environment (i.e. in the case of mercury), and oxidization and low conductivity (with alloys such as Galinstan) [21, 73].

2.2.1. Liquid Metal Applications for Microfluidic Reconfiguration of Microwave Devices

Even though the use of liquid metals comes with certain drawbacks as discussed above, several designs have been fabricated, thus demonstrating promising applications of microfluidic technology. Nevertheless, further research is needed to address concerns regarding system integration, repeatability and packaging.

Among some of the relevant work in microfluidic applications, Chen *et al.* in [17], showed the wideband and low loss behavior of liquid metal switches. Different approaches were considered by using mercury, Galinstan and ultrapure ionic water. S-Parameter characterizations of the proposed switches placed within a 1500 μm CPW line was done from 2 to 100 GHz. For mercury and Galinstan, results showed that the IL was maintained below 1.3 dB for the whole range and 20 dB isolation. In the case of water, the switch transforms into an absorptive

component, showing 1.3 dB IL and above 10 dB RL in its off-state and 27.5 dB isolation when the channel is filled.

Similarly, Gough *et.al* demonstrate the viable application of continuous electro-wetting (CEW) for RF reconfiguration [74]. By introducing a liquid metal droplet inside a dielectric liquid, and then applying an external voltage, it is possible to produce a pressure imbalance that results in the motion of the liquid metal. A tunable antenna was designed and fabricated in order to demonstrate the applicability of this phenomenon in RF devices. It consisted of a slot antenna with center frequency at 2.65 GHz fed by a microstrip and liquid metal coupled to the feed via a microfluidic channel. Dynamic reconfiguration was achieved by extending the feed length as the microfluidic channel was filled with liquid metal. The antenna gain was approximated to 2 dB and tunable bandwidth was around 15.2 %.

Reconfiguration of an FSS was proposed by Lei *et al.* in [75] by using liquid metal inside periodically spaced PTFE tubes. The group used mercury to produce movable slugs inside an oil filled tube. It was shown that it is possible to model the liquid metal slugs as inductors, whereas the dielectric oil acts as capacitor. A parallel array of these tubes, along with the pressure control at the input of each channel, constitutes the FSS. Measurements showed the tunable capabilities of the design between 4 to 17 GHz.

2.2.2. Microfluidic Reconfigurable RF Devices Via the Metallized Plate Approach

Although liquid metal reconfiguration has shown some great progress in the recent years, there are still oxidization concerns when devices are fabricated using Galinstan. For these reasons, the use of metallized plates inside microfluidic channels has been proposed as an alternative to solve the problems encountered in liquid metal applications [24]. Different components such as reconfigurable filters [27, 76], antennas [77], and a 1D mm-wave microfluidic based focal plane

array [78] (MFPA) have been demonstrated using the plate metallization approach. Selective metallization of off-the-shelf RF substrates (e.g. Rogers RT/Duroid®, RO4000®) addresses the limitations of liquid-metals. By taking advantage of standard PCB photo-lithography it is also possible to design selective metallization patterns on these moving plates, thus providing extra degrees of freedom on component design [25, 65]. These devices have also shown great promise to handle high amount of power due to their materials and highly linear behavior [76, 77].

Dynamic bandpass filter reconfiguration is presented by Palomo *et al.* in [27]. The authors report low IL and wideband reconfiguration by using a selectively metallized plate approach. The filters were designed to operate between 0.8 to 1.5 GHz, achieving almost 2:1 tuning. Measured response shows 4.5 IL and constant fractional bandwidth within a margin of 5%.

A tunable monopole antenna from 1.7 to 3.5 GHz and over 2.4 realized gain was also demonstrated in [77]. Reconfiguration is accomplished by moving a metallized plate that acts as the main radiator. Power handling characterization were made, and the device proved to be able to handle at least 15 W at its highest operation frequency. One of the advantages of using the plate metallization approach is the highest thermal conductivity achieved by both substrate and insulator, as compared to using liquid metal for reconfiguration.

The microfluidic focal plane array (MFPA) proposed by Gheethan *et al.* in [78], was the first reported beam-steering application of microfluidics at mm-wave frequencies. The MFPA is composed of a metallized plate inside a microfluidic channel, which acts a patch antenna at 30 GHz. The antenna moves along the focal plane of an extended semi-hemispherical dielectric lens. The necessary considerations on feed network design for these MFPAs were thoroughly addressed in [78]. Measured gain was 23.5 dB, however, bandwidth limitations were clearly noted due to the resonant nature of the feed networks used and, when non-resonant networks are employed,

insertion losses are considerably high. All these advantages position microfluidic reconfiguration of microwave devices via the selectively metallized approach as a very attractive alternative to the use of liquid metals. The SMP approach allows for achieving successful design of microfluidically reconfigurable microwave with reliable and repeatable operation. Additionally, the use of SMPs allows for expanding microfluidic reconfiguration up to mm-wave frequencies thanks to the use of standard PCB techniques that avoid liquid metals with reduced conductivity and oxidization problems.

2.3. Chapter Summary

A general review about the field of RF device reconfiguration through MMIC, MEMS and microfluidic technology has been presented, and the advantages for each alternative have been noted. Current technology utilized for reconfiguration of microwave devices such as RFICs dominates most of today's applications thanks to their capabilities for high integration and extremely fast response times. However, RFICs still are limited by the elevated costs, limited performance in power handling, and considerably high losses. Whereas MEMS on the other hand, presents advantages of device integration, and low loss performance. Still, MEMS devices need to improve their reliability and simplify packaging challenges. As an attractive alternative to MEMS and RFICs, microfluidic technology promises low loss, highly linear, and high-power handling performances. In addition, it is inherently low cost due to is fabrication processes and it has been proven as a great approach for realizing flexible circuitry. Nevertheless, the field of microfluidics is still in its infancy although gaining momentum as new design approaches and solutions are proposed by different research groups.

Therefore, several concerns must be addressed if microfluidic technology aims to gain a solid foothold as a reliable application. Mainly: device packaging, repeatability and

reconfiguration speeds. The rest of this dissertation focuses on addressing these problems. Primarily, reconfiguration speeds are improved from the order of several seconds to millisecond ranges. Additionally, integrated actuation techniques are employed to demonstrate device operation in the order of millions of cycles. Furthermore, all the proposed solutions are offered at mm-wave bands, which represent the future of wireless communications technology. Proving that microfluidic reconfiguration can potentially be competitive when compared to current applications of MEMS or RFICs.

Chapter 3: Microfluidically Switched Microstrip Lines Using Selectively Metallized Plates[2]

Microfluidic technology has been demonstrated in the past as switching mechanism for microstrip lines [81], waveguides [82], and coplanar waveguides [18]. However, these applications use liquid-metal inside the microfluidic channels. When there is no need for substrate elasticity, introducing a Selectively Metallized Plate (SMP) inside the channel helps to circumvent the limitations of liquid-metals [14]. Additionally, the SMP approach avoids oxidization and channel contamination problems that have been noted to be present when liquid metal is used. Moreover, the use of readily available PCB technology for manufacturing the SMPs provides design flexibility and simplicity. All of this while maintaining the advantage of high conductivity of copper traces of the PCB. Therefore, realizing a microfluidically controlled switch via the SMP approach, increases the flexibility in application areas of this technology. The fundamental switching approach exploited for this purpose is the one of strong capacitive coupling between the metal traces of the SMP and the PCB metals. This allows for control of loss and isolation of the RF switch by properly designing the switch geometry and substrate stack-up. This chapter presents such approach and demonstrates the low loss and wide band capabilities of these types of switches.

3.1. Microfluidically Switched Microstrip Line Design and Equivalent Circuit Model

A microstrip line that is microfluidically switched by an SMP can be designed by considering a structure shown in in Figure 3.1(a). Moving the SMP along the channel makes it

[2] Portions of this chapter have been published in [79, 80]. Copyright permissions can be found in Appendix B.

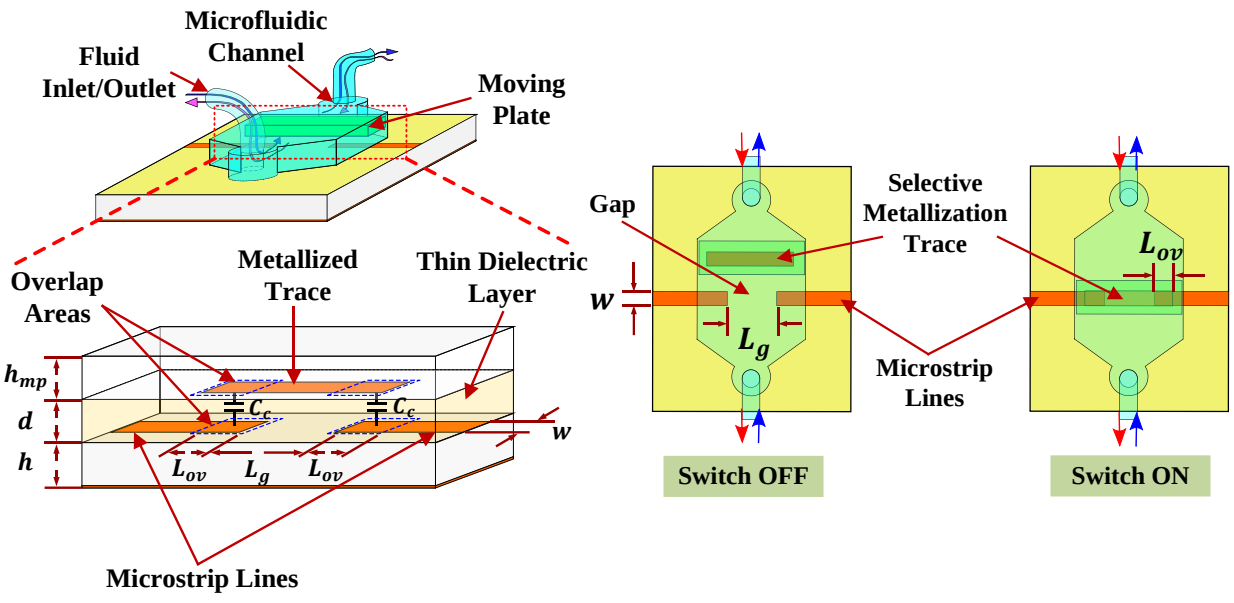

Figure 3.1. Microfluidically switched microstrip line design layout. (a) Isometric view of the microfluidically switched microstrip line stack-up, the materials used are PDMS for the fluidic channel, BCB for the thin dielectric layer, Rogers RO4003C™ for the microstrips and RT/Duroid® 5880 (εr = 2.2, tanδ = 0.0004) for the SMP with $h_{mp} = 0.254$ mm, $h = 0.203$ mm and $d = 6$ μm. Top views of the ON (b) and OFF (c) states of the switch.

possible to enable or interrupt the energy flow along the microstrip. The OFF and ON states of the switch are depicted in Figures 3.1(b) and 3.1(c), respectively. The gap does not only interrupt the energy flow but also provides control over the isolation. Microstrip gap discontinuities have been widely studied in the past, and there are closed-form expressions already available in [83] that model their behavior as capacitive π-network under certain circumstances (i.e. specific microstrip width, gap spacing, substrate height and permittivity). When the dimensions of the microstrip gap or substrate properties fall outside of the readily available formulae in [83], EM modeling can be utilized to extract the equivalent Y-Parameters and calculate the corresponding capacitance values as in [84]. In either case, the circuit model for the gap discontinuity consists of coupling capacitor (C_g) between the open ended microstrip lines and the two capacitors (C_d) to ground from each open end. Similarly, the coupling between the SMP and the microstrip lines can be modeled by

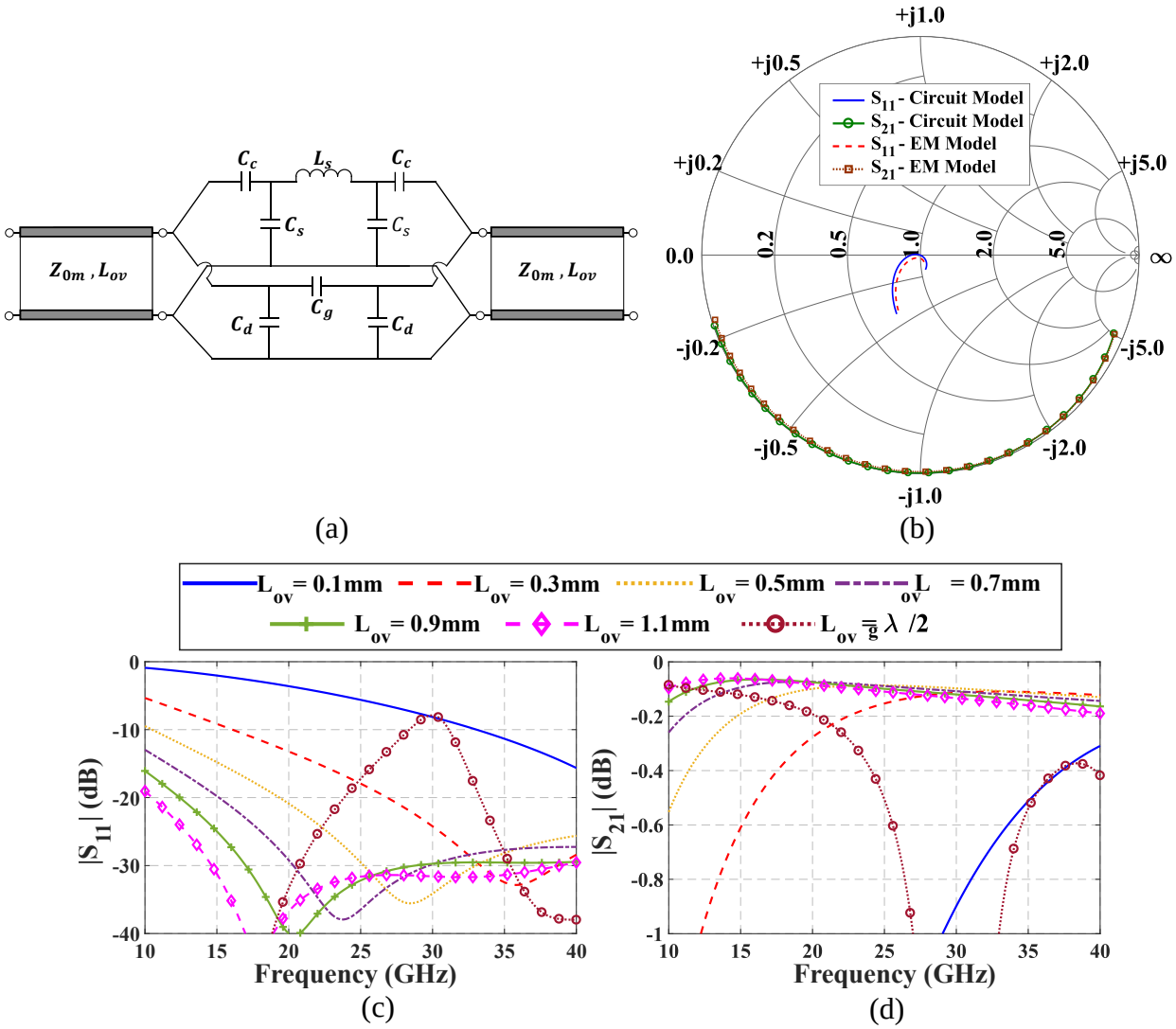

Figure 3.2. Equivalent circuit model and performance of the switch. (a) Circuit model; (b) scattering parameters obtained from EM and schematic simulations for L_{ov} = 0.5 mm (Circuit Model: $Z_{0m} = 50\ \Omega$, $L_{ov} = 0.736$ mm, $C_s = 12.53$ fF, $L_s = 128.26$ pH, $C_g = 0.398$ fF, $C_d = 11.734$ fF and $C_c = 0.856$ pF); (c) S_{11} and (d) S_{21} performances within 10 – 40 GHz band for varying L_{ov} values.

two capacitors (C_c) in the overlap areas. The SMP area over the gap can be represented by a low pass π- network consisting of series inductor L_s and shunt capacitors C_s. Consequently, the equivalent circuit model for the switch becomes as shown in Figure 3.2(a). It is important to note that this model exhibits slight difference with respect to the ones presented in [66, 85] for liquid metal loaded structures. Reference [85] models a microfluidically switched slot antenna with

transmission lines, while the liquid-metal loading the slot is modeled by a shunt capacitance. Reference [66] represents the coupling effect of the liquid-metal-filled microfluidic channel with equivalent shunt open-circuited stubs. The model utilized here retains the microstrip lines under the overlap areas as transmission lines with characteristic impedance Z_{0m}. These lines are modeled as microstrips placed in the multi-layer substrate stack-up (ADS TLines-LineType library). The coupling at the overlap areas is represented by the series capacitors C_c in contrast to the circuits in [66, 85] that utilize transmission lines. This circuit model is expected to have accuracy for electrically short overlap lengths ($L_{ov} \leq \lambda_g/4 = 1.31$ mm) due to this series capacitance approximation.

The validity of this circuit model is verified in Figure 3.2(b) by comparing the scattering (S) parameters obtained from the EM model (Keysight Advanced Design System [ADS] Momentum) for L_{ov}= 0.5 mm and circuit schematic simulations. The initial value of C_c is extracted from the well-known parallel plate capacitor equation, L_s and C_s are calculated from equation (1) of [86], C_g and C_d are evaluated from equation (5.20) in [84]. The gap length L_g is selected as 0.8 mm to achieve > 28 dB isolation at 30 GHz with a compact size. The final component values of the circuit model are obtained by matching the S-Parameter response of the circuit to the one from the EM simulation through optimization. The variables that are optimized in the circuit model are the coupling capacitance (C_c), the equivalent inductance (L_s) and capacitance (C_s), and (L_{ov}). The optimization compensates for the fringing fields and multilayered substrate that are not considered in the calculation of the initial component values. Appendix A demonstrates the optimization process chosen to validate the assumptions made within this circuit model. Figure 3.2(c) and 3.2(d) depict the S_{11} and S_{21} performances of the switch for different L_{ov} values. As expected, large L_{ov} values correspond to larger coupling capacitances, lower insertion losses, and wider bandwidth

performances. It is observed that insertion loss (IL) at 30 GHz remains < 0.2 dB for L_{ov} > 0.3 mm. For the switch implementation, an L_{ov} value of 0.5 mm is selected to achieve a wide bandwidth performance ($|S_{11}|$ < -10 dB above 10 GHz) and accommodate fabrication/positioning uncertainties. Figure 3.2(c) and 3.2(d) also demonstrate the S_{11} and S_{21} performances of the switch obtained from EM simulation for half guided wavelength overlap length ($L_{ov} = \lambda_g/2$). It is clearly seen that the performance is significantly deteriorated due to the realization of a broadside resonant coupled line structure.

3.2. Fabrication and Experimental Verification

To experimentally verify the simulated switch performance, a device prototype is fabricated by utilizing the micro-molding techniques. For the microfluidic channel, a photoresist (SU8-2075) mold is fabricated by standard photolithography on a dummy silicon wafer. Then, a 10:1 mixture of PDMS is poured on top in order to produce a 2 mm thick microfluidic chip housing a 2 mm wide by 0.3 mm high microfluidic channel. The microstrip and metallized trace of the moving plate is $w = 0.42$ mm wide to realize 50 Ω lines. After patterning the microstrip via standard photolithography, the substrate is spin-coated with a 6 μm thick insulating layer of BCB and cured in a programmable convection oven attending to the manufacturer guidelines. Following the curing process, the substrate is exposed to oxygen plasma activation (50 W for 30 s at < 0.7 Torr), submerged in a 5% (3-Aminopropyl)triethoxysilane (APTES) solution kept at 70 °C for 20 minutes, and dried with a nitrogen gun. Subsequently, the SMP is positioned on top of the substrate, which is then brought in contact with the PDMS chip that has been exposed to plasma activation. To ensure a strong bond between the substrate and the PDMS chip, the device is placed in a convection oven at 110 °C for 30 min. In addition to the microfluidically switched microstrip line, a continuous reference microstrip line is also fabricated under the identical substrate stack-up

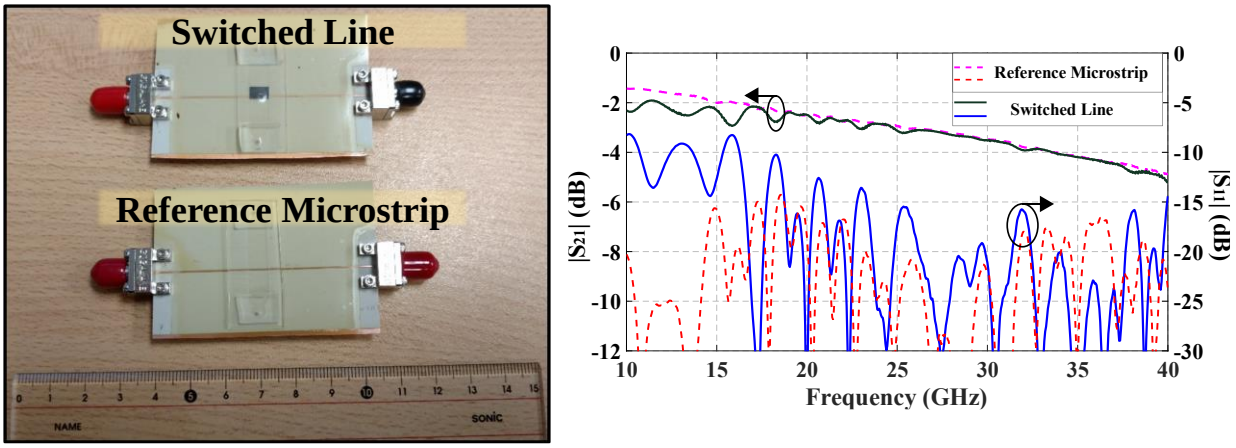

(a) (b)

Figure 3.3. Microfluidically switcher microstrip prototype and its measured performance. Microfluidically switched and reference microstrip line prototypes (a) with measured S_{11} and S_{21} performances (b).

for performance comparison. Figure 3.3 shows the fabricated lines and their measured performances. Specifically, the microfluidically switched line performs almost identical with the continuous line above 16 GHz exhibiting an $|S_{11}|$ < -10 dB. The IL difference is less than 0.2 dB over a wide frequency range (> 20 GHz) as predicted by the circuit model.

3.3. Chapter Summary

Microfluidically switched microstrip lines utilizing the selectively metallized plate approach are introduced to demonstrate low loss and wideband performance of microfluidic reconfiguration of microwave devices at mm-wave frequencies. The microfluidic switch performs with less than 0.2 dB IL over 20 GHz bandwidth and an equivalent circuit model is developed to aid in the design of such switches. Specifically, the equivalent circuit model can be employed to develop complex networks with several switches as it will be demonstrated in the next chapter. By utilizing this type of switching mechanism with microfluidic technology, it will be possible to reduce device reconfiguration time from the order of seconds to a few hundreds of milliseconds.

Chapter 4: Millimeter-Wave Beam-Steering Focal Plane Arrays[3]

Microfluidic beam-steering focal plane arrays (MFPAs) offer beam-steering capabilities without the need of active RF devices, potentially reducing costs and providing higher efficiency performance. The concept of MFPAs was demonstrated by microfluidically positioning a patch antenna (in the form of liquid metal [16] or metallized plate [78]) at the focal plane of an extended hemispherical dielectric lens. However, the feed networks of [78] needed to accommodate the position variation of the antenna element by making use of multiple resonance mechanisms. Consequently, this made the bandwidth of the arrays dependent on array size. To solve this limitation, a Selectively Metallized Plate (SMP) was introduced within a microfluidic channel to implement a microfluidically switched feed network. This feed network utilizes the microfluidic switching concept presented in Chapter 3. With this approach, same beam-steering range and antenna gain as in [78] is achieved while providing reduced reconfiguration times. This was possible by decreasing the motion range by a factor of about 10 times with a compact switching mechanism. In addition, because the feed network does not rely on multiple resonant elements, a better bandwidth performance is possible. Specifically, the need for resonant feed networks is alleviated by resorting to a microstrip line feed network exhibiting gap discontinuities that can be switched on/off by microfluidically repositioning an SMP. To be able to utilize a single bi-directional micropump unit, the gap discontinuities and SMP metallizations are arranged strategically to sequentially direct the RF power to the antenna elements of the focal plane array.

[3] Portions of this chapter have been published in [79, 80, 87]. Copyright permissions can be found in Appendix B.

Furthermore, a position sensing approach integrated with the microfluidically repositionable SMP is introduced for the first time to enable closed-loop precise positioning control.

It was experimentally verified that the MFPA exhibits 22.6 dBi peak gain corresponding to < 3 dB feed network loss. The measured data agrees quite well with the expected device performance extracted from a mixture of full-wave electromagnetics (EM) and circuit simulations. These studies demonstrate that the microfluidically switched feed network performs with wide bandwidth (~38%) and low insertion loss (IL). Hence, the feed antenna of the MFPA becomes the major limiter of the bandwidth (as compared to the bandwidth limitation associated with the feed network resonances presented in [78]). An integrated sensing approach for detecting the SMP position is also demonstrated for the first time to facilitate the use of presented MFPAs with closed-loop position controllers. The significantly reduced microfluidically actuated motion range (4.2 mm vs. 40 mm of [78]) is also experimentally shown to result in a much faster beam-scanning performance (270 ms vs. 5.25 s of [78]).

4.1. Operation Principle of the Microfluidically Switched MFPA

The substrate stack-up of the MFPA is presented in Figure 4.1(a) along with the external piezoelectric micropump actuation mechanism. Rogers RO4003C™ (ε_r = 3.38, tanδ = 0.0022) laminates with 0.203 mm thickness and 17.5 µm of copper cladding are used as the substrates for the patch antenna elements, microstrip line feed network, and the SMP located inside the microfluidic channel. The patch antennas are excited with aperture coupling and designed to operate at a center frequency of 30 GHz with an 8% fractional bandwidth (FBW). The antennas are located at the back surface (i.e. focal plane) of an extended semi-hemispherical dielectric lens. The lens is 8 cm in diameter with 4.32 cm extension length and made from Rexolite® (ε_r = 2.55, tanδ = 0.00085). Based on ray-tracing [78] and Tai & Pereira's approximation [88], it provides

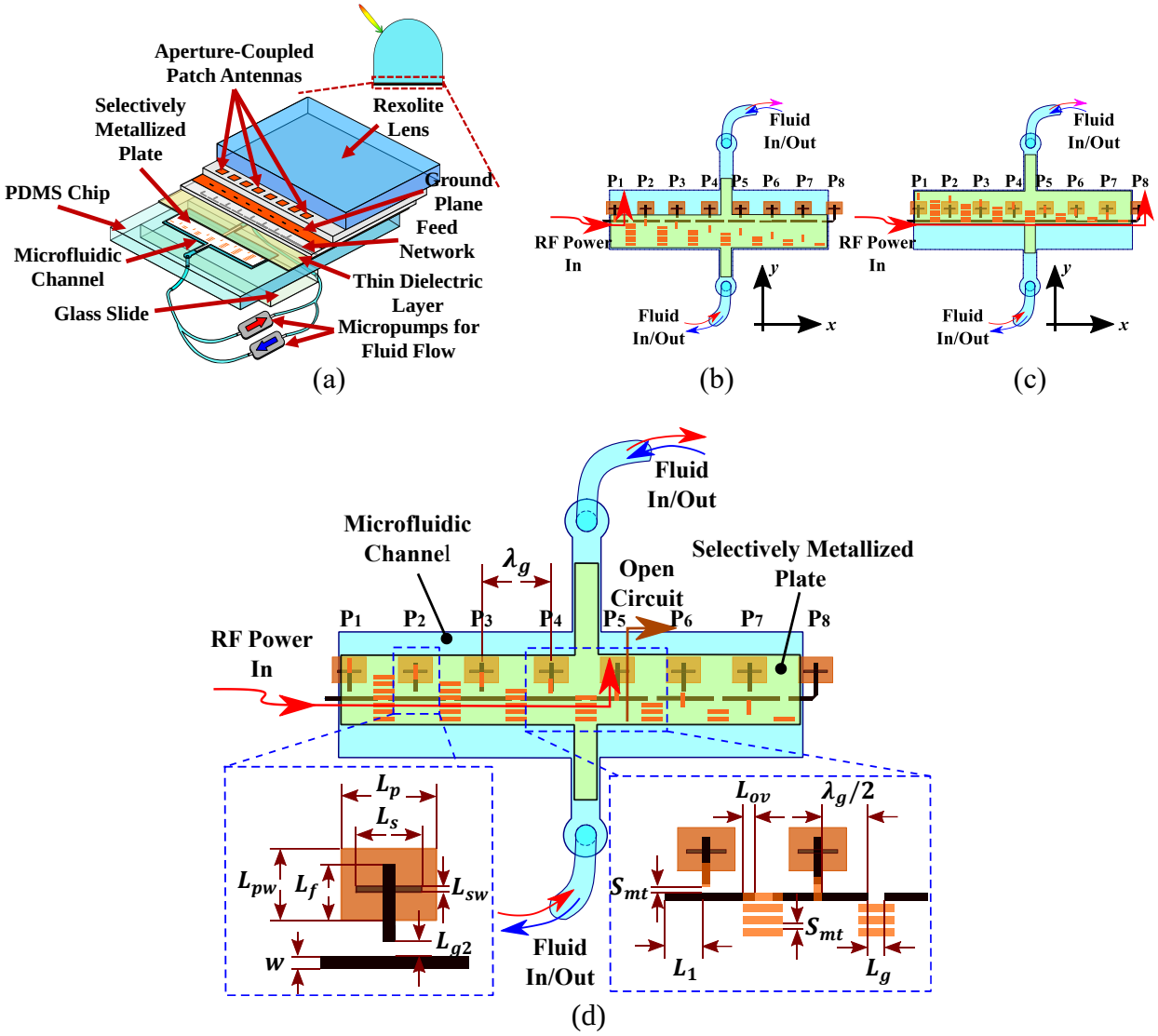

Figure 4.1. Operational principle and design layout of the 8-element MFPA. (a) Substrate stack-up; (b) selectively metallized plate (SMP) positioned to excite first antenna element; (c) SMP positioned to excite last antenna element; (d) detailed layout with dimensions w = 0.39, L_1= 2.25, L_{ov}= 0.5, L_g= 0.8, L_{g2}= 0.3, L_p= 2.86, L_{pw}= 2.16, L_s= 1.97, L_{sw}= 0.18, L_f= 1.7, S_{mt}= 0.3, and λ_g = 5.23 (all units are in mm).

28.4 dBi directivity and ±30° beam-scanning capability. The microstrip line feed network is designed with a specific set of gap discontinuities. The microfluidic channel that carries the SMP is bonded to the surface of the feed network by utilizing a low loss thin benzocyclobutene (BCB, ε_r = 2.65, tanδ = 0.00088 [89]) insulator layer. Consequently, the metallizations of the SMP are brought near the feed network. To generate strong capacitive coupling (and a potential RF short-

based switch) between the two, the BCB thickness is selected as small as possible (6 μm for the Cyclotene™ 3022-57 BCB resin available in our laboratory). The 270 μm microfluidic channel is prepared from a 2 mm thick Polydimethylsiloxane (PDMS, ε_r = 2.7, tanδ = 0.045 [90]). Motion of the SMP is possible by filling the microfluidic channel with a low-loss dielectric liquid (Sigma-Aldrich FC-40, ε_r = 1.9, tanδ = 0.0003) and using a pair of parallel-connected piezoelectric micropumps (Bartel mp6 30×15×3.8 mm^3, ~200mW). A 1 mm thick soda-lime glass, ($\varepsilon_r = 6.2$, $\tan\delta = 0.023$) is bonded to the top of the microfluidic channel in order to prevent bulging of PDMS due to the fluid pressure and its elastic nature.

The SMP carries sets of horizontal (*x*-directed) and vertical (*y*-directed) metallization strips as shown in Figures 4.1 (b)-(d). The positions of horizontal and vertical strips are adjusted to overlap with the microstrip feed line discontinuities at specific SMP positions. The horizontal strips are placed in sets with changing element numbers. This is to ensure a sequential switching functionality among the antenna elements. As an example, Figure 4.1(b) depicts the initial position of the SMP that activates the antenna element in position #1 (P_1). Moving the SMP in a certain increment along the *y*-axis [i.e. $S_{mt} + w$ based on the layout shown in Figure 4.1(d)] directs the RF power from antenna element at P_1 to P_2. Multiple increments or decrements in SMP position can be used to activate any antenna element within the array. As an example of another state, Figure 4.1(c) depicts the position of the SMP that directs the RF power towards the antenna element at P_8. Layout details of the microstrip line feed network, SMP, and aperture coupled patch antennas are presented in Figure 4.1(d).

4.2. Microfluidically Switched Feed Network Design

The main concept of this design utilizes the microfluidically switched microstrip lines that were introduced in Chapter 3. Several switched line elements are strategically cascaded to form a

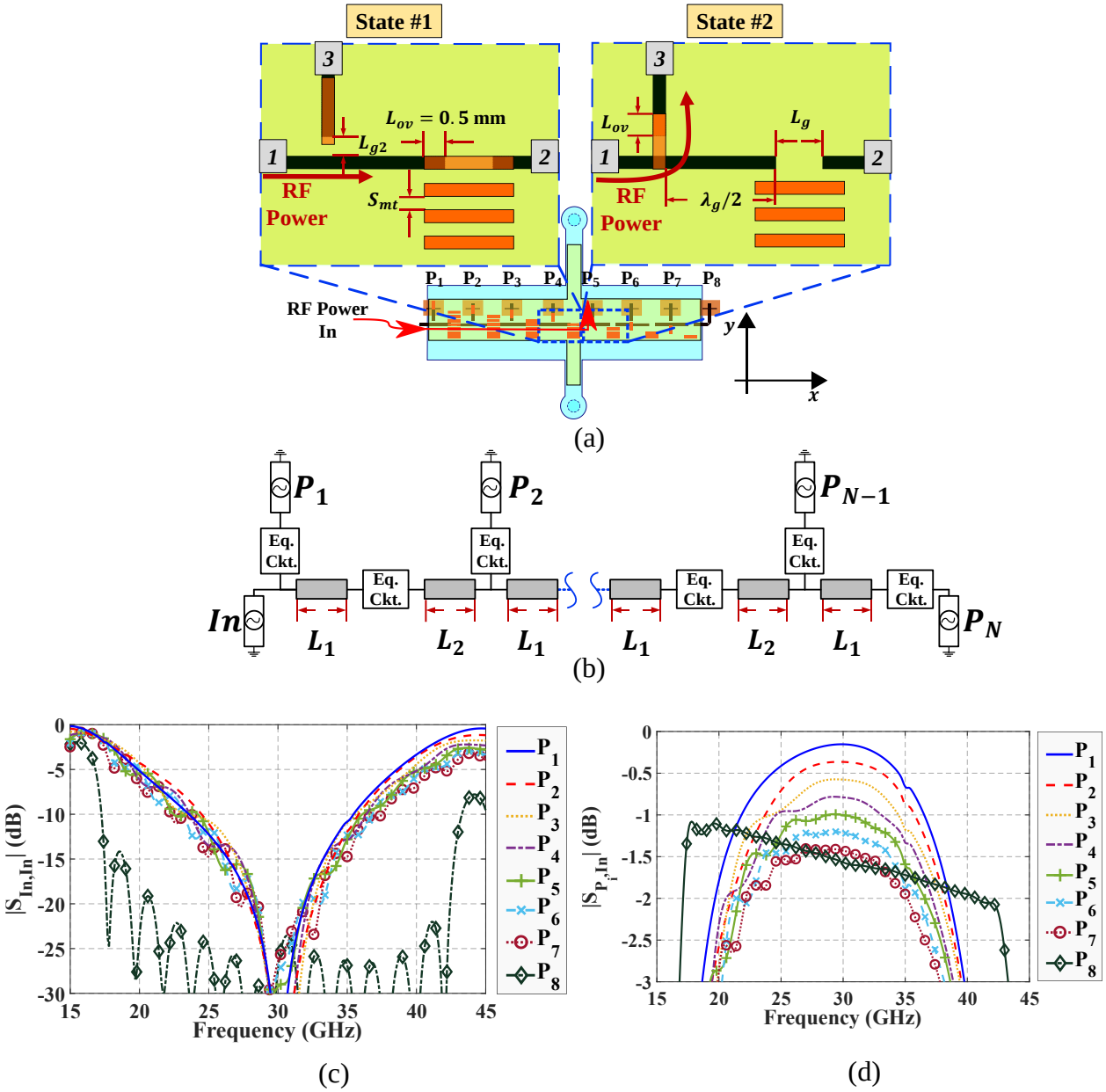

Figure 4.2. Figure 4.2.MFPA feed network layout and simulated performance for increasing number of elements. (a) Subnetworks from the feed network of 8-element MFPA when the SMP is positioned to direct RF power towards the antenna at position P_5; (b) transmission line model of the feed network with equivalent circuits in Figure 4 representing the switch behaviors (C_s = 13.13 fF, L_s = 119.58 pH, C_g = 2.11 fF, C_d = 13.83 fF, C_c = 0.863 pF, L_{ov} = 0.764 mm, $L_{1OFF} = \lambda_g/2$ = 2.65 mm, L_{1OFF} = 2.15 mm, L_2 = 1.82 mm); (c) $|S_{In,In}|$ performance and (d) $|S_{P_i,In}|$ for an 8-element array when SMP is positioned to excite each port P_i.

feed network for beam-steering MFPAs. Figure 4.1 has already presented the detailed layout for an 8 element MFPA. The performance of this feed network (or similar networks designed for larger

1D arrays) can be investigated by considering the subnetworks shown in Figure 4.2(a). Specifically, these subnetworks correspond to the regions of the feed network between antenna positions P_4-P_5 (state #1) and P_5-P_6 (state #2) when the SMP is positioned to direct RF power towards the antenna at position P_5. These states provide a Single-Pole-Double-Throw (SPDT) switching functionality by directing RF power to flow towards *x*-axis from Port 1 to Port 2 (state #1) or towards *y*-axis from Port 1 to Port 3 (state #2). From Figure 4.2(a) it can be noted that the overlap length (L_{ov}) at the vertical switching position is equal to the width of the 50 Ω microstrip line. This is done to provide design simplicity and to avoid extra coupling/mismatch effects at the T-junction. Moreover, it is important to note that a half-wavelength $\lambda_g/2$ open circuited stub is utilized to generate an open-circuit condition at the vertical switch junction to maximize the RF power flow through the 90° bend. This $\lambda_g/2$ stub is therefore the main limiting factor for the bandwidth of the feed network. Nevertheless, since any excited antenna within the array only utilizes one of these stubs (except the last element that does not need the stub), the bandwidth of the feed network is extremely wide as compared to the resonant feed networks of prior work that require multiple wavelength long stubs [78].

The IL and bandwidth performance of the feed network can be conveniently analyzed for varying array sizes by making use of transmission line theory and the equivalent circuit model of the switch that was developed in Chapter 3 [as seen in Figure 4.2(b)]. The component values of the equivalent circuit model are updated and optimized to match the switch placed in the substrate stack-up of the MFPA. The antennas are replaced with ideal 50 Ω terminations to investigate the antenna-independent performance of the feed network. The length of the transmission line that corresponds to the half-wavelength stub (L_1) is modified from L_{1OFF} to L_{1ON} depending on each state of the switch. Figure 4.2(c) presents the $|S_{In,In}|$ performance of the 8-element array ($N = 8$)

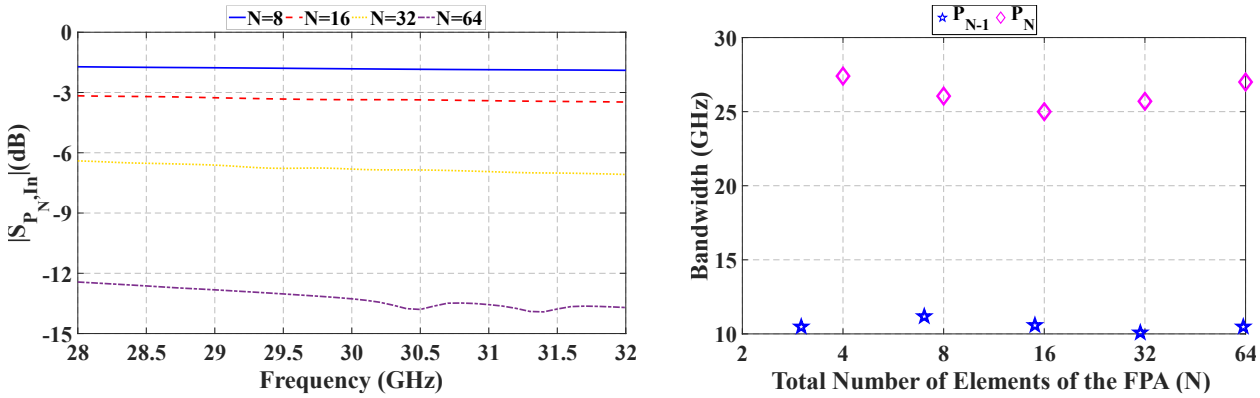

(a) (b)

Figure 4.3. Insertion loss and bandwidth performance of the MFPA for different array sizes (i.e. N=4, 8, 16, 32 and 64). (a) S_{21} performance of the feed network for different array sizes; (b) Bandwidth performance as a function of array size.

as SMP is positioned to excite ports P_1 to P_8 It is seen that the bandwidths of the ports $P_1 - P_7$ are almost identical. The bandwidths of these ports are limited by the $\lambda_g/2$ stub. Since any excited port only utilizes one stub (except the last element that does not need the stub), the bandwidth of the feed network is still extremely wide (38%) as compared to the resonant feed networks that require multiple wavelength long stubs [78]. The bandwidth of the last element is determined by the switch performances. Figure 4.2(d) depicts the $|S_{Pi,In}|$ performance of the 8-element array ($N = 8$) as SMP is positioned to excite ports P_1 to P_8. At the center frequency of 30 GHz, it is clearly observed that the IL increases from P_1 to P_8 and therefore IL can be attributed to the microstrip line losses. The worst-case IL (1.58 dB) is observed for the last port (i.e. $P_N = P_8$) since the last port is excited by the longest microstrip line.

Since P_N exhibits the largest IL, Figure 4.3(a) presents the $|S_{P_N,In}|$ performance for varying array sizes to investigate the worst-case feed network loss. Clearly a low loss performance is achieved as compared to conventional SP2T switch loaded feed network implementations. For example, a 16-element conventional beam-scanning FPA can be implemented with 15 SP2T switches. Each excited element within this array would require RF power to pass through 4 SP2T

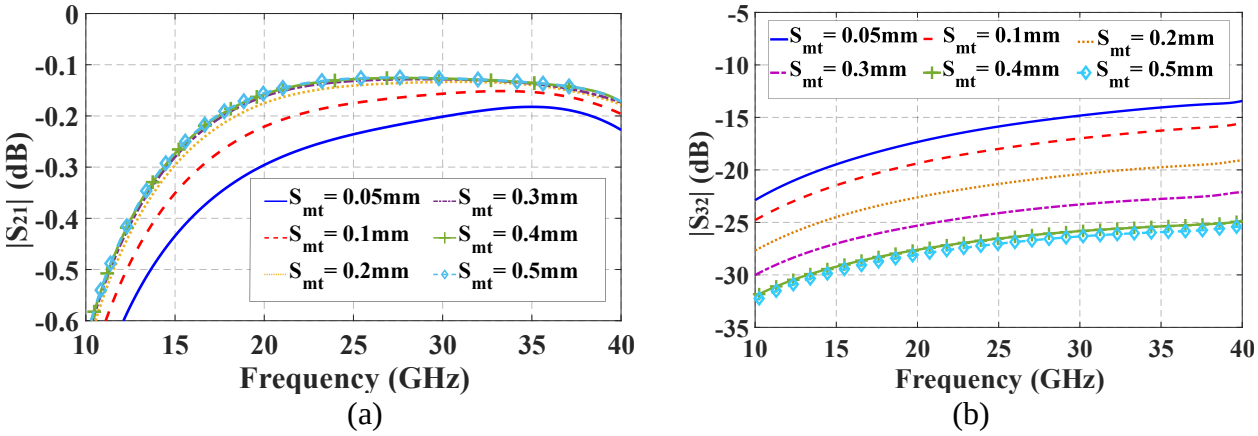

Figure 4.4. Effect of metallized trace position and overlap length on insertion loss and isolation of the feed network of the MFPA. S_{21} (a) and S_{32} (b) performances as a function of S_{mt} in State #1 and State #2 subnetworks shown in Figure 4.2(a), respectively.

switches. The IL is expected to be well above 4 dB (assuming 0.9 dB loss per switch [91]) due to the interconnect and transmission line losses. In addition, the DC bias and switch state control lines are expected to result in complex high-cost feed network assemblies. On the other hand, the N = 16 MFPA feed network exhibits a simplified design and about 4 dB loss based on the transmission line study discussed above. Figure 4.3(b) presents the $|S_{11}|$ < -10 dB bandwidth performance of the feed network for varying array sizes. The $(N-1)^{th}$ element of the array and all the preceding elements utilize a single $\lambda_g/2$ open circuited stub when the SMP is positioned to excite them. While for the last element (N^{th}) of the array, the bandwidth is limited by the switches connected in series, since there are no resonant lines. This results in a worst case ~38% bandwidth (~12 GHz at 30 GHz) performance independent of the array size.

It is important to mention that the spacing between the metallized traces (S_{mt}) of the SMP also plays a role in the feed network performance. S_{mt} design is carried out by considering reconfiguration speed and RF performance (i.e. isolation and IL). Larger S_{mt} values increase the reconfiguration time needed when switching the excited antenna element, whereas smaller S_{mt} values negatively affect the RF performance due to coupling between adjacent metallized traces.

The coupling effect is investigated by carrying out EM simulations of the state #1 subnetwork shown in Figure 4.2(a) by assuming horizontal metallized traces exist on both sides of the microstrip line. Figure 4.4(a) shows that the impact on S_{21} becomes negligible for S_{mt} > 0.2 mm. For state #2, S_{32} (i.e. isolation) gets worse by smaller values of S_{mt} as shown in Figure 4.4(b). In the presented 8-element MFPA layout, S_{mt} was selected to be 0.2 mm to ensure > 20dB isolation.

4.3. Experimental Verification of MFPA Performance

Two MFPA prototypes were characterized, one corresponding to the design layout described in Section 4.2 [see Figure 4.1(d)], and another one including additional features for position sensing and control that will be described in Section 4.4. Both prototypes exhibit similar performances. The MFPAs were fabricated by utilizing micro-molding, photolithography and multilayered printed circuit board assembly techniques. The feed network is first fabricated by standard photolithography and then the antenna coupling apertures are patterned onto the ground plane by employing an optical mask aligner (EVG 620) for back-side alignment. This feed network substrate is then bonded to the antenna substrate (with one side of its copper cladding removed) by using a 100 μm thick Rogers RO4450F™ prepreg layer. The bonding is performed with a press that keeps the substrates under the pressure and temperature rise guidelines recommended by Rogers Corp. Following the bonding process, the patch antennas are patterned by standard photolithography and feature alignment. The SMP shape is realized with a milling machine (LPKF S63) and metallized traces are patterned via standard photolithography. The BCB deposition, preparation of the microfluidic PDMS chip, and bonding the PDMS chip with the feed network substrate is identical with the procedures discussed previously for the microfluidic switch. The glass and the PDMS are bonded together through plasma activation with similar parameters used in PDMS to BCB bonding.

The fabricated prototype is presented in Figure 4.5(a) and the measured S_{11} and 30 GHz x-z plane normalized gain patterns of the array are shown in Figures 4.5(b) and 4.5(c), respectively, for SMP positions corresponding to different antenna excitations. The measured S_{11} performances demonstrate that the MFPA bandwidth (i.e. 8% $|S_{11}|$ < -10 dB) is established solely by the antenna element in contrast to prior work that was limited by the resonant feed network itself (i.e. 3%). EM simulations carried out by Keysight ADS Momentum predict similar S_{11} performances when all substrate discontinuities exhibited in the prototype are accounted for (i.e. the extension line needed to accommodate the edge connector for experimental purposes does not completely lie under the PDMS chip and crosses over different substrate stack-up regions). The measured gain values are observed to remain almost constant across the bandwidth. The beam-steering capability is

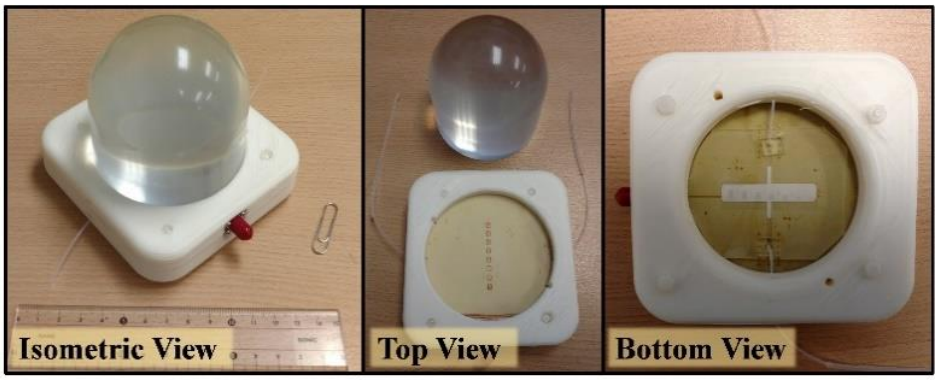

(a)

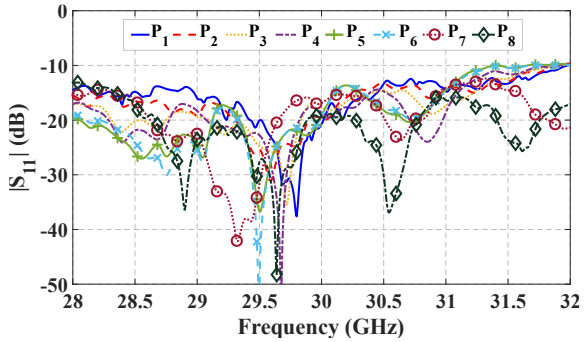

(b)

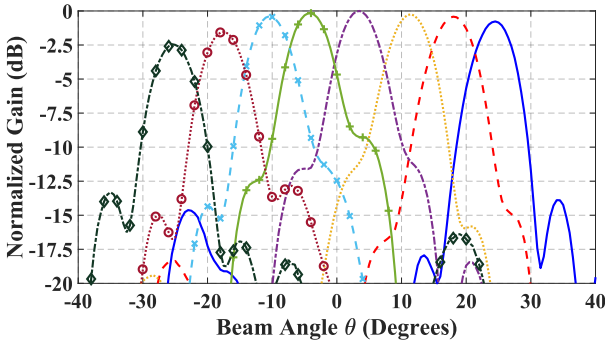

(c)

Figure 4.5. Fabricated MFPA and its measured performance. Isometric, top and bottom views of the prototype (a). Measured S_{11} performance as the SMP is positioned to excite the antennas at locations P_1 to P_8 (b) and x-z plane normalized gain at 30 GHz (c).

demonstrated in Figure 4.5(c). The patterns exhibit 7° half-power beamwidth with > 20 dB realized gain at 30 GHz. The simulated and measured gain values agree within 1dB. These differences may be due to the minor misalignments in microfluidic channel bonding, FC-40 presence below the SMP, and minor uncertainties/errors in anechoic chamber measurements. Nevertheless, even when the losses introduced by the edge connector, lens, extension line, antenna efficiency are considered, and the 1 dB gain disagreement is assigned to feed network loss (i.e. the worst-case scenario), the measured feed network loss remains equal or less than 3 dB. A summary of the measured data compared to the expected theoretical results is presented in Table 4.1.

4.4. Closed-Loop-Control Considerations for SMP Positioning

The small motion range (4.2 mm total) and positioning accuracy needed for the RF switching functionality (0.6 mm increments) is expected to necessitate a reliable technique for sensing/controlling the SMP position. The SMP technique provides a convenient way to implement non-destructive sensing schemes since the plate size/shape can be adjusted to include metallization traces for sensing purposes. To demonstrate this possibility, the SMP shape was modified to include a trapezoidal metallization area as shown in Figure 4.6(a). This metallization area interacts with an inductive spiral coil (13.9 mm diameter, double layer, 19 turns/layer, 0.15 mm trace width and spacing) that is interfaced with the Texas Instruments (TI) LDC1614 inductance to digital converter chip (LDC) as shown in Figure 4.6(b) [92]. The inductance of the coil is modified as the position of the trapezoidal metallization within the microfluidic channel is varied. The trapezoidal shape of the metallized pattern allows for a smooth change in the inductance as the SMP is repositioned. The LDC1614 features 28 bits of resolution and potentially provides sub-micron position sensing accuracy [92]. The sensing coil and inductance-to-digital converter used in Figure 4.6 are from the TI evaluation module (TI-EVM) which provides the

Table 4.1. Measured gain performance of the MFPA.

Excited Antenna #	**1**	**2**	**3**	**4**	**5**	**6**	**7**	**8**
Steering Angle (Measured / Calculated)	24.5º / 25º	18° / 18°	11.5º / 11º	3.5º / 4º	-4º / -4º	-10.5º / -11º	-17.5º / -18º	-25.5º / -25º
Theoretical Gain (dB)	28.4	28.4	28.4	28.4	28.4	28.4	28.4	28.4
Connector Loss (dB)	0.5	0.5	0.5	0.5	0.5	0.5	0.5	0.5
Ext. Line Loss (dB)	2.05	2.05	2.05	2.05	2.05	2.05	2.05	2.05
Lens Loss (dB)	2.2	1	0.4	0.7	0.7	0.4	1	2.2
Feed Network Loss (dB)	0.16	0.37	0.58	0.8	1.05	1.23	1.45	1.58
Antenna Efficiency (dB)	1.02	1.02	1.02	1.02	1.02	1.02	1.02	1.02
Expected Gain (dB)	22.47	23.46	23.85	23.33	23.08	23.20	22.38	21.05
Measured Gain (dB)	**21.9**	**22.2**	**22.4**	**22.6**	**22.5**	**22.2**	**21.0**	**20.2**

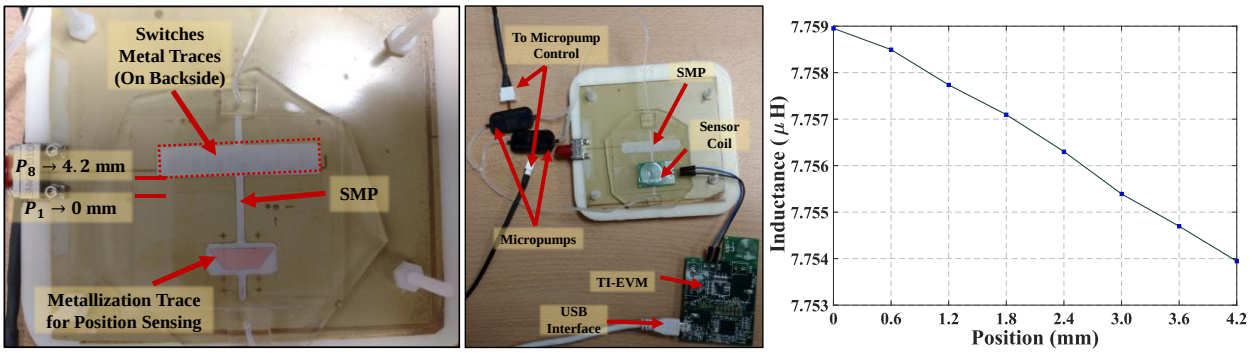

(a) (b) (c)

Figure 4.6. Position sensing implementation within the SMP of the MFPA. (a) Modified SMP and microfluidic channel shape to achieve position sensing by using TI inductor to digital converter chip; (b) Experimental setup for position sensing; (c) Detected inductance values as the SMP is re-positioned from P_1 to P_8.

LDC1614 along with a micro processing unit. In addition, the measured inductance values can be easily accessed via the vendor-provided software through USB interface.

Figure 4.6(c) presents the measured inductance by the TI-EVM as the SMP is moved across all switching positions (i.e. from P_1 to P_8). Specifically, the coil inductance varies by ~0.6 nH as the switching position is changed. The position-based variation observed in inductance values clearly demonstrates that the SMP position can be accurately controlled in a closed-loop control system. Further improvements in inductance variation range and shape could be potentially achieved by redesigning the metallized trace, sensor coil and substrate thicknesses. With the shown SMP configuration and micropumps, the reconfiguration time between two switched beams is tested to be about ~39 ms. The travel time from the first position (P_1) to the last (P_8) is measured to be ~270 ms. This speed is significantly improved as compared to prior work that needed a large motion range (270 ms vs. 5.25 s [78]). This application demonstrates the flexibility of the SMP approach to integrate sensing schemes that can provide closed-loop control of the SMP position. Additionally, with the achievements on improved bandwidth and much shorter reconfiguration

speed performances, it is now possible to expand the MFPA concept into high-gain two-dimensional beam-steering arrays at mm-wave frequencies.

4.5. Millimeter-Wave 2D Beam-Steering Focal Plane Array with Microfluidically Switched Feed Networks

The need for high-gain beam-steering arrays at mm-wave frequencies, makes it necessary to integrate a high number of antenna elements which can be reconfigured on-demand to provide control over the antenna beam direction. Having demonstrated a compact application for 1D beam-steering MFPAs in the previous section, it is now possible to extend the microfluidically switched feed network concept to 2D beam-steering. This application will be discussed through an 8×8 array design.

4.5.1. 2D Beam-Steering MFPA Design

The 1D beam-steering MFPA concept presented in the previous section can be extended into 2D beam-steering by employing an array of the feed network of Figure 4.2(a). As seen in Figure 4.7(a), independent beam-steering in two orthogonal planes can also be achieved by utilizing two distinct microfluidic channels each connected to their own bi-directional micropump unit. In the layout shown in Figure 4.7(a), the micropumps of the microfluidic channel on the left allows for row selection. On the other hand, the micropumps of the microfluidic channel on the right is utilized to excite antenna elements within a desired column. The larger size of the selectively metallized plate within this microfluidic channel allows such operation. The total movement needed by the plates is equal to 4.2 mm. Based on the capabilities of the piezoelectric micropumps utilized in our experiments, it is expected that the worst-case beam-steering scenario (i.e. sequential excitation of elements in ends of a diagonal) will be completed in ~140 ms. Switching among adjacent elements (i.e. beams) is expected to take about ~20 ms. Figure 4.7(b)

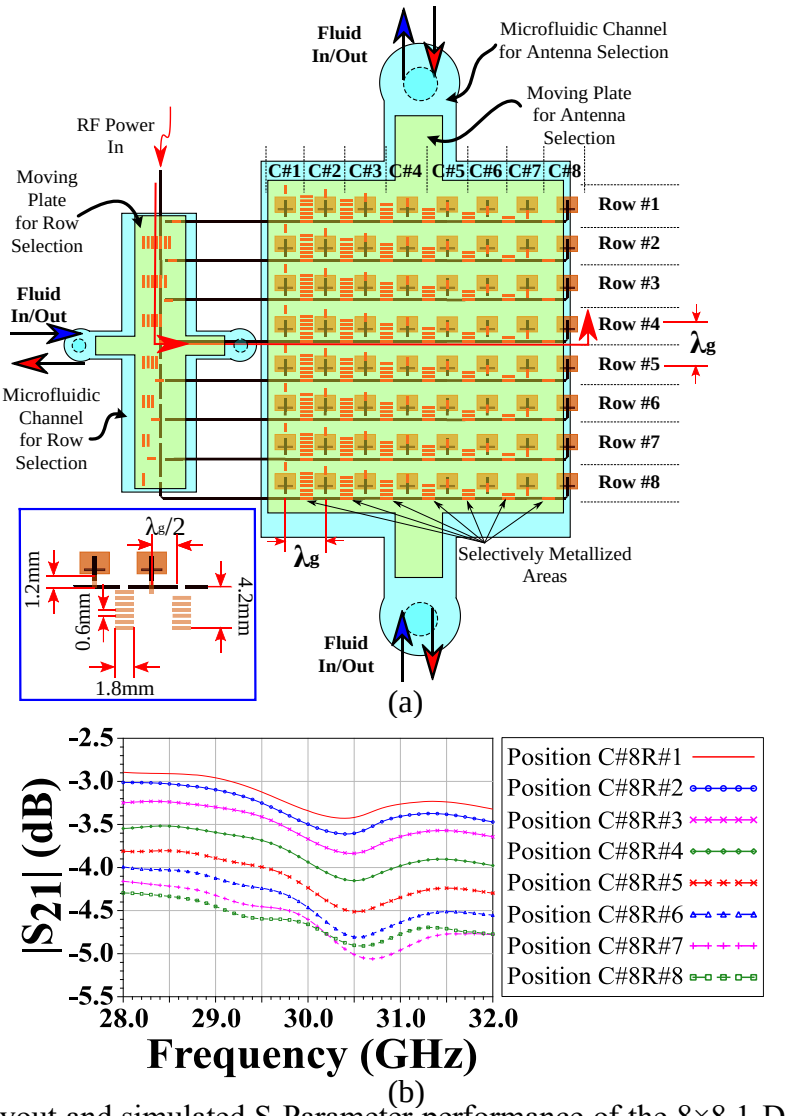

Figure 4.7. Design layout and simulated S-Parameter performance of the 8×8 1-D beam-steering MFPA. Layout of the 8×8 MFPA (a). The selectively metallized plate states are shown for the case when the aperture coupled patch antenna in row 4-column 8 is excited. Simulated worst case $|S_{21}|$ for the 8×8 MFPA feed network (b).

presents the simulated $|S_{21}|$ performance for the worst-case scenarios (i.e. last antenna location within each row of the array). Specifically, the loss is < 5.2 dB and promising for impelemntation of low-cost efficient large format high gain beam-steering mm-wave antenna arrays.

4.6. Chapter Summary

A low-loss and wideband microfluidically switched feed network is presented for mm-wave beam-steering applications. For this purpose, the microfluidically switched microstrip line

design introduced in Chapter 3 is implemented in a cascaded SP2T configuration. As compared to previous microfluidic beam-steering focal plane arrays designs, the switching time, bandwidth, and loss performances are significantly improved by replacing the need for resonant microstrip lines with microfluidic switches. With this compact microfluidically switched feed network design, a microfluidically switched beam-steering focal plane array concept has been extended for 2D beam-steering. Specifically, a simulated feed network loss < 5.2 dB is demonstrated for a 64 element (8×8) MFPA configuration.

Thanks to these advances, microfluidic reconfiguration technology demonstrated promising advantages as compared to current existing technologies (i.e. MEMS and RFICs) at mm-wave frequencies. It is possible now to reconfigure the MFPA in about 40 ms, as compared to over 5 s in previous designs. This compact ranges allow for integrated actuation mechanisms that will help solve the integration and reliability test challenges of microfluidic technology, as it will be demonstrated in the following chapters.

Chapter 5: Integrated Piezoelectric Actuation and Miniaturization of Millimeter-Wave Microfluidically Switched Microstrip Lines[4]

Although microfluidic technology has been shown to be promising for mm-wave applications in previous chapters, the lack of an integrated actuation mechanism with fast reconfiguration time continues to limit its practical use. Development of integrated actuation mechanism can also allow for long-term testing of the microfluidically reconfigurable microwave devices in order to fully assess their applicability. To address this need, a piezoelectric actuation concept is introduced to operate a miniaturized version of the microfluidically switched microstrip line from Chapter 3. The switch in Chapter 3 operated in mm-wave band width a microfluidically reconfigurable Selectively Metallized Plate (SMP) actuated within (~10 μm) microfluidic channel walls using bulky external piezoelectric pumps. However, the switch needs only an SMP displacement of 0.6 mm to provide the ON and OFF capabilities with <0.3 dB insertion loss (IL) and 20 dB isolation. These micro-scale actuation ranges needed for mm-wave device operation also motivates to pursue an integrated compact actuation mechanism that is expected to provide much smaller motion range as compared to the external pumps, but yet offer a satisfactory range for operation in mm-wave band.

Actuation of microfluidically reconfigurable RF devices has so far been performed with electrowetting [95], external micropumps [17] or syringes [81]. Among these, electrowetting has been the only technique available for integration. However, electrowetting has been applied for

[4] Portions of this chapter have been published in [93, 94]. Copyright permissions can be found in Appendix B.

liquid metals and resulted in low device efficiencies (due to inclusion of electrolytes) and slow actuation speeds (2.25 s due to long actuation distance needs [95]). Motivated from these aspects, an SMP-based mm-wave single-pole single-throw (SPST) switch is integrated with a piezoelectric actuator. Specifically, the switch layout of Chapter 3 is first redesigned to exhibit a smaller footprint to reduce the actuation distance between the ON and OFF states. The new design maintains wideband and low-loss performance at mm-wave band. A switch prototype confirms the wide-band (18 GHz) and low-loss (<0.42 dB) performance while operating with rise/fall times down to 1.12 ms. The prototype has also been actuated up to 3 million cycles with no performance degradation before the test is terminated.

5.1. Microfluidic Switch Miniaturization

The substrate stack-up and layouts of the SPST switch in its ON/OFF states are presented in Figure 4.1. The stack-up consists of a single layer of printed circuit board (PCB) and material layers used to form microfluidic channels at the top and bottom surfaces of the PCB. Microstrip line exhibiting a gap discontinuity is patterned on the top surface of the PCB. Sidewalls of a microfluidic channel are fabricated around this discontinuity and closed from the top with a solid fused silica slide after the SMP placement. The SMP metallization faces towards the microstrip line discontinuity. The SMP is covered with a 2 μm thin dielectric layer and capacitively loads the microstrip line discontinuity to approximate an RF short-circuit condition. The microfluidic channel is filled with low loss dielectric liquid Sigma-Aldrich Fluorinert FC-40 ($\varepsilon_r = 1.9$, $\tan\delta =$ 2×10-4). Current fabrication approach within our group results in ~8 μm surface roughness on microfluidic channel sidewall height. This brings the separation between the SMP metallization and microstrip line into the ~10 μm range where majority of the volume being filled by the liquid FC-40. Switching occurs as the SMP is positioned on top of the gap (ON) or moved away from

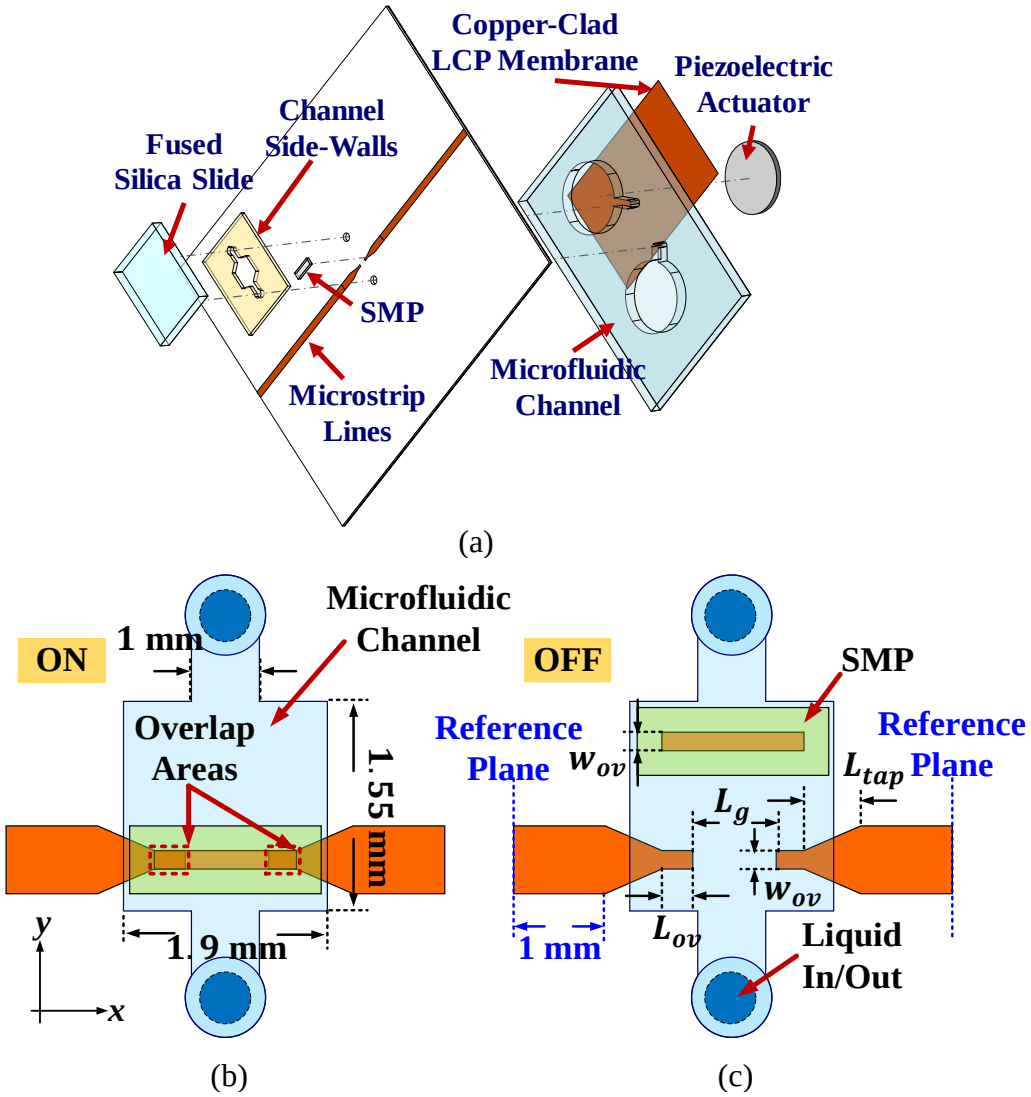

Figure 5.1. Substrate stack-up detail and design layout of the miniaturized SPST microfluidic switch. Substrate stack-up (a) and design layouts in ON (b) and OFF states (c).

the gap (OFF) actuated by the fluid motion [see Figure 5.1(b-c)]. A secondary microfluidic channel is placed below the ground plane of the PCB to realize the integrated actuation mechanism. This channel is formed from a layer of Polydimethylsiloxane (PDMS, $\varepsilon_r = 2.7$, $\tan\delta = 0.045$) and bonded to the PCB using the treatment reported in [26]. It contains two fluidic reservoirs with one of them being loaded by a piezoelectric actuator. This construction allows for a compact device since the area on the top surface of the PCB remains available for other RF functionalities. The

microstrip lines are designed to exhibit 50 Ω characteristic impedance at 30 GHz [78] and fabricated by standard photolithography on a 0.4 mm thick Rogers RO4003C substrate ($\varepsilon_r = 3.55$, $\tan\delta = 2.2\times10^{-3}$) with 17.5 µm copper cladding. The microfluidic channel sidewalls are fabricated from a 250 µm thick SU-8 2075 (MicroChem) layer ($\varepsilon_r = 3.25$, $\tan\delta = 0.017$) through standard photolithography and mask alignment features. The SMP is processed on a 0.2 mm thick Rogers RO4003C via photolithography. After etching the metallized traces, a 2 µm thin-film of Parylene N ($\varepsilon_r = 2.4$, $\tan\delta = 2\times10^{-4}$) is deposited on the SMP substrate and then cut with a dicing saw. The microfluidic channel is sealed using a 1 mm thick fused silica slide ($\varepsilon_r = 3.81$, $\tan\delta = 4\times10^{-4}$) by SU8 adhesion bonding process after the SMP placement.

An important design goal is to minimize the SMP and microstrip overlap areas. A small SMP size reduces the reconfiguration time when switching between the ON and OFF states. However, overlap areas must also be large enough to meet desired IL and impedance matching performance ($|S_{11}| <$ -10 dB). The design starts with selecting the width of the overlap areas (w_{ov}). Based on the smallest feature size that can be fabricated very reliably in available facilities, $w_{ov} = 0.15$ mm is selected. The initial estimation for the overlap length (L_{ov}) is based on the parallel plate capacitance of the overlap area (C_{ov}) neglecting fringe fields. To ensure $|S_{11}| <$ -10 dB above 25 GHz, a series 0.18 pF capacitor is required. This implies a $C_{ov} = 0.36$ pF by approximately representing the two overlap areas as two capacitors connected in series. From the C_{ov} value, overlap length is calculated as $L_{ov} = 1.4$ mm by considering a 10 µm thin dielectric layer (i.e., Parylene + FC-40) between the overlap areas and employing the parallel plate capacitor equation. Spacing between the microstrip lines (L_g) is selected as 0.8 mm to ensure >20 dB isolation at 30 GHz. The transition from 50 Ω lines to the thin overlap trace can be achieved gradually with a tapered line as seen in Figures 5.1(b) and 5.1(c). From these initial considerations,

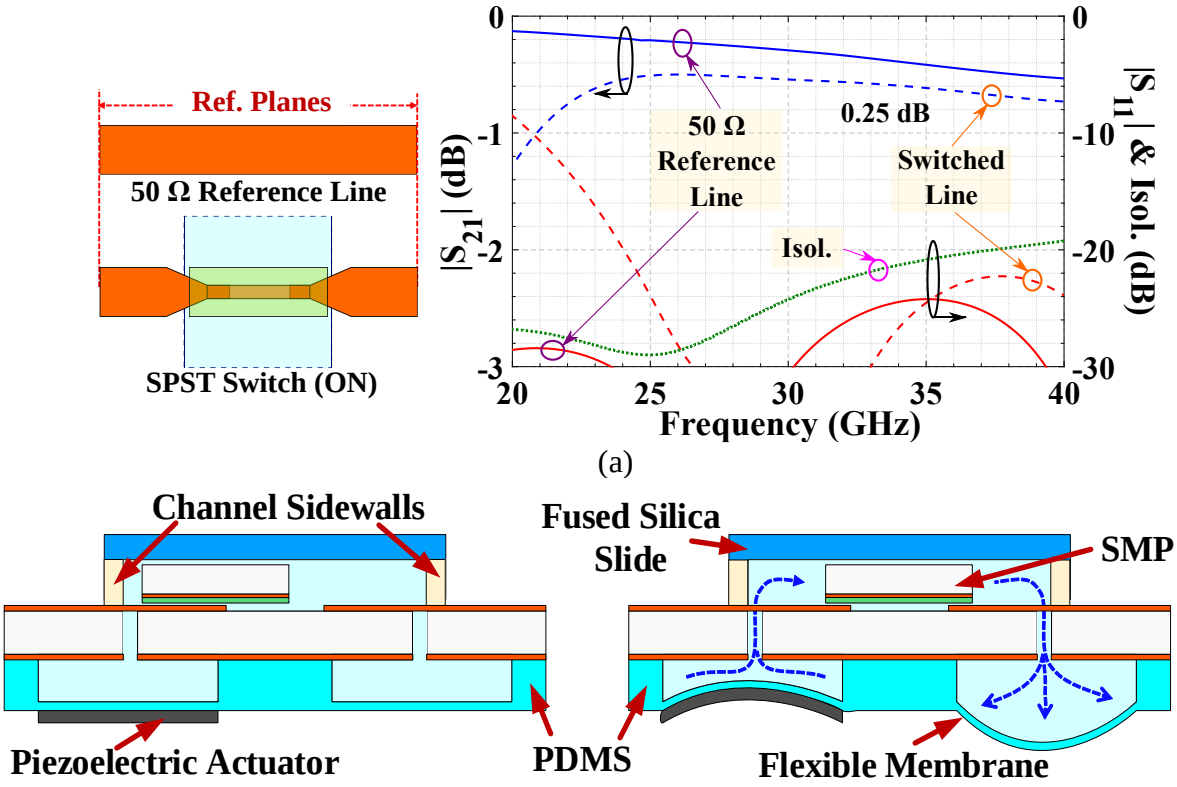

Figure 5.2. Simulated performance of the SPST microfluidic switch, and detail of the integrated actuation concept. (a) Simulated performance of the switch and comparison to a continuous 50 Ω microstrip line under the same substrate stack-up. (b) Layout of the proposed actuation mechanism with no voltage and (c) with voltage applied.

parameterized full wave simulations are carried with Keysight ADS Momentum to identify the best overall performance of the switch under different overlap and taper lengths. The dimensions obtained from these simulations are 1.25 mm for taper length and 0.25 mm for the overlap length. This implies that the metallization area of the SMP in the switch is being miniaturized from 0.49×1.8 mm^2 to 0.15×1.3 mm^2 (i.e., ~73% area reduction) as compared to the prior design demonstrated in Chapter 3.

Although $L_g = 0.8$ mm provides >20 dB isolation, the vicinity of SMP to the microstrip line gap reduces the isolation. From simulations, it is determined that SMP needs to be displaced by 0.3 mm away from the gap to achieve 20 dB isolation. Hence, SMP actuation range is 0.3 mm

and implies a 50% reduction as compared to the switch of Chapter 3. The simulated performance of the switch at the reference planes is presented in Figure 5.2(a) while being compared to a continuous 50 Ω microstrip line constructed under the same substrate stack-up. The IL performance of the switch is confirmed as 0.25 dB at 30 GHz and exhibits $|S_{11}| < -10$ dB bandwidth from 22 GHz up to 40 GHz, along with 20 dB isolation.

5.2. Integrated Piezoelectric Actuation for Microfluidic Reconfiguration

Figures 5.2(b) and 5.2(c) depict the operation principle of the piezoelectric actuation. To place the piezoelectric disk over the reservoir, a 25 µm thick copper cladded flexible liquid-crystal polymer (LCP) (Rogers ULTRALAM 3850) was patterned and bonded on top of the PDMS reservoir using the procedures reported in [26]. The copper cladding on the LCP provides a convenient technique for applying the driving voltage to the actuator. The piezoelectric actuator is bonded to the copper side of the LCP using silver epoxy (Epotek H20E). For this SPST prototype, an actuator with diameter of 12.7 mm was used. The aspect ratio variation from reservoir to the channel amplifies the out-of-plane displacement of the actuator (max 19 µm) into an in-plane SMP displacement of 0.3 mm. The liquid reservoirs are 12.5 mm in diameter, and they are connected to the top microfluidic channel by holes drilled through the microstrip substrate. Applying an actuation voltage bends the actuator and causes the fluid to push the SMP along the channel. The secondary PDMS membrane flexes to allow volume displacement. The use of hard materials in the construction of the microfluidic channel hosting the SMP avoids losses in pressure and potentially maximizes the SMP motion.

5.3. SPST Switch Protype Performance

Figure 5.3(a) shows the SPST switch prototype from the top and bottom. The S-Parameter performance of the switch is verified at the reference planes where RF edge connectors are placed.

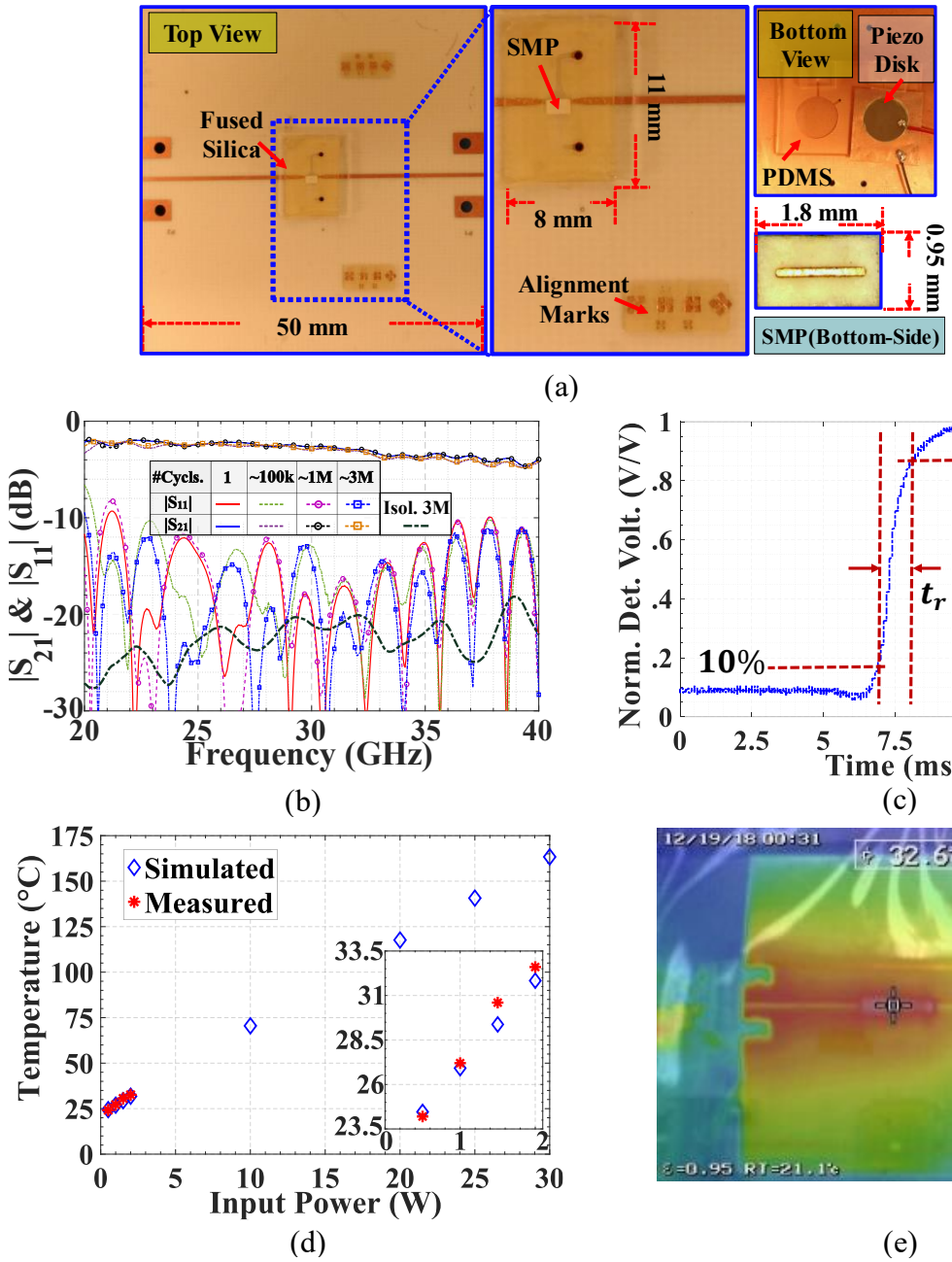

Figure 5.3. SPST switch prototype and its measured performance. Prototype (a); S-Parameter response of the test set-up (b); Measured rise time (c); Measured and simulated steady state maximum temperature on device for changing RF power (d); IR image under 20 minutes of continuous 2 W 32 GHz RF input power (e).

The IL performance is measured after applying voltage to the piezoelectric actuator and placing the SMP to its ON position. From simulations, the total IL of the microstrip extension lines are expected to be 1.25 dB at 30 GHz. Each connector introduces 0.47 dB IL based on experimental

characterization. The measured IL of the SPST switch prototype is 2.61 dB as shown in Fig 5.3(b). This implies 0.42 dB IL from the switch and agrees well with simulation-based expectation (0.25 dB). The 0.17 dB difference can be attributed to inaccuracy in material properties and errors in measurements. To test reconfiguration speed, repeatability and reliability; a measurement setup like the one reported in [96] was used. A 25 Hz square-wave signal is used to actuate the piezoelectric actuator. The lowest peak voltage (V_{pk}) that can reliably actuate the SPST switch is observed to be $\pm 27\, V_{pk}$. Under this actuation voltage, switch reconfiguration time is 3.65 ms. Increasing the actuation voltage is observed to lower this reconfiguration time. However, exceeding $\pm 52\, V_{pk}$ actuation voltage yields practically no other improvement for the reconfiguration time. Specifically, with $\pm 52\, V_{pk}$ actuation voltage, the reconfiguration time is 1.12 ms as shown in Figure 5.3(c). This indicates a 36× faster switching speed with respect to pump-based actuation in Chapter 3. Fast reconfiguration speed also allows investigating the lifetime of the switch. The switch is actuated up to 3 million cycles under RF excitation before terminating the experiments. As shown in Figure 5.3(b), the switch operates with no considerable degradation in performance. Future work will consider acquiring dedicated RF sources to investigate switch lifetime for considerably larger number of actuation cycles.

Power handling capability of the switch is evaluated with multiphysics simulations by employing ANSYS Workbench 19.1 and Electronics Desktop (HFSS). Based on steady-state thermal simulations, the switch can withstand up to 30 W of continuous RF power without requiring cooling, heat-sink attachment, or a thicker ground plane. The simulations predict a maximum temperature of 163°C under this power excitation, which is slightly below the boiling temperature (165°C) of the FC-40 liquid used inside the microfluidic channel. Other materials used within the switch construction can withstand higher temperatures. However, thermal expansion of

Table 5.1. Performance comparison of different SPST switch technologies.

Reference	**Switch Type**	**Freq. (GHz)**	**IL max. (dB)**	**Isolation (dB)**	**DC Power (mW)**	**P_{out} (dBm)**	**Reconfiguration Time**
[97]	0.13µm CMOS	30-40	1.5	24	-	12	-
[98]	PCM (GeTe)	0-20	0.6	20	92	20	0.6 ms
[17]	Microfluidic CPW	10-40	1.3	27.5	100	-	~10 ms*
[95]	Microfluidic CPW	0-11	2	10	16	-	2.25 s
This Work	Microfluidic Microstrip	22-40	0.42	20	12	43*	1.12 ms

*Simulated / Estimated

materials must also be considered, and this may be a limiting factor when operating with such higher temperatures. Figure 5.3(d) shows the simulated and measured maximum temperature observed inside the device as a function of input RF power. In experiments, the switch is kept in its ON state with 27 V actuation voltage and excited by a 2 W mm-wave power amplifier (Quinstar QPW-31403330-A0). Its thermal profile [see Figure 5.3(e)] was captured with a Keysight U5850 TrueIR. For each excitation power level, the thermal profile was taken after 20 min. of operation when a steady-state temperature distribution was reached. The measured and expected temperatures are in good agreement. Table 5.1 presents a performance comparison between the presented SPST switch and other technologies. It demonstrates superior power handling capability when compared to semi-conductors and considerably fast reconfiguration speeds as compared to other microfluidic switches.

5.4. Single-Pole Multiple-Throw Microfluidic Switches

The SPST from the previous section can be extended to a single-pole four-throw (SP4T) design as shown in Figure 5.4(a). Its simulated performance is presented in Figure 5.4(b) for the position where Port 2 is activated. The wide-band and low-loss characteristics of this switch can

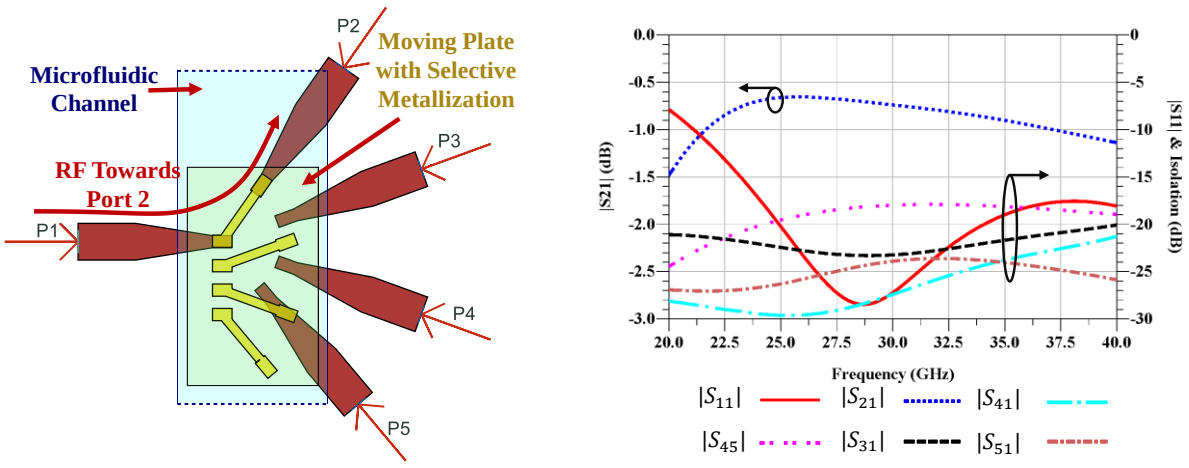

(a) (b)

Figure 5.4. Proposed SP4T design and its simulated performance. Design layout (a) and simulated performance when port 2 of the switch is connected (b).

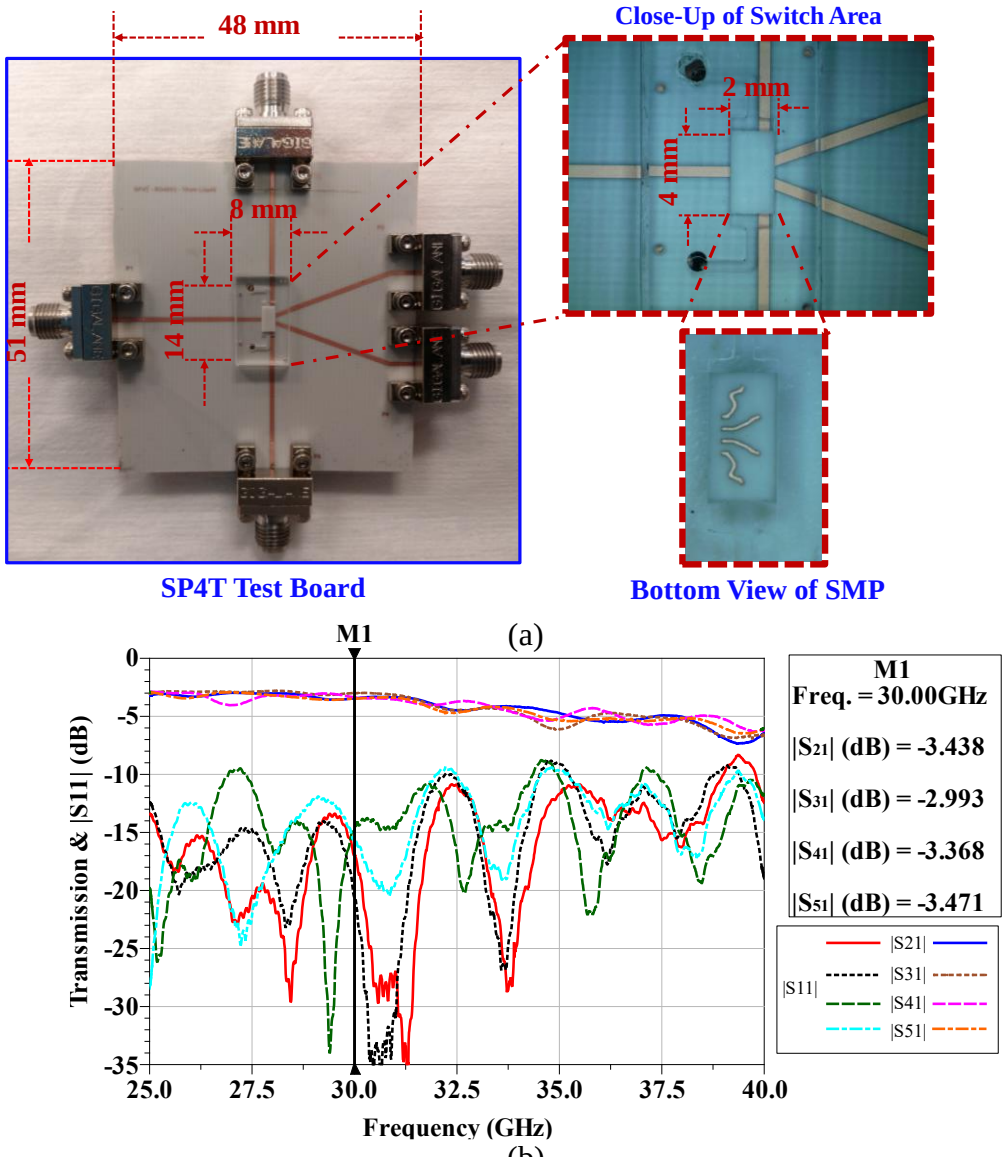

Figure 5.5. SP4T prototype and its measured S-Parameter performance. (a) SP4T prototype; (b) measured performance of the SP4T switch for its varying switch states.

be maintained in a SP4T configuration. Less than 0.7 IL at 30 GHz and over 18 dB isolation. Furthermore, such compact design will also allow for fast switching times when actuated by a piezoelectric bending disk. Additionally, these microfluidically actuated mm-wave switches can be implemented within applications towards mm-wave beam-steering. Packaging the actuator under the ground plane enables a compact footprint and allows to utilize available PCB area for other RF functionalities.

5.4.1. *Experimental Verification of the Single-Pole Four-Throw Microfluidic Switch*

The SP4T prototype is fabricated within a similar substrate stack-up as the SPST from previous section. The fabrication process is similar as explained above. The main difference is within the microfluidic channel. The channel for the SP4T is realized in a PDMS chip by soft-photolithography for rapid-prototyping purposes. Below the switch PCB, a microfluidic channel with an integrated piezoelectric actuator, similar as with the SPST, enables the motion of the SMP. Figures 5.5(a) and 5.5(b) show a close-up view of the prototype and its measured performance respectively. The meandered lines observed for the SMP in Figure 5.5(a) improve isolation performance of the switch. The SP4T switch exhibits <0.9 dB IL at each ON position and >18 dB isolation at 30 GHz. Additionally, it exhibits >18 GHz operational bandwidth (BW) with $|S_{11}| < -10$ dB.

5.4.2. *Microfluidically Switched Beam-Forming Network with Integrated Actuation*

Having a compact microfluidic switching design allows for the integration of the switching mechanism into a beam-forming network at mm-wave frequencies. One such network can be

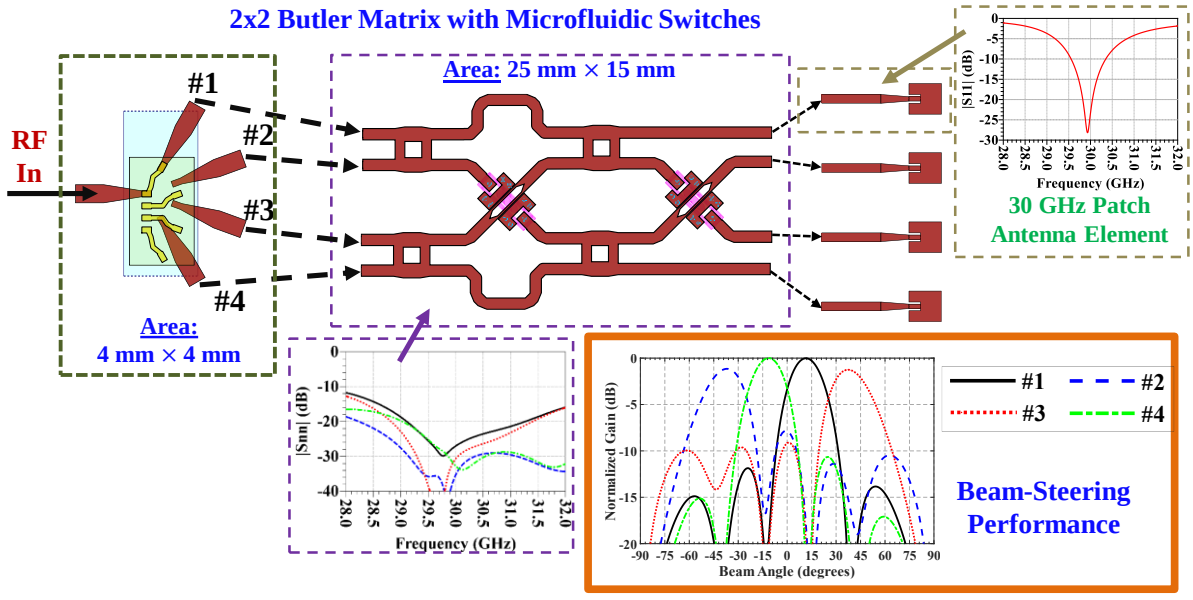

Figure 5.6. Proposed SP4T design integrated within a 4×4 Butler matrix beam-forming network.

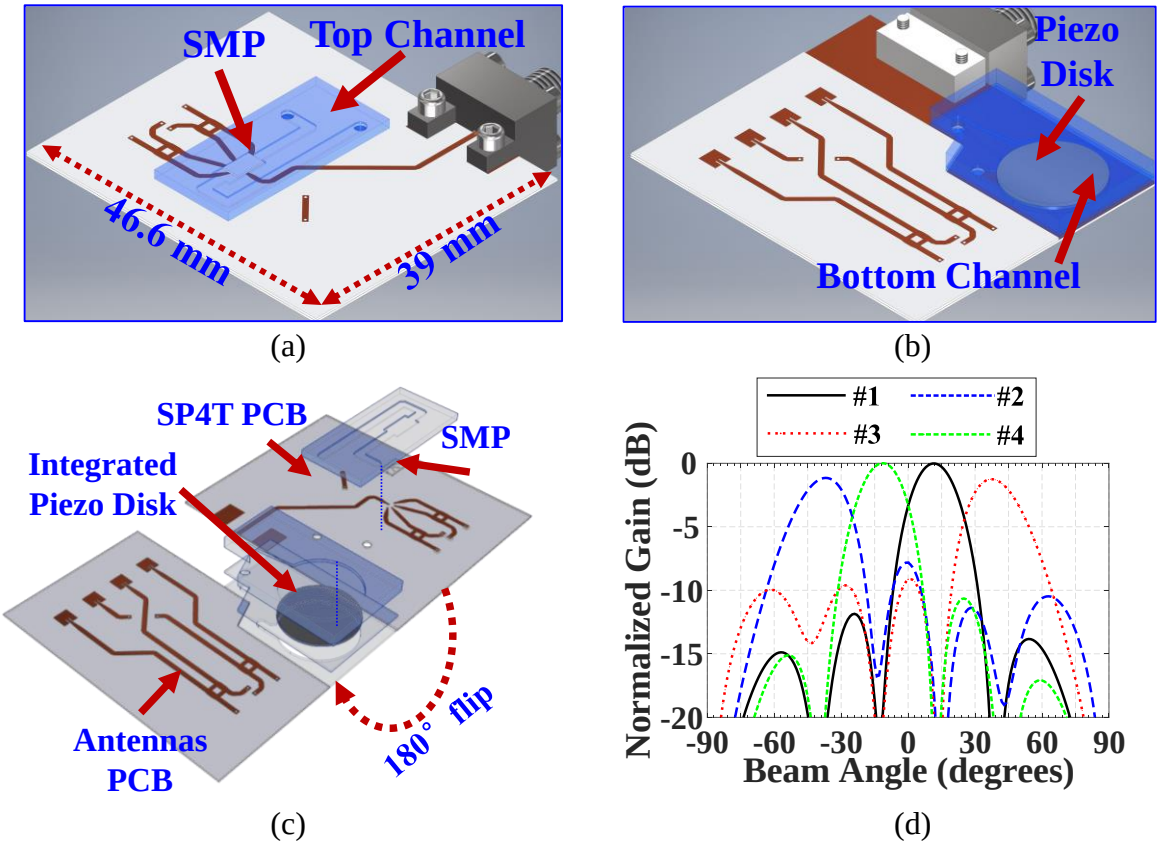

Figure 5.7. Integrated SP4T and compact actuation mechanism for mm-wave beam-steering. Top-isometric view (a) and bottom-isometric view (b). Detailed/exploded view of the array (c) and simulated beam-steering performance (d).

realized with 4×4 Butler matrix configuration such as the one presented in Figure 5.6. This design allows for 1D beam steering with a ±45° field-of-view within four beam positions as the switch is operated. Furthermore, the SP4T and actuation mechanism can be integrated to form a compact beam-steering antenna array as shown in Figure 5.7(a) and 5.7(b). This integration makes use of a 4×4 Butler matrix similarly as shown in Figure 5.6. The design of the array is based on stacking two PCB substrates with a common ground plane. The bottom and top metallization surfaces of the PCB carry the two halves of the Butler matrix. These halves are connected to each other with metallized vias. The SP4T switch is placed on the opposite side of the antenna elements while piezoelectric disk is on the same surface with the elements [a detailed view of the PCB layers and actuation mechanism is offered in Figure 5.7(c)]. However, it is important to note that different

arrangements are also possible with the proposed switches. Beam-steering performance is shown in Figure 5.7(d). Based on full wave simulations, the array is expected to perform with 10.2 dBi realized gain and 13% $|S_{11}| < -10$dB BW.

5.5. Chapter Summary

A low-loss and wideband microfluidic switch actuated with an integrated and compact piezoelectric mechanism is presented. The SPST switch prototype demonstrates 0.42 dB IL with an operating bandwidth from 22 to 40 GHz. A piezoelectric actuation mechanism is successfully integrated for the first time in an SMP-based microfluidic device. The integrated piezoelectric actuation enables reliability and reconfiguration time characterization of the prototype. The SPST switch demonstrates 1.12 ms switching time, making it the fastest microfluidically-actuated switch reported to date. Furthermore, the prototype is operated up to ~3×10^6 switching cycles with no apparent performance degradation. Additionally, power handling measurements show the potential of microfluidic switches based on the SMP approach to provide >43 dBm at mm-wave frequencies. The SPST design is demonstrated to be scalable for multi-throw operations with an SP4T design that maintains similar IL and wideband performance as the SPST in a compact package. The SP4T switch is subsequently used to develop a 4-element mm-wave beam-steering antenna array demonstrating the advanced capabilities of integrating the microfluidic actuation mechanism in compact device.

Chapter 6: Microfluidically Reconfigurable Millimeter-Wave Hairpin Band-Pass Filters with Integrated Actuation for Continuous Bandwidth and Frequency Control[5]

The realization of integrated actuation of microfluidic devices via piezoelectric bending actuators [93], as demonstrated in Chapter 5, has eliminated the need for bulky external micropumps and provided a path for compact designs of microfluidically reconfigurable RF devices. Additionally, the integrated actuation is made possible due to the advantage of reduced device size at mm-wave frequencies, where small deflections by the piezoelectric actuator (e.g. tenths to hundredths of μm) can be transformed into several millimeters of liquid motion. This has enabled microfluidic devices with reconfiguration times of about 1 ms [93]. The integrated actuation provides additional design flexibility by allowing the microfluidic device to be fully packaged in one compact structure using thin-film and multi-layered fabrication techniques. Simultaneously, by utilizing integrated piezoelectric actuators that enable device reconfiguration times in the millisecond range, it is now possible to realize reliability and repeatability tests in the order of millions of cycles [93]. All these advantages allow the opportunity to expand the concept of microfluidic reconfiguration via Selectively Metallized Plates (SMPs) with integrated actuation, presented in Chapter 5, into reconfigurable filters with frequency tuning and bandwidth control. Piezoelectric actuators can be used to drive two separate microfluidic channels as seen in Figure 6.1(a), to provide independent control of frequency and bandwidth while maintaining a relatively small footprint for mm-wave applications.

[5] Portions of this chapter were submitted to IEEE Transactions on Microwave Theory and Techniques.

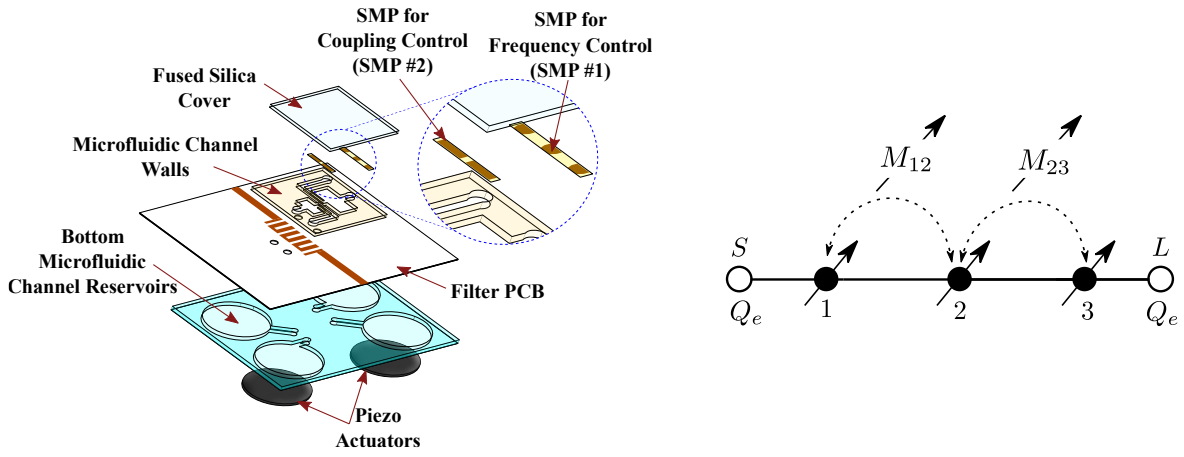

(a) (b)

Figure 6.1. Microfluidically tunable filter design concept with frequency and bandwidth reconfiguration. Substrate stack-up of the frequency and bandwidth tunable filter with integrated actuation (a); Coupling diagram (b).

The major contributions of this chapter are (i) to demonstrate, for the first time, the capabilities of SMP-based microfluidic reconfiguration of filters at mm-wave frequencies; (ii) introduce a microfluidically reconfigurable filter design with independent and continuous control of frequency and bandwidth at mm-wave frequencies; and (iii) investigate reliability, reconfiguration speed, and power handling performance of the microfluidically reconfigurable. For these purposes, this chapter discusses three separate filter designs and prototypes. The first design is a frequency tunable band pass filter (FT-BPF). The second design is a bandwidth tunable band pass filter (BT-BPF). The third design can be considered as combination of the two filters providing bandwidth and frequency tuning capabilities simultaneously (FBT-BPF). The filter topology is based on a third order coupled resonator BPF where resonance frequencies and inter-resonator couplings must be simultaneously tuned for the desired functionalities [see Figure 6.1(b)]. The frequency tuning range is selected to be 28 GHz – 38 GHz band due to emerging interest in mm-wave communications. The FT-BPF is designed to maintain a constant 7% fractional bandwidth (FBW) within the band. This is motivated from the bandwidth of 28 GHz (e.g. 27 GHz – 29 GHz and 26.5 GHz – 29.5 GHz) and 38 GHz (e.g. 36.5 GHz – 39.5 GHz and

37 GHz – 41 GHz) frequency bands [16, 17]; however, different design specifications can also be pursued. The BT-BPF design carried out at 38 GHz. The filter offers 7% to 16% FBW control. The FBT-BPF design operates with frequency tuning range from 28 GHz to 38 GHz while achieving bandwidth tunability from 7% to 12% at 28 GHz and 7% to 16% at 38 GHz. It is shown that the filter prototypes perform with worst-case insertion loss (IL) of 3.1 dB at 38 GHz. They offer 7.8%–16.7% 3 dB FBW tunability at 38 GHz and 7%–12% 3dB FBW tunability at 28 GHz. A reconfiguration speed of 285 MHz/ms is achieved and actuation cycles up to 12 million are demonstrated. The FBT-BPF is characterized to handle up to 5 W of continuous RF power without needing thick ground planes or heat sinks.

6.1. Frequency and Bandwidth Tuning Principles

The coupling diagram in Figure 6.1(b) demonstrates the concept of achieving frequency and bandwidth tunability from a third order BPF. Resonance frequencies of the resonators and their inter-resonator coupling coefficients must be controllable. For a symmetrical filter response, the coupling coefficients M_{12} and M_{23} need to be equal along with synchronized resonance frequencies. External quality factor (Q_e) and coupling coefficients can be determined from the coupled resonator filter theory [99] to achieve the desired filter response and FBW. For well-known filter types (such as Chebyshev and maximally flat), the link between low-pass filter prototype and coupling coefficients is already established [99].

Frequency tunability of microwave filters is commonly achieved by capacitively loading the resonators or modifying the physical dimensions of the resonators. A well-known approach for capacitive loading based frequency tunability is microstrip combline topologies implemented with varactors [100]. A similar capacitive loading approach is demonstrated with microfluidics in [25] where the repositionable SMP metallizations act as the varactors loading the resonators. A well-

known approach for physical dimension variation based frequency tunability is the semiconductor [101] or MEMS switch loaded resonators [102]. Physical variation based frequency is tuning is also shown to be possible with microfluidics in [27] where repositionable SMP acts as the resonator itself. Bandwidth tunability of microwave filters is also commonly achieved with capacitive loading to modify the inter-resonator couplings. Simultaneous frequency and bandwidth control increases the number of the control elements (i.e. varactors and/or switches) and penalizes the IL of the filter. This becomes high in mm-wave frequencies with IL values reaching up to 9 dB at 20 GHz (see Table 6.1 in Section 6.7 for comparison of state of the art and presented filters). On the other hand, frequency and/or bandwidth tunable filters have never been implemented in mm-wave frequencies with microfluidics. As will be shown, these filters can offer significant advantages in IL and power handling capability from a compact footprint.

Implementing independent control for frequency and bandwidth tunability with microfluidics necessitates to utilize two distinct SMPs within two separate microfluidic channels. Therefore, the coupled resonator filter topology consisting of hairpin resonators is proposed as shown in Figure 6.1 and Figure 6.2. The hairpin resonators allow to use an SMP to simultaneously load the open ends of the resonators for achieving frequency tunability [see Figure 6.2(a) SMP #1]. Another SMP can be used at the opposite sides of the hairpin resonators to control inter-resonator couplings through capacitive loading [see Figure 6.2(b) SMP #2]. Having SMPs at opposite sides of the resonators allows to realize the filter by making use of meandered microfluidic channels. The channel layout demonstrating this operation is also highlighted with dashed lines in Figure 6.2. Each microfluidic channel can be interfaced with a piezoelectric actuator at the back of the ground plane to provide individual control of the SMP positions as shown in 3D perspective view of the filter in Figure 6.1.

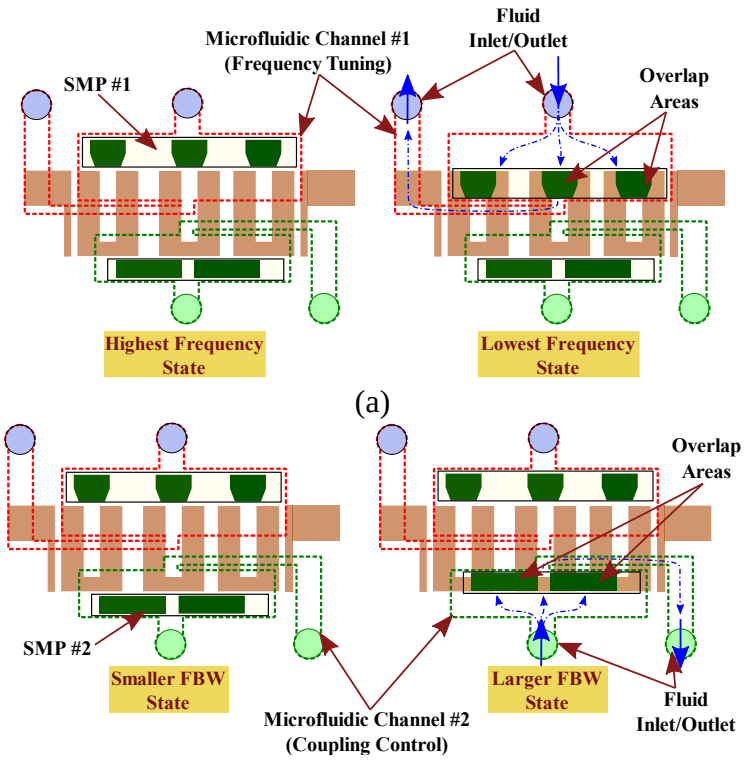

Figure 6.2. Filter layouts demonstrating frequency and bandwidth reconfiguration. (a) Frequency reconfiguration with SMP #1 (SMP #2 is taken to be not loading the filter); and (b) bandwidth reconfiguration with SMP #2 (SMP #1 is taken to be not loading the filter).

Figure 6.3(a) shows the equivalent circuit of two adjacent resonators loaded with the SMPs. In this circuit model, each hairpin resonator is represented with a parallel L_0C_0 network. These resonators in general exhibit mixed magnetic and electric couplings. However, for the selected geometry and orientation of adjacent resonators, the electrical coupling dominates for small resonator spacing [103] and the performance of the equivalent circuit gets dominated by the electrical coupling capacitance C_m. Within the circuit, coupling is represented with an admittance inverter network. The capacitive loading between the two resonators generated by the metal trace of the SMP #2 is represented with a variable capacitor C_C placed in parallel with the admittance inverter network. The capacitive loading introduced by the SMP #1 metal trace across the open ends of the resonator is represented with the variable loading capacitor C_L. The resonance frequency of the resonator is given by:

$$f_0 = \frac{1}{2\pi\sqrt{L_0(C_0 + C_L)}} \tag{6.1}$$

Keysight ADS Momentum suite is used for electromagnetics (EM) simulations to design the unloaded resonator operate at 38 GHz. Co-simulation is performed and the C_L value that reduces the resonance frequency down to 28 GHz is identified as 0.3 pF (i.e. 0.3 pF > C_L > 0 for 28 GHz > f_0 > 38 GHz). Co-simulations and Equation 6.1 is utilized at different operation frequencies to extract L_0 and C_0 as 48.314 pH and 0.363 pF, respectively. Afterwards, C_L must be related to the SMP metallizations to realize the filter. For design simplicity, in this work, the C_C

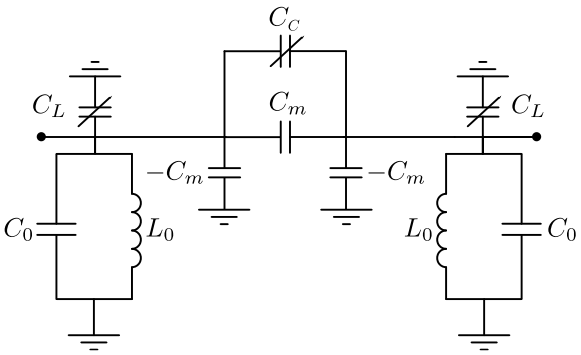

(a)

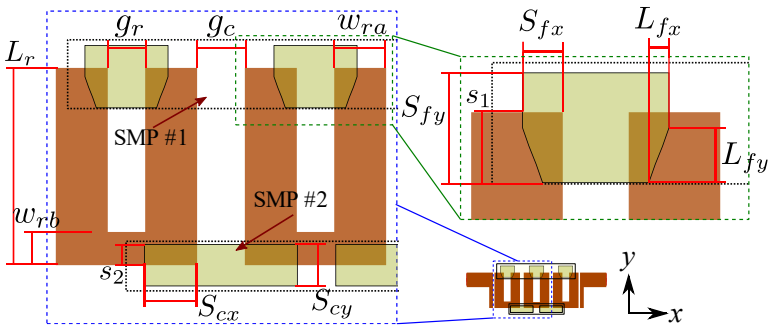

(b)

Figure 6.3. Equivalent circuit model and layout detail of a resonator pair. (a) Equivalent circuit model of a coupled resonator pair and (b) layout detail of the resonator pair when loaded with SMP metallizations (L_r = 0.95, w_{ra} = 0.25, w_{rb} = 0.16, g_r = 0.18, g_c = 0.1, S_{fx} = 0.105, S_{fy} = 0.3, L_{fx} = 0.055, L_{fy} = 0.15, S_{cx} = 0.25, S_{cy} = 0.175, $0 \geq s_1 \geq S_{fy}$, $0 \geq s_2 \geq S_{cy}$; all units are in mm).

and C_L are related to SMP metallizations through the parallel plate capacitor equations. As shown in Figure 6.3(b), the metal trace of SMP #1 overlaps with the open ends of the hairpin resonator with an area proportional to $S_{fx} \times S_{fy}$, where S_{fx} and S_{fy} denote the maximum horizontal and vertical overlap lengths of the SMP #1 metallization with respect to the resonator, respectively. Parameter s_1 defines the position of SMP #1 relative to the resonator (e.g. $s_1 = 0$ implies no overlap and $s_1 = S_{fy}$ implies maximum overlap). The shape of the metal traces of SMP #1 is partially trapezoidal to linearize the frequency tuning with respect to s_1 as was similarly employed in [27]. The parameters L_{fx} and L_{fy} shown in Figure 6.3(b) describe the shape of the partial trapezoidal area. The relationship between the total overlap area (A_{C_L}) and C_L is:

$$C_L = \frac{\varepsilon_r \varepsilon_0 A_{C_L}}{4d} \tag{6.2}$$

where d is the vertical separation between the SMP metallizations and printed circuit board (PCB) traces forming the resonators (d = 10 μm); and ε_r is the relative dielectric constant of the material separating the SMP metallizations and PCB traces (ε_r = 2.15). From the described geometry in Figure 6.3(b), A_{C_L} is linked to the geometry as:

$$A_{C_L} = \begin{cases} 2(S_{fx} - L_{fx})s_1 + \dfrac{L_{fx}s_1^2}{L_{fy}} & \text{for } s_1 < L_{fy} \\ 2S_{fx}s_1 - L_{fx}L_{fy} & \text{for } s_1 \geq L_{fy} \end{cases}. \tag{6.3}$$

The factor of 4 in Equation 6.2 appears due to the C_L being formed through the series connection of two capacitors defined by the half of the total overlap area. Figure 6.4(a) presents the relationship between s_1 and f_0. This relationship is obtained from EM simulations. Frequency

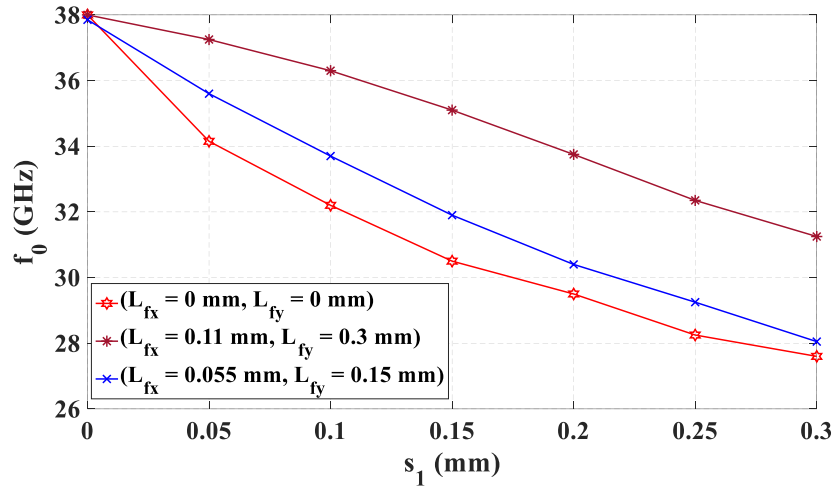

(a)

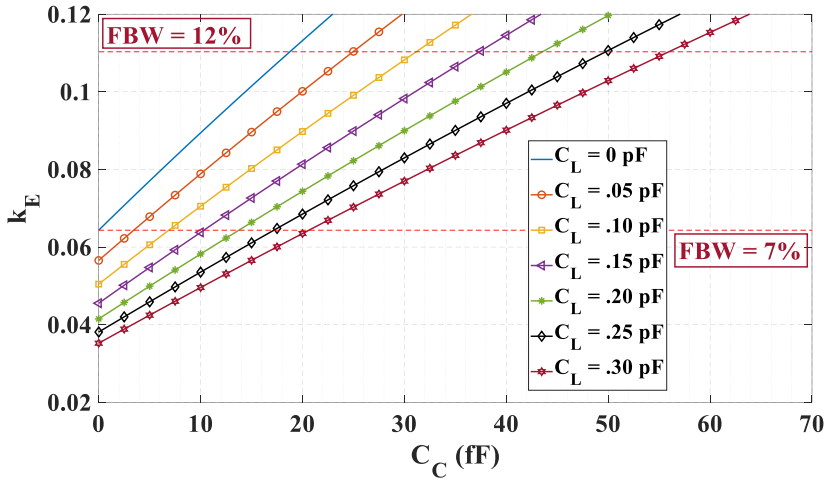

(b)

Figure 6.4. Frequency linearization of the hairpin resonator and coupling factor variation with respect to the coupling capacitances introduced in the design. (a) Resonance frequency variation of the hairpin resonator as a function of SMP #1 position s_1 with different L_{fx} and L_{fy} parameters used in defining the SMP #1 metallization; (b) Coupling as a function of C_L and C_C.

variation with s_1 can be linearized by utilizing the L_{fx} and L_{fy} parameters. In the design, S_{fx} is selected as 0.11 mm due to the need to include coupling compensation traces in SMP #1 (see Section 6.2 for coupling compensation discussion). With this value of S_{fx}, L_{fx}= 50 µm and L_{fy} = 0.15 mm achieves an almost linear frequency variation behavior with respect to s_1. Subsequently, S_{fy} is determined as 0.3 mm from Equations 6.2 and 6.3 by making using of the maximum value of C_L = 0.3 pF at $s_1 = S_{fy}$.

To achieve the desired minimal FBW tunability of 9.5% $\pm$ 2.5%, the tunability range of C_C must be determined. C_C is proportional to the area $S_{cx} \times S_{cy}$ formed by overlapping metal trace of SMP #2 with the hairpin resonator. Here, S_{cx} and S_{cy} denote the maximum horizontal and vertical overlap lengths of the SMP #2 metallization with respect to the resonator. Parameter s_2 defines the position of SMP #2 with respect to the resonator (e.g. s_2 = 0 implies no overlap and $s_2 = S_{cy}$ implies maximum overlap). The total overlap area A_{C_C} for C_C is rectangular since this shape is found to readily provide a linear coupling variation with s_2. The relationship between A_{C_C} and C_L is:

$$C_C = \frac{\varepsilon_r \varepsilon_0 A_{C_C}}{4d}, \tag{6.4}$$

From the described geometry in Figure 6.3(b), A_{C_C} is linked to the geometry as:

$$A_{C_C} = 2S_{cx}s_2 \tag{6.5}$$

From the equivalent circuit of Figure 6.3(a), with the approach described in [99], the electrical coupling factor k_E is expressed as:

$$k_E = \frac{f_m^2 - f_e^2}{f_m^2 + f_e^2}, \tag{6.6}$$

where:

$$f_e = \frac{1}{2\pi\sqrt{L_0(C_0 + C_m + C_L + 2C_C)}} \tag{6.7}$$

$$f_m = \frac{1}{2\pi\sqrt{L_0(C_0 + C_L - C_m)}} \tag{6.8}$$

Equations 6.1 and 6.6 – 6.8 show that C_L reduces k_E while also reducing f_0. Therefore, dependence of k_E to C_C must be extracted for different values of C_L as shown in Figure 6.4(b). To determine required k_E, a filter topology must be selected. In this manuscript, we pursue a third-

order 0.1 dB ripple Chebyshev filter with minimal FBW tunability from 7% to 12%. From [84], low-pass prototype element values can be obtained as $g_0 = g_4 = 1$, $g_1 = g_3 = 1.0316$ and $g_2 = 1.1474$. For FBW of 7%, $Q_e = 14.74$, $M_{12} = M_{23} = 0.06434$. For FBW of 12%, $Q_e = 8.597, M_{12} = M_{23} = 0.1103$. Therefore, k_E needs to be tunable within the range of 0.064 – 0.11. Minimum FBW is achieved when C_C = 0. As described in introduction, a design goal is to maintain minimum FBW as 7% at all possible center frequencies. To achieve this, $C_L = 0$ and C_C = 0 point in Figure 6.4(b) is adjusted with the choice of C_m = 23.36 fF to provide the minimum required k_E of 0.064. As seen in Figure 6.4(b), for $C_L = 0$, C_C must be varying from 0 to 20 fF to increase the FBW from 7% to 12%. In the case of C_L = 0.30 pF, C_C needs to vary from 20 fF to 60 fF to tune FBW from 7% to 12%. In the following section, coupling capacitive loading ranging from 0 to 20 fF will be provided with SMP #1 metallizations to ensure a constant FBW filter with minimum of 7% FBW. SMP #2 metallizations will be designed to provide coupling capacitance tunability ranging from 0 fF to 40 fF. For realizing C_C, S_{cx} is chosen as the resonator arm width $w_{ra} = 0.25$ mm. and S_{cy} is calculated from Equations 6.4 and 6.5 for C_C = 40 fF at $s_2 = S_{cy}$. Figure 6.4(b) also demonstrates that k_E depends almost linearly to C_C, thus, justifying the use of rectangular area for coupling capacitors.

Figure 6.5 presents the substrate stack-up used to design the filter in Keysight ADS Momentum. A 203 µm Rogers RO4003C substrate ($\varepsilon_r = 3.55$, $\tan\delta = 2.7\times10^{-3}$) with 17.5 µm copper-cladding is used for the PCB hosting the resonators. A 5 µm thick layer is used to represent the liquid between the PCB and SMP metallizations. The liquid is Sigma-Aldrich Fluorinert FC-40 ($\varepsilon_r = 1.9$, $\tan\delta = 2\times10^{-4}$). The thickness of this liquid layer is due to the fabrication tolerances in realizing the height of the microfluidic channels. A 5 µm thick Parylene N ($\varepsilon_r = 2.4$, $\tan\delta = 2\times10^{-4}$) layer is deposited on the SMP metallizations to ensure a dielectric insulation between

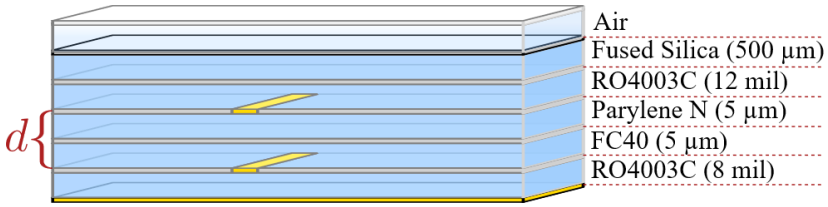

Figure 6.5. Substrate stack-up used for Keysight ADS Momentum EM simulations.

SMP and the PCB metallizations. A 0.305 mm thick Rogers RO4003C substrate is selected for the SMP. The channel is sealed with a 0.5 mm thick fused silica substrate ($\varepsilon_r = 3.81$, $\tan\delta = 4\times10^{-4}$).

Figure 6.3(b) shows the physical dimensions of the resonator designed to operate at 38 GHz in its unloaded state within the selected substrate stack-up. Through EM simulations, inter-resonator spacing is determined to be $g_c = 0.1$ mm to provide the desired k_E. The SMP metallization dimensions determined from the circuit analysis are slightly tuned in ADS simulations to provide the desired frequency and bandwidth tuning. The finalized dimensions of the SMP metallization areas are also provided in Figure 6.3(b). The resonator is expected to provide an unloaded quality factor of $Q_u \approx 115$.

6.2. Frequency Tunable Constant FBW Filter Design

The design of the resonator is already detailed in previous section. The constant 7% FBW frequency tunable filter layout is shown in Figure 6.6(a). As detailed before, SMP #1 metallization includes traces to compensate for the inter-resonator coupling coefficient as the frequency is lowered with s_1 motion. The range of the compensation is 0 to 20 fF and should be varying linearly with s_1. Therefore, the dimensions of these coupling compensation metallizations can be initially determined by making use of Equations 6.3 and 6.5 as $S_{fx} = 0.1$ mm and $S_{fy} = 0.3$ mm. The finalized dimensions obtained through simulations is given in Figure 6.6(a).

Additionally, maintaining a constant 7% FBW across the entire frequency tuning range requires to stabilize the Q_e. The filter is fed with a capacitively coupled microstrip line that is

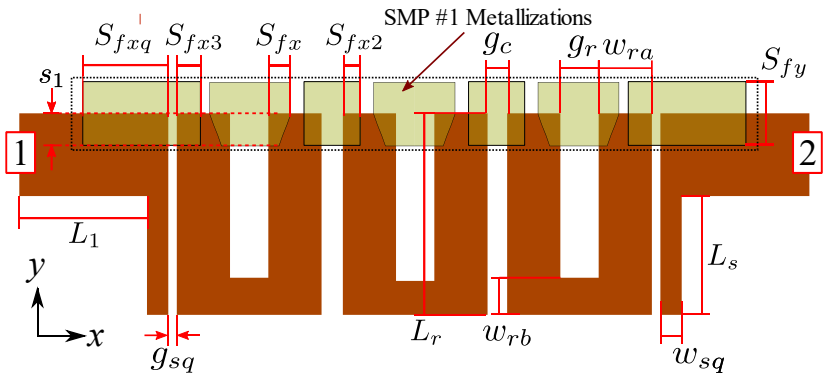

(a)

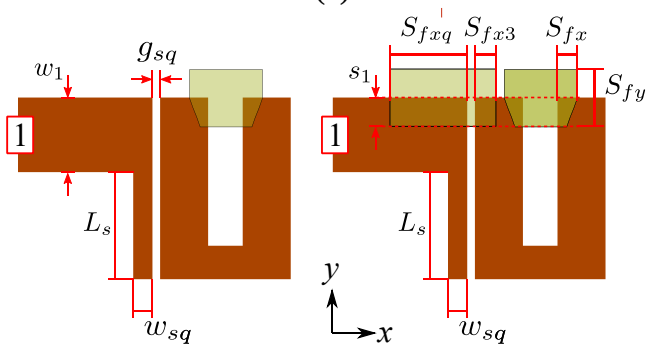

(b)

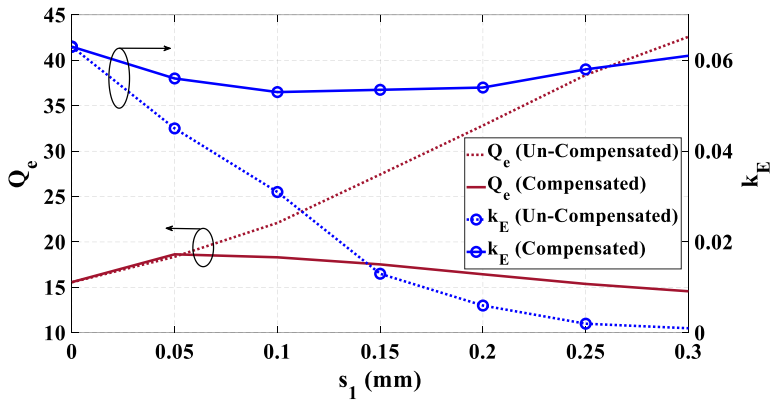

(c)

Figure 6.6. Layout of the FT-BPF and extracted external quality and coupling factors for filter design. (a) Layout for the FT-BPF filter with 7% constant FBW; (b) Q_e compensation scheme; (c) Q_e and k_E with and without SMP #1 coupling compensation metallizations. ($L_1 = 0.6$, $w_1 = 0.39$, $L_r = 0.95$, $w_{ra} = 0.25$, $w_{rb} = 0.16$, $g_r = 0.18$, $g_c = 0.1$, $S_{fx} = 0.105$, $S_{fy} = 0.3$, $L_{fx} = 0.055$, $L_{fy} = 0.15$, $L_s = 0.56$, $w_{sq} = 0.1$, $g_{sq} = 0.04$, $S_{fxq} = 0.4$, $S_{fx2} = 0.08$, $S_{fx3} = 0.11$, $0 \leq s_1 \leq S_{fy}$; dimensions are in mm).

terminated in a shunt open-circuited stub. The stub serves two purposes: (i) stabilize the Q_e for lower frequencies similarly as in [3]; and (ii) provide a point where additional capacitive coupling

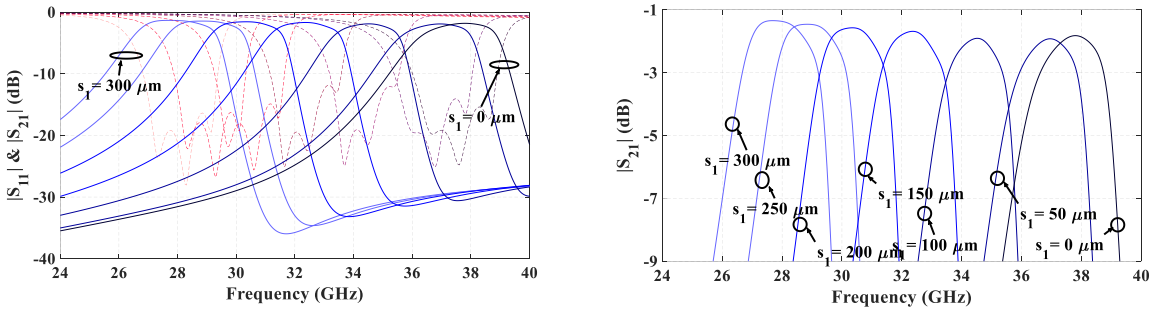

(a) (b)

Figure 6.7. Simulated performance of the FT-BPF. (a) $|S_{21}|$ and $|S_{11}|$; (b) close-up view of $|S_{21}|$ as a function of SMP #1 position s_1.

can realized between the input/output line and the resonator through SMP #2 metallizations (see Section 6.3). The stub dimensions L_s and w_{sq} are designed to provide a stable Q_e as s_1 increases, following a similar approach as in [3]. Without any modifications, Q_e increases as resonance frequency of the filter is lowered. This is similar to the inter-resonator coupling and associated with the reduction in coupling capacitance. Therefore, additional metallization traces are added into the SMP #1 to gradually compensate for the reduced coupling ta the input ports of the filter. The detailed layout of the input side of the filter is provided in Figure 6.6(b). For stabilizing Q_e, S_{fqx} = 0.4 mm is selected to maximize the capacitance between SMP #1 trace and input feed line. This allows to use smallest possible overlap length S_{fx3}. Through simulations this length is found as 0.11 mm. Figure 6.6(c) demonstrates that the effectives of coupling compensation traces included in the SMP #1. Specifically, the variation of the Q_e is stabilized to be around 16.6±2. Likewise, k_E is maintained within the 0.058±0.006 range. The simulated S-Parameters of the filter are shown in Figure 6.7 for s_1 varying from 0 to 0.3 mm in 0.05 mm steps. The filter operates as desired with 28 GHz to 38 GHz frequency tunability. It operates with almost constant FBW at 7.68±0.39% due to the slight variations in k_E and Q_e. The IL of the simulated filter is 1.37 dB at 28 GHz and 1.83 dB at 38 GHz.

6.3. Bandwidth Tunable Filter Design

The design of the bandwidth tunable filter follows from the constant FBW frequency tunable filter presented in the previous section. The layout of the filter is shown in Figure 6.8(a). SMP #1 that is responsible for the frequency tuning functionality is removed. Hence, the center frequency of the filter is that of the unloaded filter and it is 38 GHz. SMP #2 is included in the

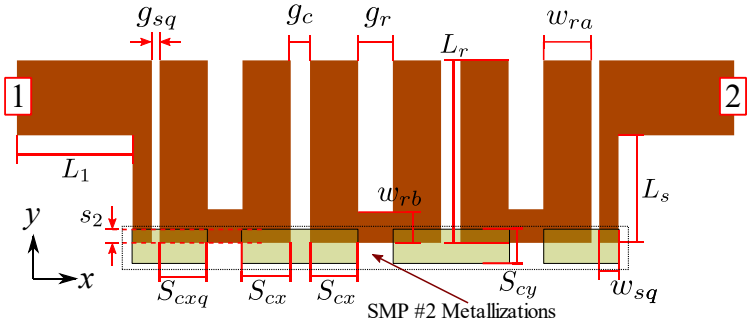

(a)

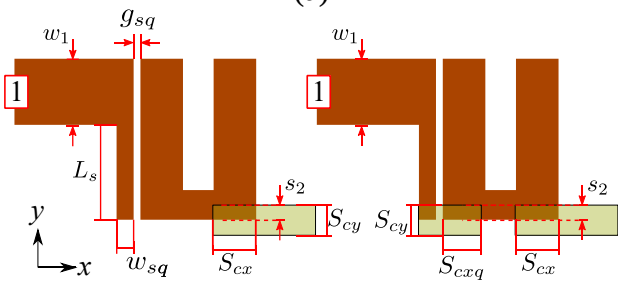

(b)

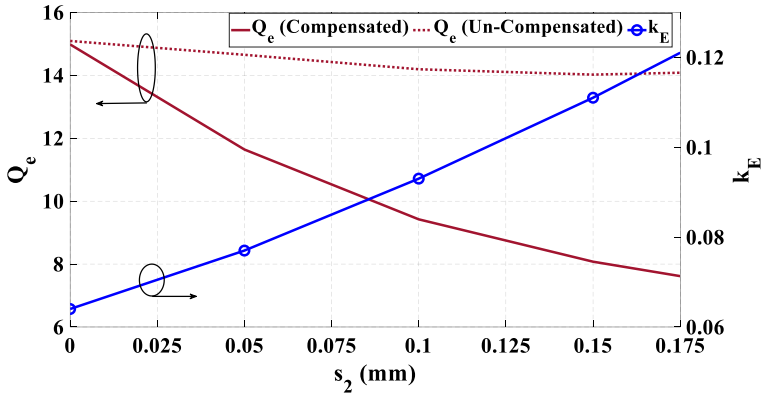

(c)

Figure 6.8. Layout of the BT-BPF and extracted external quality and coupling factors for filter design. (a) Layout of the BT-BPF; (b) Q_e compensation scheme; (c) Q_e and k_E with and without SMP #2 coupling compansation metallizations. ($L_1 = 0.6$, $w_1 = 0.39$, $L_r = 0.95$, $w_{ra} = 0.25$, $w_{rb} = 0.16$, $g_r = 0.18$, $g_c = 0.1$, $S_{cx} = 0.25$, $S_{cy} = 0.175$, $L_s = 0.56$, $w_{sq} = 0.1$, $g_{sq} = 0.04$, $S_{cxq} = 0.25$, $0 \leq s_2 \leq S_{cy}$; dimensions are in mm).

layout for bandwidth tunability. Two of the SMP #2 rectangular traces are responsible for tuning the inter-resonator couplings. The size of these traces (i.e. S_{cx} and S_{cy}) are designed in Section 6.1 to provide FBW tuning from 7% to 12% at 28 GHz. At 38 GHz, these traces increase k_E from 0.062 to 0.12 as SMP #2 is repositioned. Therefore, the FBW tunability extends from 7.6% to 17.6% when Q_e of the input/output resonators are properly adjusted.

Relative position of SMP #2 with respect to the resonators on the PCB is denoted with s_2 as explained in Section 6.1. To maintain impedance matching across different values of s_2 (i.e. different values of FBW), a Q_e reduction scheme is introduced similar to the approach followed in the design of the constant FBW frequency tunable filter. Specifically, SMP #2 hosts metallized traces that overlap with the input/output microstrip lines/stubs and resonators to provide increased capacitance as s_2 is increased. The overlap area is defined with parameters w_{sq}, S_{cxq}, and s_2. w_{sq} is set with the design of the coupling stub placed at the input/output microstrip lines. S_{cxq} is designed through simulations to provide the required Q_e reduction from 14.74 to 8.6 as k_E is increased. The layouts used for Q_e extraction and reduction are presented in Figure 6.8(b). Designed Q_e and k_E variation with respect to SMP #2 position s_2 is shown in Figure 6.8(c). Simulated S-parameters of the filter is presented in Figure 6.9. It is observed that filter bandwidth

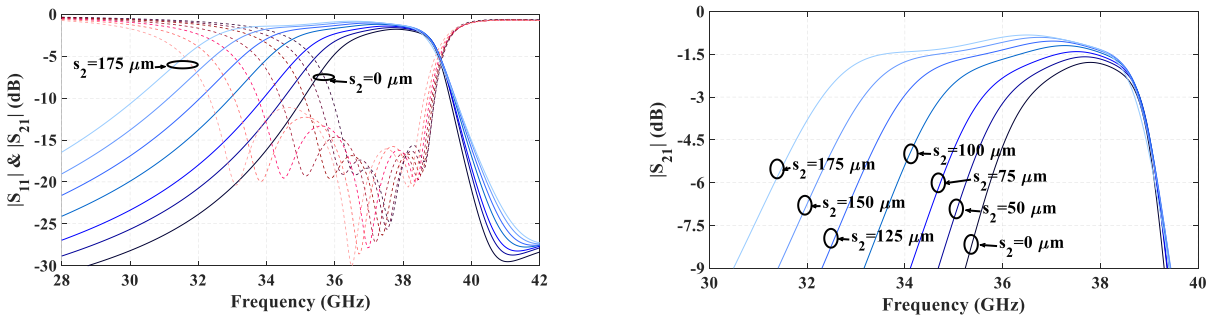

(a) (b)

Figure 6.9. Simulated performance of the BT-BPF. (a) $|S_{21}|$ and $|S_{11}|$; (b) close-up view of $|S_{21}|$ as a function of SMP #2 position s_2.

can be tuned from 7.6% up to 17.6%. The filter performs with mid-band 1.8 dB IL for the 7.6% FBW position and mid-band 0.95 dB IL for the 17.6% FBW position.

6.4. Frequency and Bandwidth Tunable Filter

The frequency and bandwidth tunable filter can be implemented as the combination of the frequency tunable constant FBW design presented in Section 6.2 and bandwidth tunable filter design presented in Section IV. Since the frequency and bandwidth tunable filter is loaded with both SMP #1 and SMP #2, two distinct microfluidic channels are needed. Consequently, the microfluidic channels need to be meandered as previously illustrated in Figure 6.2. The microfluidic channel dimensions used for prototype development are provided in the flowing section. The layout of the filter is presented in Figure 6.10(a) along with its dimensions. The

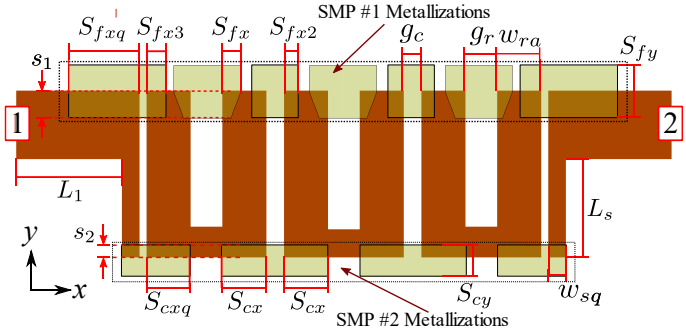

(a)

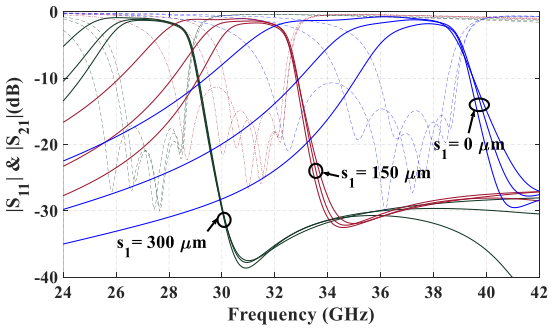

(b)

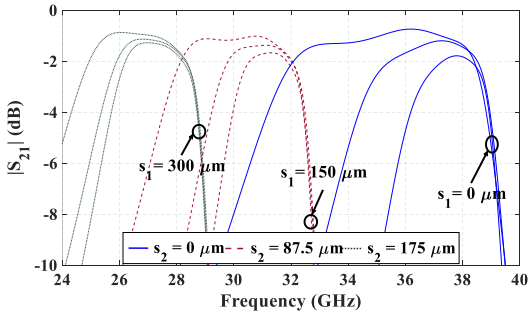

(b)

Figure 6.10. Simulated performance of the FBT-BPF and its simulated S-parameter performance. (a) Layout of the FBT-BPF; (b) Simulated $|S_{21}|$, $|S_{11}|$, and (c) close-up view of $|S_{21}|$ as a function of SMP #2 position s_2. ($L_1 = 0.6$, $w_1 = 0.39$, $L_r = 0.95$, $w_{ra} = 0.25$, $w_{rb} = 0.16$, $g_r = 0.18$, $g_c = 0.1$, $S_{fx} = 0.105$, $S_{fy} = 0.3$, $L_{fx} = 0.055$, $L_{fy} = 0.15$, $S_{cx} = 0.25$, $S_{cy} = 0.175$, $L_s = 0.56$, $w_{sq} = 0.1$, $g_{sq} = 0.04$, $S_{fxq} = 0.4$, $S_{fx2} = 0.08$, $S_{fx3} = 0.11$, $S_{cxq} = 0.25$, $0 \le s_1 \le S_{fy}$, $0 \le s_2 \le S_{cy}$; dimensions are in mm).

simulated S-parameter performance of the filter is shown in Figure 6.10(b) for sampled states The maximum bandwidth is 17.6% and 12.5% at the highest (i.e. $s_1 = 0$ mm) and lowest resonance frequencies (i.e. $s_1 = 0.3$ mm), respectively. The frequency of operation can be tuned from 38 GHz down to 28 GHz with near constant FBW of 7.68 ± 0.39% for $s_2 = 0$. The IL performance of the filter is presented in Figure 6.10(c). IL is less than 1.8 dB for all states. The worst-case IL is observed for the lowest FBW at highest operation frequency.

6.5. Fabrication

Filter prototypes are fabricated with the substrate stack-ups shown in Figure 6.1(a) and Figure 6.5. The resonators and SMPs are realized with standard photolithography. All dimensions of the resonators, microstrip lines, coupling stubs, and SMP metallizations are oversized by 10 μm in mask generation to account for wet etching related undercut. The substrate of the resonators is bonded with a double-side copper-cladded 0.762 mm thick FR4 substrate using silver epoxy and a bonding press in order to provide mechanical rigidity. This completes the PCB preparation for the resonators. The SMPs are cut with a dicing saw from their main substrate. The metallization surfaces of the SMPs are deposited with 5 μm thick Parylene N by using a PDS 2010 Parylene Deposition System. The microfluidic channel walls with 360±10 μm height are fabricated on top of the PCB. These walls are formed by spin-coating the PCB with SU8 photoresist ($\varepsilon_r = 3.25$, $\tan\delta = 0.017$) and applying standard photolithography for patterning. The processing of the walls is done in two-steps of spin-coating by following the procedures described in [104, 105] for optimal exposure and baking times. The holes needed for channel inlets and outlets are drilled along with the holes needed for mounting the edge connectors. The SMPs are placed within the microfluidic channel walls. Sealing the microfluidic channel with fused silica layer is carried out with the tenting technique [25]. Specifically, a ~50 μm thick film of soft-baked SU8 resist is placed

on top of the channel walls to form the tented structure. Fused silica slide is coated with ~50 μm layer of SU8 photoresist for adhesive bonding. PCB and the dry film are heated to 48 °C and brought in contact with the coated fused silica slide to complete the sealing. 48 °C is below the glass transition of SU-8. It ensures that the dry film does not melt and flow inside the channel [26]. Following this process, the PCB is exposed and hard baked to complete the microfluidic channel sealing process.

The microfluidic channel reservoirs that will be placed under the bottom side of the PCB are fabricated with PDMS using soft-photolithography processes [69]. The thickness of the PDMS used for the microfluidic reservoirs are 3 mm. A 1 mm diameter punch is used to realize the channel filling ports in the PDMS substrate that will enable fitting of flexible hoses for introducing the FC-40 liquid into the microfluidic channel. Bonding of the PDMS with the copper layer at the bottom surface of the PCB is carried out with O_2 plasma (50 W, 30 s) treatment of the PDMS and APTES treatment of the copper layer. The copper layer is submerged in a 5% APTES solution for 20 minutes at 70 °C and dried out with a nitrogen gun before brought in contact with the plasma treated PDMS to form the irreversible bond [106]. In order to place the piezoelectric actuators on top of the PDMS based microfluidic channel reservoirs, the reservoir areas are first bonded with 25 μm thick LCP (Rogers ULTRALAM® 3850 with 9 μm copper cladding on both sides) following the APTES process described above. The piezoelectric actuators are bonded to the LCP layers using silver epoxy (EPO-TEK® H20E). This completes the fabrication process. As a final step, the microfluidic channels are filled with the FC-40 dielectric liquid. For this, flexible hoses are fit into the channel reservoirs, and the FC-40 liquid is introduced into the microfluidic channel with syringes connected to one-way stopcock valves with Luer connections (Cole-Parmer). After filling the channels, the valves are closed and Luer sealing plugs are connected to finalize closing

the fluidic system. Prototypes maintain the valves and the plugs in case emptying/refilling of the microfluidic channels are needed. These components could be removed for stand-alone operation.

6.6. Experimental Verification

The prototypes for the bandwidth reconfigurable and frequency reconfigurable filters are shown in Figure 6.11. Filters that exhibit only the frequency or bandwidth tuning capabilities are fabricated with single microfluidic channel that contain either the SMP #1 or SMP #2. Figure 6.11(a) presents top and bottom views of the frequency tunable constant FBW filter. The SMP sizes and metallizations are shown in Figures 6.11 (d) and 6.11(e). The measured S-parameter

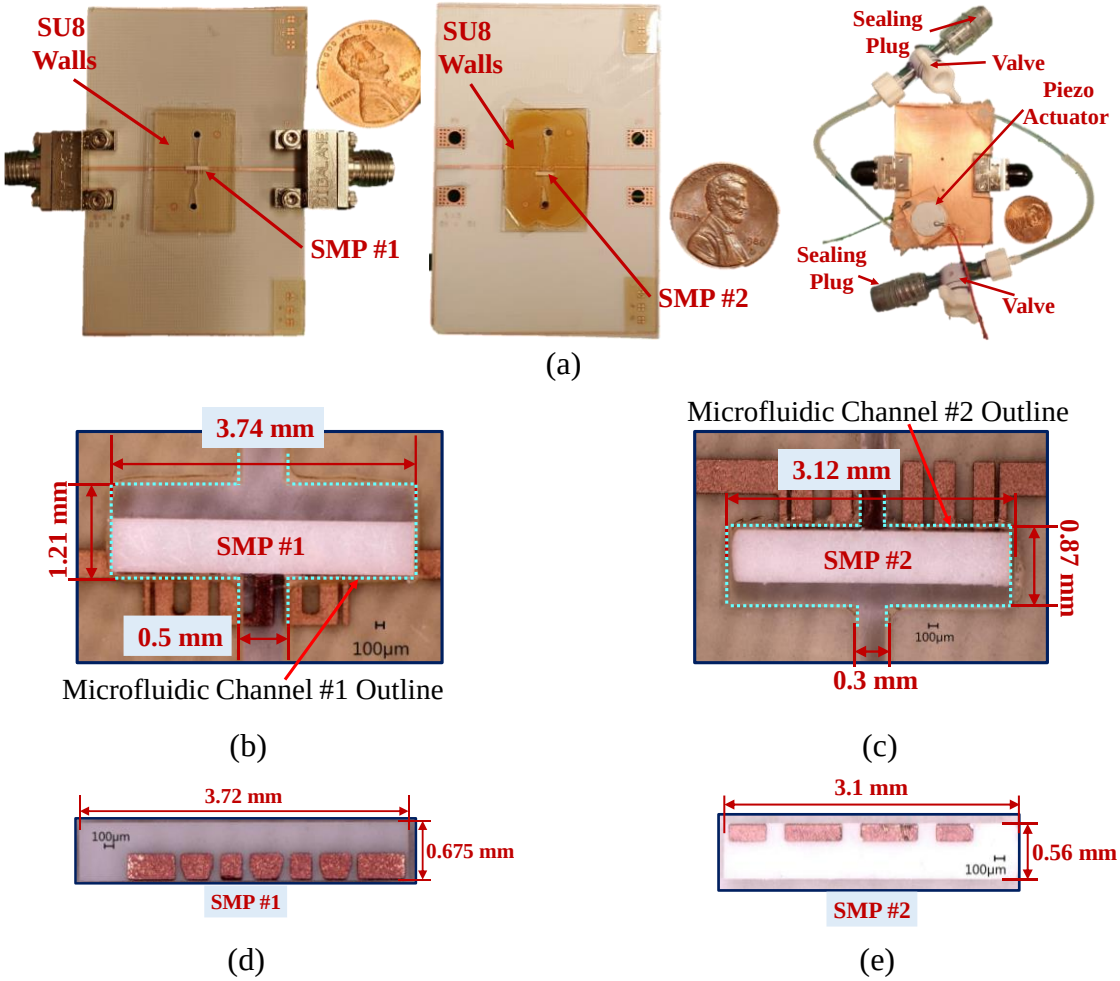

Figure 6.11. Detail of the FT-BPF and BT-BPF prototypes. (a) Top-side (left and center) and bottom-side views (right) of the FT-BPF/BT-BPF prototypes; (b) Microfluidic channel details of the FT-BPF; (c) Microfluidic channel details of BT-FPF; (d) SMP #1 of FT-BPF; (e) SMP #2 of BT-BPF.

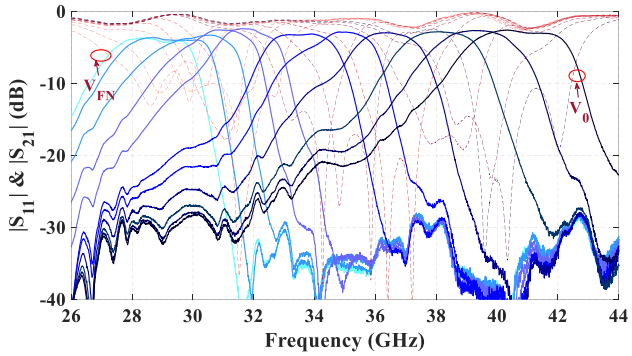

(a)

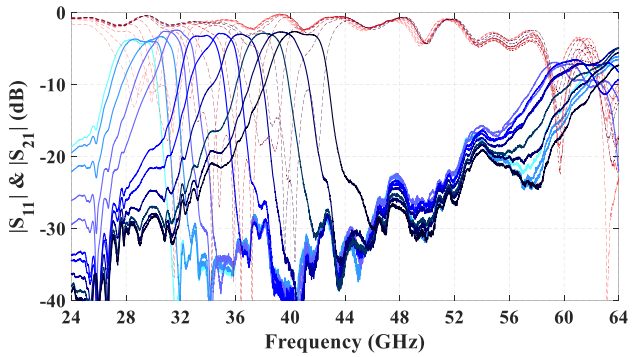

(b)

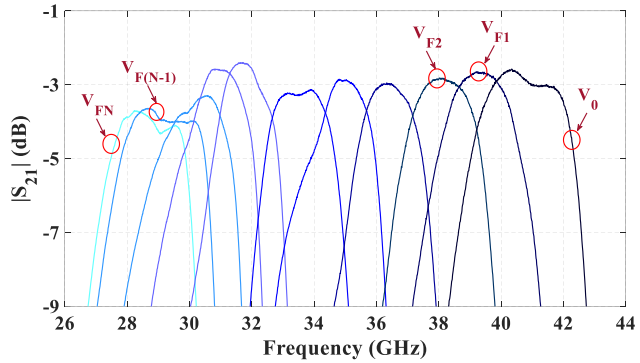

(c)

Figure 6.12. Measured performance of the FT-BPF prototype for actuation voltages V_{FN}. (a) 26 GHz – 44 GHz response; (b) 24 GHz – 64 GHz response; (c) Close-up S_{21} response (V_{F0} = 0, V_{F1} = 56, V_{F2} = 66, V_{F3} = 70, V_{F4} = 77, V_{F5} = 86, V_{F6} = 95, V_{F7} = 105, V_{F8} = 114, V_{F9} = 124, and V_{F10} = 129 V).

performance of the frequency tunable filter is shown in Figure 6.12(a). It is found that SMP #1 completes its motion range with piezoelectric actuation voltage varying from 0 V to 129 V. The center frequency of the prototype is shifted to 41 GHz for the unloaded case (i.e. $s_1 = 0$ mm). This ~8% resonance frequency shift is due to the substrate stack-up used in Keysight ADS (see Figure

6.5). The substrate stack-up maintains a uniform RO4003C substrate inside the microfluidic channel. However, the channel is partially filled with this substrate due to the physical size of the SMP. In the unloaded case, the SMP is completely removed, leaving the channel filled with the FC-40 dielectric liquid over the resonators. In addition, the channel walls partially overlap with resonators and this contributes to frequency and IL variation with respect to the simulations. Modeling non-uniform 2D substrate-stack-up and substrate stack-up variation as a function of SMP position requires employment of full-wave 3D EM simulators. However, due to the significant simulation times needed by 3D EM simulators, the presented filter design has been carried out with Keysight ADS Momentum suite under a fixed substrate stack-up configuration.

Simulating the unloaded filter layout in Keysight ADS with a 315 μm thick FC-40 liquid layer replacing the RO4003C layer shows a resonance frequency shift up to 42 GHz. Modeling the filter layout in 3D EM simulator Ansys HFSS shows the resonance frequency at 41 GHz. These simulations verify the reasoning behind the 8% resonance frequency shift observed in experiments. The filter is found to be tunable from 28 GHz to 41 GHz with SMP #1 position varied from s_1 = 0 mm to s_1 = 0.3 mm. The lower end of the frequency band is unchanged because the substrate-stack-up chosen in the Keysight ADS model is most accurate for the maximally loaded case of the resonators.

The measured IL of the filter is 3 dB and 4 dB at 38 GHz and 28 GHz, respectively. IL is better than 3 dB in majority of the frequency tuning range (i.e. 31 GHz – 41 GHz). The data represents ~1.2 dB increase in IL with respect to the simulations. This is mostly related to the half of the resonators being covered with lossy SU8 side walls. 3D EM simulator Ansys HFSS determines IL as 2.1 dB for the unloaded case and fits with measurements. Figure 6.12(b) presents the measured performance within 24 – 64 GHz band. Out of band rejection of the filter is better

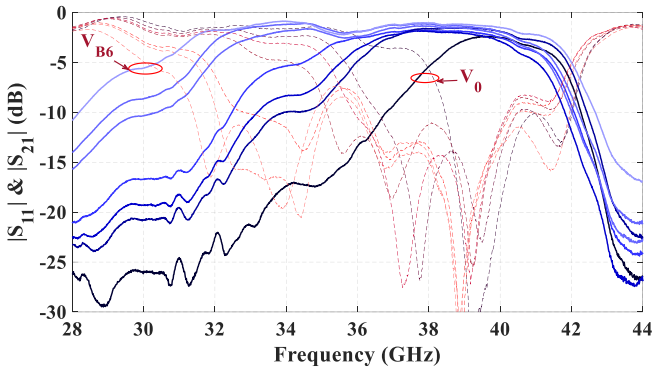

(a)

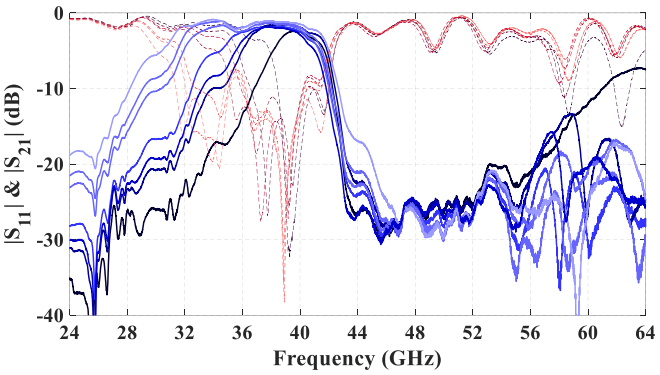

(b)

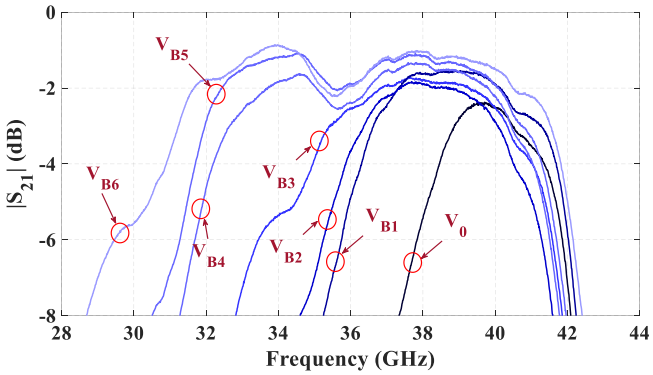

(c)

Figure 6.13. Measured performance of the BT-BPF prototype for actuation voltages V_{BN}. (a) 28 GHz – 44 GHz response; (b) 24 GHz – 64 GHz response; (c) Close-up S_{21} response (V_0 = 0, V_{B1} = 54, V_{B2} = 78, V_{B3} = 88, V_{B4} = 96 , V_{B5} = 104, V_{B6} = 115 V).

than 25 dB for majority of the states. Second harmonic of the resonators are contributing to the degradation in the out of band rejection. Improvement may be possible by carrying out the design on thinner substrates and considering alternative resonators arrangements/types. Figure 6.12(c) presents the close up view of the IL performance when SMP #1 is actuated with voltages ranging

from 0 V to 129 V. The filter maintains an almost constant 7.8% ± 0.75% FBW. This is in very good agreement with the simulated performance.

The measured S-parameter performance of the bandwidth tunable filter is shown in Figure 6.13(a) and (b). It is found that SMP #2 completes its motion range with piezoelectric actuation voltage varying from 0 V to 115 V. Figure 6.13(c) presents the close-up view of the IL performance for different bandwidth tuning actuation voltages. The SMP #2 can tune the filter bandwidth from 7.8% up to 16.7%. This is in good agreement with simulations. The filter performs with 2.6 dB IL at the lowest bandwidth and 1.9 dB IL at the highest bandwidth. The increase in IL and introduction

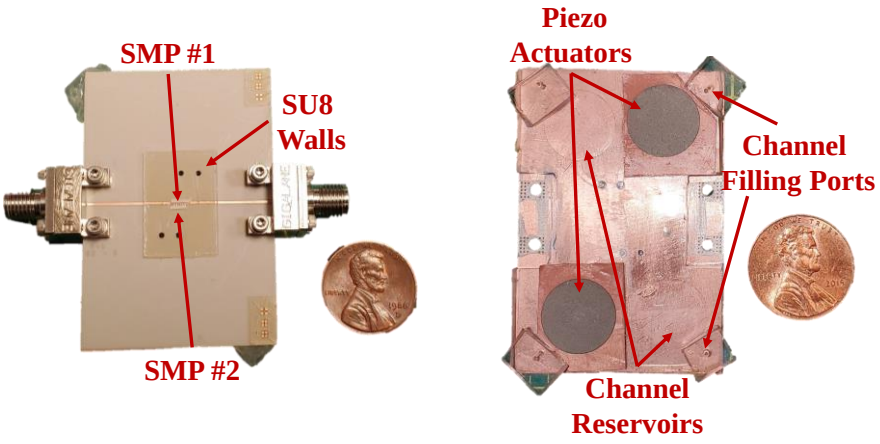

(a)

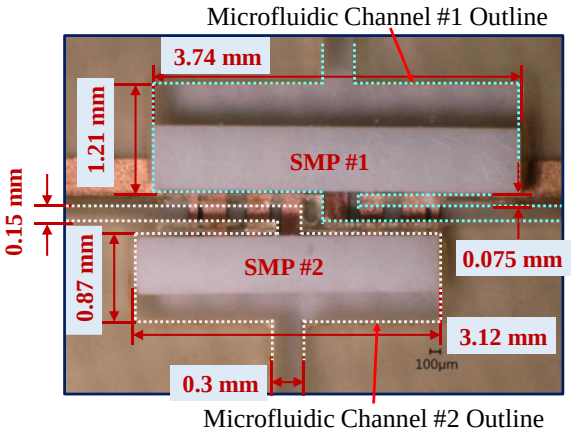

(b)

Figure 6.14. Detail of the FBT-BPF prototype. (a) Prototype and (b) microfluidic channel details.

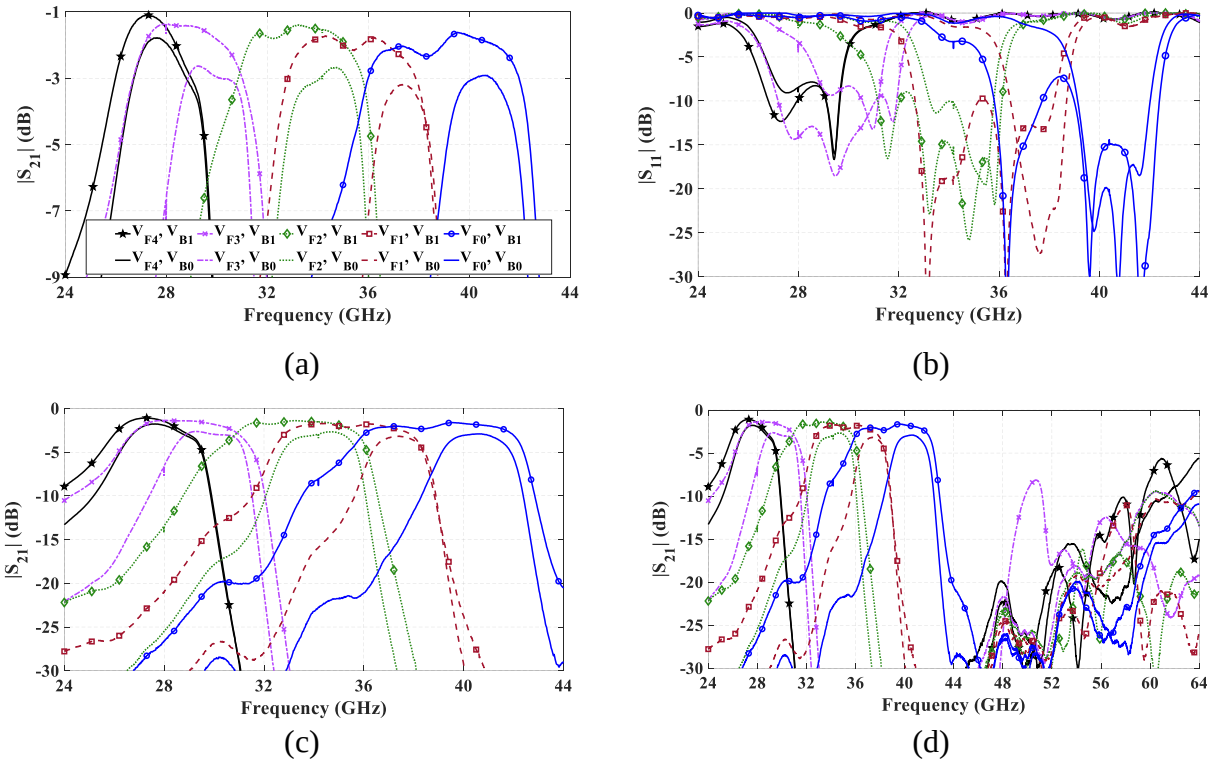

Figure 6.15. Measured performance of the FBT-BPF prototype for different actuation voltages V_{FN} and V_{BM}. (a) 24 GHz – 44 GHz S_{21} detailed response; (b) 24 GHz – 44 GHz S_{11} response; (c) 24 GHz – 44 GHz S_{21} response; (d) 24 GHz – 64 GHz S_{21} response ($V_{F0} = 0$ V, $V_{F1} = 64$ V, $V_{F2} = 87$ V, $V_{F3} = 125$ V, $V_{F4} = 142$ V, $V_{B0} = 0$ V, $V_{B1} = 127$ V).

of 1 dB ripple within the passband is associated with the differences in simulation-based substrate stack-up vs. the actual fabricated devices. These differences have been already explained for the frequency tunable filter.

The prototype of the frequency and bandwidth tunable filter is shown in Figure 6.14(a). A detailed view of the microfluidic channel dimensions is given in Figure 6.14(b). The measured S-parameter performance is shown in Figures 6.15 (a)-(d). The bandwidth can be reconfigured from 7.8% to 16.7% at 38 GHz. Worst-case IL is 3.1 dB at 38 GHz and 1.95 dB at 28 GHz. The measured IL performance matches much better with the Keysight ADS simulated IL performance due to the minimized SU8 channel walls on the filter resonators to host two distinct SMPs. SMP #1 and SMP

#2 complete their full motion ranges with piezoelectric actuation voltages varying within 0 V – 142 V and 0 V – 127 V, respectively. It is noticed that the actuation voltages are slightly increased in this filter with respect to the stand-alone frequency and stand-alone bandwidth tunable filters. This can be attributed to the shape of the microfluidic channels used within this design. Meandering the microfluidic channels within the available circuit area has a consequence of employing narrower channel widths. This necessitates a larger fluidic pressure for mobilizing the SMPs [107], resulting in higher actuation voltages.

6.7. Reliability and Power Handling Characterization

The prototypes are tested for their reconfiguration speed, reliability and power handling capability. In these tests, 1.85 mm end launch connectors were replaced with 2.92 mm end launch connectors. Therefore, this section shows the measured data up to 40 GHz. Reconfiguration speed is measured by using the set-up described in [93]. For this measurement, the frequency reconfigurable filter is used. The filter is excited with continuous single tone RF signal at 28 GHz. SMP is actuated with a 50% duty cycle rectangular waveform (0 V to 127 V) while tracking the output of a mm-wave power detector diode (Krytar 203AK) connected to the output of the filter. Figure 6.16 presents the detected voltage from the power detector. With the given setup, the signal received at the detector input was measured and set as -10 dBm at 28 GHz. This translates into ~46.4 mV received voltage at the detector output. At -25 dBm, the detected voltage measured is ~5 mV. With this information, reconfiguration speed can be estimated after the center frequency of the filter has shifted up enough to provide 15 dB attenuation at 28 GHz. This condition occurs after approximately 22.8 ms where the filter is estimated to have shifted ~6.5 GHz from its center frequency. Thus, reconfiguration speed for the filter is calculated as 285 MHz/ms. Additionally, the entire SMP actuation is expected to be within 35.8 ms.

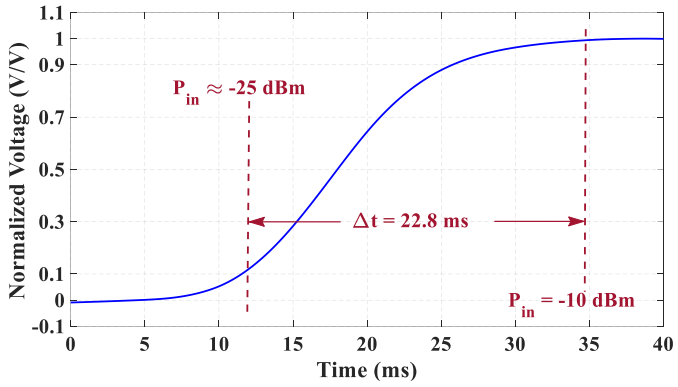

Figure 6.16. Measured reconfiguration time for the frequency reconfigurable filter.

For reliability testing, both stand-alone bandwidth tunable and stand-alone frequency tunable filters are actuated with a 20 Hz 50 % duty cycle rectangular waveform (0 V to 127 V) for 7 days. S-parameters of the filters are measured approximately after they are actuated 100×10^3, 1×10^6, 5×10^6 and 12×10^6 times. Figure 6.17 and Figure 6.18 show the measured performance for the stand-alone bandwidth tunable and stand-alone frequency tunable filter, respectively. For simplicity, the measured response is only shown at 3 possible actuation voltages (56 V, 86 V and 129 V and 54 V, 88 V and 115 V for the frequency reconfigurable and bandwidth reconfigurable filters respectively). It is observed that filters operate without major degradation in IL performance. For a given actuation voltage, center frequency shows variations less than 1%. This is likely due

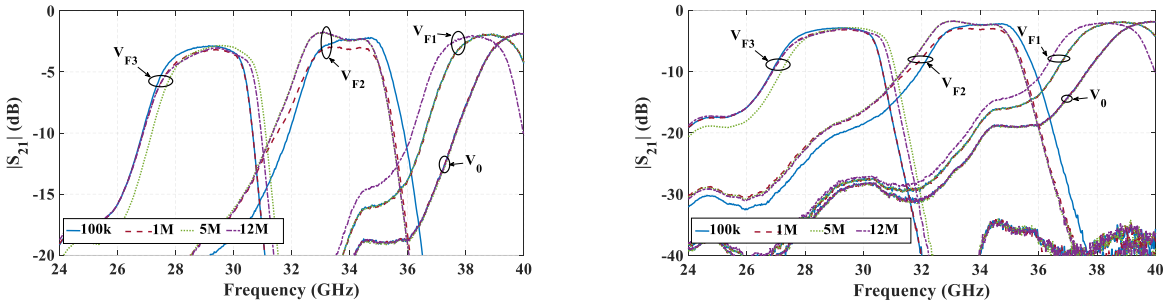

(a) (b)

Figure 6.17. FT-BPF prototype performance for different actuation cycles. Close-up detail (a) and expanded range view (b) of S_{21} performance after different actuation cycles ($V_0 = 0$ V, $V_{F1} = 56$ V, $V_{F2} = 86$ V, $V_{F3} = 129$ V).

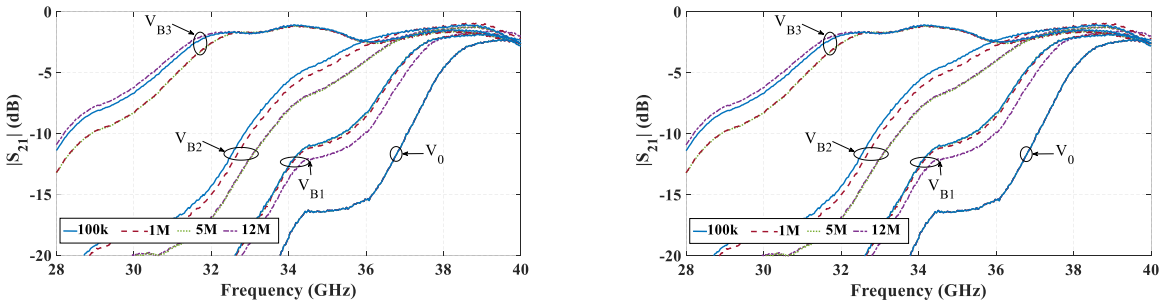

(a) (b)

Figure 6.18. BT-BPF prototype performance for different actuation cycles. Close-up detail (a) and expanded range view (b) of S_{21} performance after different actuation cycles ($V_0 = 0$ V, $V_{B1} = 54$ V, $V_{B2} = 88$ V, $V_{B3} = 115$ V).

to the mechanical nature of the reconfiguration scheme used. The repeatability test is stopped at ~12,000,000 cycles due to the frequency tunable filter developing a leak at the bonding interface between the fused silica and the SU8 channel walls. More investigations and repeatability testing are needed to fully understand if this is an isolated case associated with bonding parameters.

The filter prototype with simultaneous frequency and bandwidth tunability capability is used for power handling characterizations. This is motivated from the fact that this filter operates with the lowest measured IL. The experiment setup is similar to the one described in [94]. The filter is excited with continuous RF power at 38 GHz. The actuation condition selected for the power characterization is when the SMP #2 does not load the filter (i.e. smallest possible FBW). SMP #1 is actuated to shift center frequency of the filter to 38 GHz. These actuation voltage settings make the dual-tunable filter operate at its highest IL state to maximize the RF power dissipation. The filter is excited with RF power varying from 0.5 W to 2 W. Temperature measurements are taken after a steady-state condition is achieved for the given input power by using a thermal camera. Multiphysics simulations are performed with Ansys 19.2 Workbench to verify the experiments. Measured temperatures at filter surface and simulated temperatures agree quite well as shown in Figure 6.19. Simulations indicate that at 5 W of input RF power, the internal

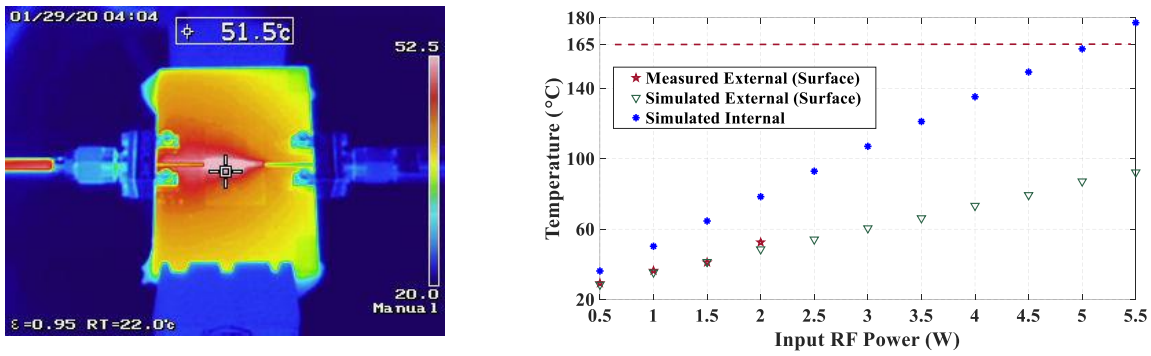

(a) (b)

Figure 6.19. Power handling performance characterization of the FBT-BPF prototype. Infrared image captured after steady-state temperatures with 2W input RF power (a); and measured temperatures at different input RF powers (b).

temperature of the device rises to 162 °C. This is slightly below the boiling temperature of FC-40 (i.e. 165 °C). Therefore, 5 W can be considered as the maximum continuous RF power handling level of this filter. Power handling can further be enhanced by resorting to thicker ground planes and/or heat sinks. Table 6.1 presents a performance comparison of several state-of-the-art reconfigurable filters. IL performance of the microfluidic reconfiguration approach benefits from the lack of active components. Typical IL performance for implementations of reconfigurable filters with varactor/PIN diodes is in the order of >7 dB, which can be expected to further increase in the 38 GHz band. Similarly, power handling capabilities are expected to be higher for the microfluidic technology than for varactors.

6.8. Chapter Summary

The implementation of a microfluidically reconfigurable 3-pole coupled combline filter at mm-wave frequencies with integrated actuation is demonstrated for the first time. Three filters are designed, fabricated and characterized to demonstrate the capabilities of microfluidic actuation at observed mm-wave frequencies. Specifically, a constant FBW frequency tunable filter, a bandwidth tunable filter, and a frequency and bandwidth reconfigurable filter are demonstrated. It was shown that the frequency and bandwidth tunable filter performs with worst-case 3.1 dB IL,

Table 6.1. Performance comparison with state-of-the-art filters.

Reference	Technology	Frequency Range (GHz)	IL (dB)	Tuning Type	FBW (%)		Tuning Ratio	Continuous Power (W)	Reconfig. Speed
					Constant	Tunable			
[108]	Microstrip (Varactor)	0.7–1.1	7–1.5	Continuous (Freq. Only)	-	7–27	1.6:1	0.32	-
[109]	Microstrip (PIN Diode)	20.5–21.3	9–8	Discrete (Freq. Only)	4.2±0.6	No	1.04:1	-	-
[110]	MEMS	18.6–21.4	4.2–3.9	Discrete (Freq. Only)	7.5±0.1	No	1.15:1	-	-
[111]	EVA (MEMS)	20–40	2.9	Continuous (Freq. Only)	3.3±1.4	No	2:1	-	10–60 μs*
[112]	SIW	20–26.5	3.2–3.4	Continuous (Freq. Only)	3±0.2	No	1.33:1	-	-
[113]	BST	28–34	3.8–2.8	Continuous (Freq. Only)	12.1±1.1	No	1.21:1	-	-
[114]	Microfluidics (CPW)	3.4–5.5	2.35–4.8	Discrete (Freq. Only)	5±0.35	No	1.6:1	10	-
[63]	Microfluidics (Microstrip)	3.75–4.75	0.6	Discrete (Freq. Only)	39±2.5	No	1.19:1	-	70±20 ms
[27]	Microfluidics (Microstrip)	1.5–4.0	2.5–4	Continuous (Freq. Only)	5	No	2.7:1	15	2.5 MHz/ms
This Work	Microfluidics (Microstrip)	28–41	1.9–3.1	Continuous (Freq. and FBW)	7.8±0.75	7.8–16.7	1.46:1	5	285 MHz/ms

while exhibiting a constant 7.8% ± 0.75% FBW and bandwidth tunability within 7.8% to 16.7%. A 3-pole is selected for simplicity, however, the concepts demonstrated in this Chapter can be applied in a straight-forward manner for higher order filters. One only would need to compensate additional coupling factors with different capacitive values (i.e. this translates in different overlap areas in the SMP). Furthermore, the integrated actuation mechanism allows for extended testing of filter reconfiguration. Repeatability tests demonstrate that the filter performs with no major degradation in IL performance and can be reconfigured at 285 MHz/ms, implying about 35.8 ms reconfiguration for the whole frequency range of 28 GHz – 41 GHz. Power handling characterization shows that the filter could handle up to 5 W of continuous RF power without the need of a thick ground plane or external cooling. Further investigations could lead to optimization of reconfiguration speeds by employing different channel shapes or plate sizes.

Chapter 7: Final Remarks and Overview of Future Work

Several applications of microfluidic technology for millimeter-wave device reconfiguration have been introduced, designed and their operation is successfully demonstrated with experimental verifications. Specifically, microfluidically switched microstrip lines utilizing selectively metallized plates were introduced to demonstrate low-loss and wideband reconfiguration at mm-wave frequencies. The novel microfluidic switch exhibits less than 0.2 dB IL over 20 GHz bandwidth. Additionally, an equivalent circuit model is developed to allow for designing complex networks with several microfluidic switches.

The circuit model is utilized for designing a low-loss and wideband microfluidically switched feed network for mm-wave beam-steering applications. For this purpose, the equivalent circuit model and layout of the microfluidically switched microstrip line is cascaded in an SP2T configuration. When compared to microfluidic beam-steering focal plane array designs previously demonstrated; the switching time, bandwidth, and loss performances are significantly improved. This is made possible by replacing the need for resonant microstrip lines with the microfluidic switches. An 8-element 1-D beam-steering array is successfully demonstrated at 30 GHz. The feed network bandwidth is demonstrated to be 38% and low IL performance of <3 dB. Additionally, the feed network design can be expanded to up to 64 elements with no degradation in bandwidth performance. Utilizing this compact feed network design, the microfluidically switched beam-steering focal plane array concept can be extended for 2D beam-steering. Something that was not possible with the previous work. More specifically, a 64 element (8×8) MFPA configuration

proves to offer simulated worst-case feed network losses < 5.2 dB. With the improvements demonstrated in this work, reconfiguring the MFPA in about 40 ms is now possible, as compared to over 5 s in previous designs. This compact reconfiguration allows for integrated actuation mechanisms that pave the way for enabling reliability testing and replace the bulky micropumps that were previously utilized for providing fluidic actuation.

With the promising advantages of microfluidically switched microstrip line concept, a low-loss and wideband microfluidic switch actuated with an integrated and compact piezoelectric mechanism is presented. This is possible by extending the initial concept of microfluidically switched lines from Chapter 3 and miniaturizing the switch area by about 73%. The miniaturized SPST switch prototype exhibits 0.42 dB IL with an operating bandwidth from 22 to 40 GHz. A piezoelectric actuation mechanism is successfully integrated for the first time in an SMP-based microfluidic device. The SPST switch is characterized to perform with 1.12 ms reconfiguration time, the prototype is operated up to ~3×10^6 switching cycles with no apparent performance degradation, and power handling measurements show the potential to provide >43 dBm at mm-wave frequencies. The SPST design is demonstrated to be scalable for multi-throw operations with an SP4T design that maintains similar IL and wideband performance. Additionally, the SP4T switch is used to develop a 4-element mm-wave beam-steering antenna array demonstrating the advanced capabilities of integrating the microfluidic actuation mechanism in compact device.

Continuing from the successful implementation of piezoelectric actuation within microfluidically reconfigurable devices in Chapter 5, the implementation of a microfluidically reconfigurable 3-pole coupled combline filter at mm-wave frequencies with integrated actuation is demonstrated for the first time. Three tunable filters are designed, fabricated and characterized to demonstrate the capabilities of microfluidic actuation at mm-waves. Specifically, a constant

FBW frequency tunable filter, a bandwidth tunable filter, and a frequency and bandwidth reconfigurable filter are implemented. The frequency and bandwidth tunable filter perform with worst-case 3.1 dB IL, while exhibiting a constant 7.8% ± 0.75% FBW and bandwidth tunability within 7.8% to 16.7%. Moreover, the concepts demonstrated in Chapter 6 can be applied in a straight-forward manner for higher order filters. One only would need to compensate additional coupling factors with different capacitive values (i.e. this translates in different overlap areas in the SMP). Furthermore, the integrated actuation mechanism allows for extended testing of filter reconfiguration. Repeatability tests proved filter performance over 12 million cycles with no major degradation in IL, and the capability to be reconfigured at 285 MHz/ms. Additionally, power handling characterization indicates potentially up to 5 W of continuous RF power without the need of a thick ground plane or any external cooling mechanisms.

7.1. Future Work

Considerable advances in microfluidic reconfiguration of RF devices with the selectively metallized plate approach have been introduced for the first time in this dissertation. Nevertheless, there is still plenty of work that can be done to further improve the performance of these devices and to fully understand their electromagnetic behavior.

Specifically, several considerations can be taken for potentially improving the SMP speed and reducing the actuation voltages needed for transforming the piezoelectric displacement into fluidic pressure. Namely, investigating the impact of: (i) further reducing device size and SMP motion by depositing/utilizing thinner metal layers (e.g. <10 μm –since this work employed metal layers of 17.5 μm); (ii) utilizing different plates with varying sizes and materials that provide densities closer to the density of the liquid that fills the channels; and (iii) evaluating the impact of different microfluidic channel shapes that potentially can help distribute channel flow evenly

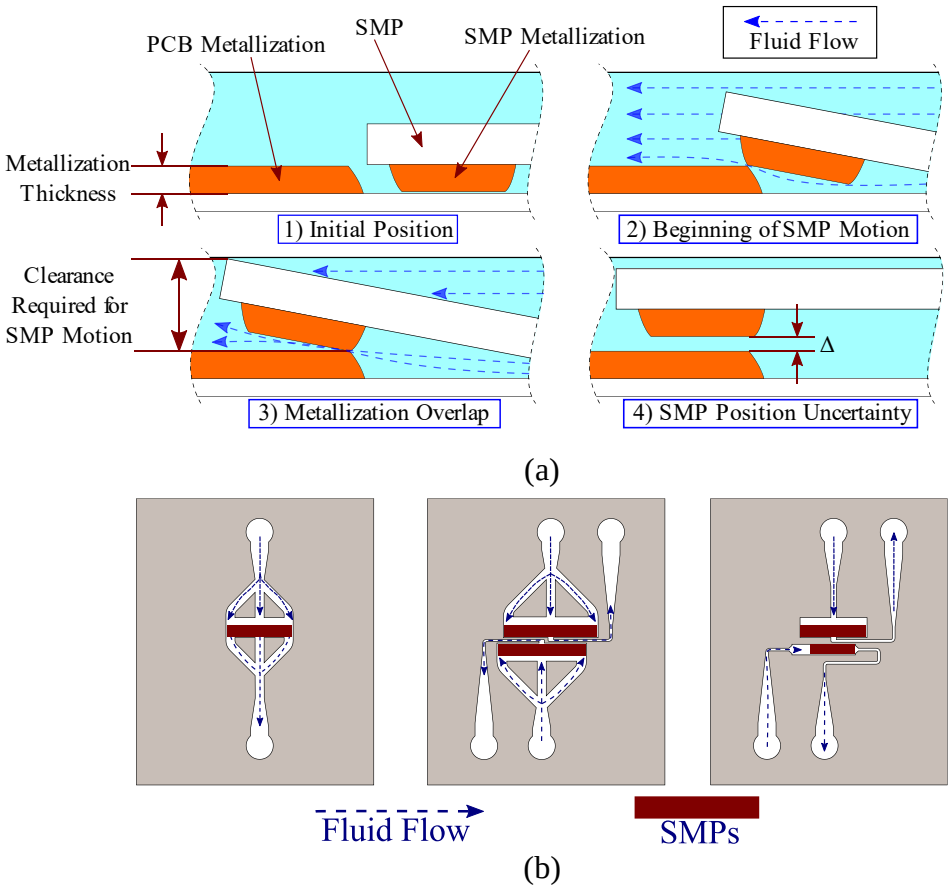

Figure 7.1. Microfluidic channel limitations and proposed shapes for potential improvements. (a) Detail of estimated SMP motion mechanism within the microfluidic channel. (b) Proposed microfluidic channel shapes to be investigated to potentially improve SMP motion and piezoelectric actuation.

across the SMP. Figure 7.1(a) demonstrates the limitations for microfluidic channel height fabrication when considering PCB and SMP metallization thicknesses, assuming that the SMP is resting on top of the PCB before starting motion. Figure 7.1(b) presents possible channel shapes that can be investigated to improve the performance of the filter introduced in Chapter 6. Obtaining further knowledge in these areas will aid in optimizing the performance of microfluidically reconfigurable devices and provide an in-depth understanding of the physical machinations at work within the fluidic actuation of these devices. Furthermore, clear design criteria for choosing the right piezoelectric actuator size and microfluidic channels can be developed.

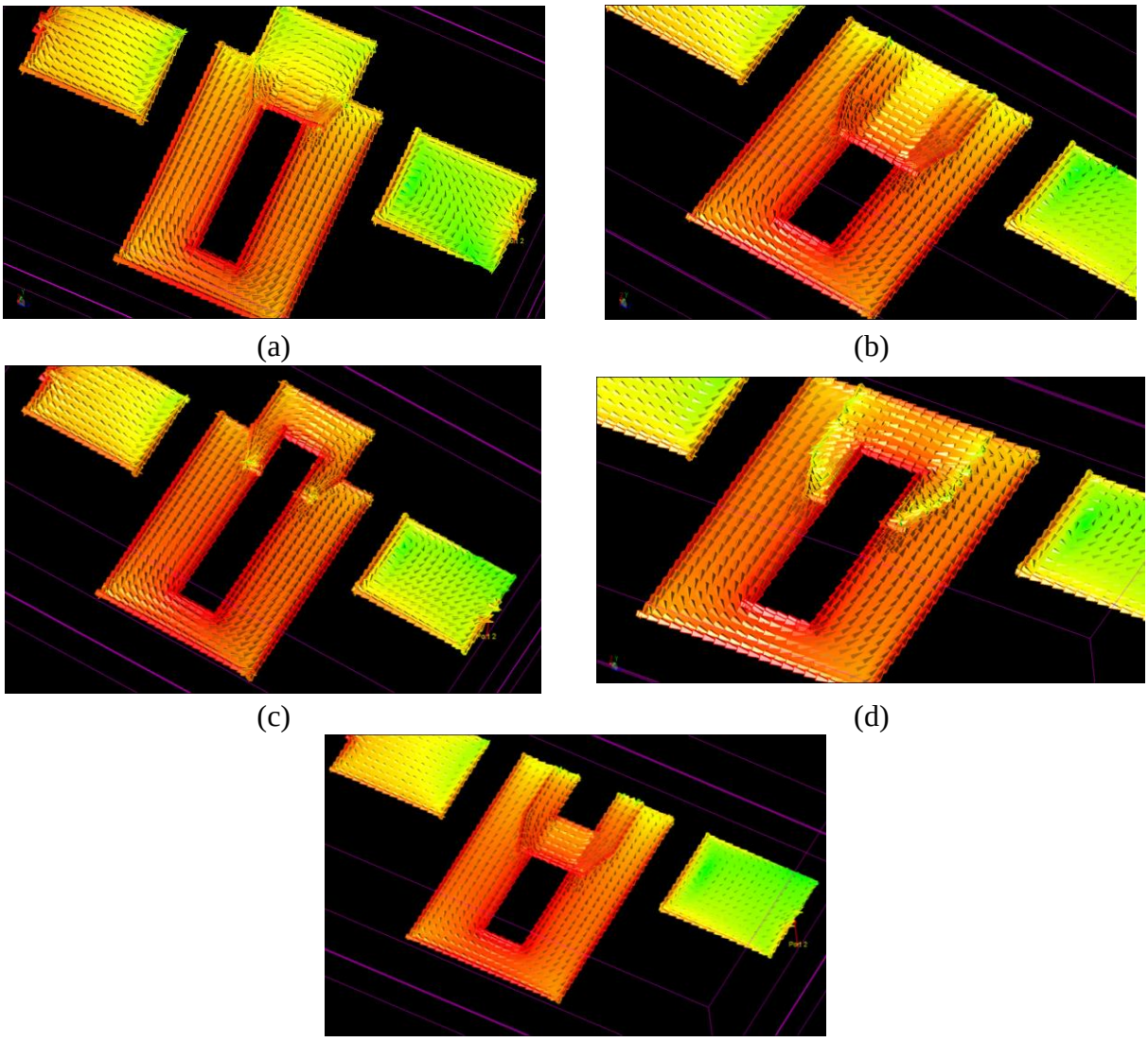

(a) (b) (c) (d) (e)

Figure 7.2. Different current distributions within the SMP #1 overlap trace at the resonator of the BPF presented in Chapter 6 for different overlap positions and metallization shape.

Another area of further research is the accurate modeling of the electromagnetic phenomena occurring at the SMP overlaps. For this work, a parallel plate capacitance condition was assumed at the overlaps between the SMP and the microwave circuit metal traces. However, this approximation is not completely accurate as demonstrated by the need for optimization/tuning of certain final dimensions within the presented designs. It is suspected that additional parasitic behaviors that are not accurately modeled by the parallel plate capacitance approximation are

present and actively affecting the SMP coupling with the microwave circuit. Figure 7.2 offers the current distribution extracted for the SMP #1 overlap of the tunable filter of Chapter 6. Specifically, for the metallization area that has as a main purpose to reconfigure the resonator center frequency. Additionally, the metallization area is moved or meandered/modified to explore the changes in current distribution. As it is seen in Figure 7.2, the changes observed in the current imply a complex parasitic behavior that if completely understood will offer more accurate modeling and simplified design of these type of devices. Furthermore, this behavior can be present in the form of enhancements or degradations in various cases. Therefore, if one can understand the phenomena, SMP shape can become an additional tool to improve device performance.

References

[1] M. Sayginer and G. M. Rebeiz, "An Eight-Element 2-16-GHz Programmable Phased Array Receiver With One, Two, or Four Simultaneous Beams in SiGe BiCMOS," *IEEE Transactions on Microwave Theory and Techniques,* vol. 64, no. 12, pp. 4585-4597, Dec 2016, doi: 10.1109/Tmtt.2016.2620144.

[2] W. Shin, B. H. Ku, O. Inac, Y. C. Ou, and G. M. Rebeiz, "A 108-114 GHz 4 x 4 Wafer-Scale Phased Array Transmitter With High-Efficiency On-Chip Antennas," *IEEE Journal of Solid-State Circuits,* vol. 48, no. 9, pp. 2041-2055, Sep 2013, doi: 10.1109/Jssc.2013.2260097.

[3] Y. Yang, O. Gurbuz, and G. M. Rebeiz, "An 8-Element 400 GHz Phased-Array in 45 nm CMOS SOI," *2015 IEEE Mtt-S International Microwave Symposium (Ims),* 2015.

[4] G. M. Rebeiz and K. J. Koh, "Silicon RFICs for Phased Arrays," *IEEE Microwave Magazine,* vol. 10, no. 3, pp. 96-103, May 2009, doi: 10.1109/Mmm.2009.932078.

[5] G. M. Rebeiz *et al.*, "Tuning in to RF MEMS," *IEEE Microwave Magazine,* vol. 10, no. 6, pp. 55-72, Oct 2009, doi: 10.1109/Mmm.2009.933592.

[6] G. M. Rebeiz, C. D. Patel, S. K. Han, C. Ko, and K. M. J. Ho, "The Search for a Reliable MEMS Switch," *IEEE Microwave Magazine,* vol. 14, no. 1, pp. 57-67, 2013, doi: 10.1109/MMM.2012.2226540.

[7] L. M. K. Timothy, M. L. Ownby, and D. G. Bowen, "Method and apparatus for an improved antenna tracking system mounted on an unstable platform," ed: Google Patents, 2002.

[8] N. Verkerk, "Gimbal system for satellite antenna," ed: Google Patents, 2003.

[9] A. P. Saghati and K. Entesari, "A Tunable Quarter-Mode Substrate Integrated Waveguide Antenna," *2016 IEEE Antennas and Propagation Society International Symposium,* pp. 841-842, 2016.

[10] F. Alibaz-Oner, M. Can, B. Ilhan, O. Polat, G. Mumcu, and H. Direskeneli, "Presence of Fibromyalgia in Patients with Takayasu's Arteritis," *Internal Medicine,* vol. 52, no. 24, pp. 2739-2742, 2013, doi: 10.2169/internalmedicine.52.0848.

[11] O. L. Chlieh, W. T. Khan, and J. Papapolymerou, "L-band tunable microstrip bandpass filter on multilayer organic substrate with integrated microfluidic channel," in *2014 IEEE MTT-S International Microwave Symposium (IMS2014)*, 1-6 June 2014 2014, pp. 1-4, doi: 10.1109/MWSYM.2014.6848341.

[12] W. Zhou, H. Tang, and J. Chen, "Novel Microfluidically Tunable Differential Dual-Mode Patch Filter," *IEEE Microwave and Wireless Components Letters,* vol. 27, no. 5, pp. 461-463, 2017, doi: 10.1109/LMWC.2017.2690874.

[13] S. J. Mazlouman, X. J. Jiang, A. N. Mahanfar, C. Menon, and R. G. Vaughan, "A Reconfigurable Patch Antenna Using Liquid Metal Embedded in a Silicone Substrate," *IEEE Transactions on Antennas and Propagation,* vol. 59, no. 12, pp. 4406-4412, 2011, doi: 10.1109/TAP.2011.2165501.

[14] A. Dey, A. Kiourti, G. Mumcu, and J. L. Volakis, "Microfluidically Reconfigured Frequency Tunable Dipole Antenna," *2015 9th European Conference on Antennas and Propagation (EuCAP),* 2015.

[15] A. M. Morishita, C. K. Y. Kitamura, A. T. Ohta, and W. A. Shiroma, "Two-octave tunable liquid-metal monopole antenna," *Electronics Letters,* vol. 50, no. 1, pp. 19-20, 2014, doi: 10.1049/el.2013.2971.

[16] A. Gheethan, R. Guldiken, and G. Mumcu, "Microfluidic Enabled Beam Scanning Focal Plane Arrays," *2013 IEEE Antennas and Propagation Society International Symposium (APS/URSI),* pp. 208-+, 2013.

[17] C. H. Chen and D. Peroulis, "Liquid RF MEMS wideband reflective and absorptive switches," *IEEE Transactions on Microwave Theory and Techniques,* vol. 55, no. 12, pp. 2919-2929, Dec 2007, doi: 10.1109/Tmtt.2007.910011.

[18] C. H. Chen, J. Whalen, and D. Peroulis, "Non-toxic liquid-metal 2-100 GHz MEMS switch," *2007 Ieee/Mtt-S International Microwave Symposium Digest, Vols 1-6,* pp. 363-366, 2007, doi: Doi 10.1109/Mwsym.2007.380446.

[19] P. Sen and C. J. Kim, "A Liquid-Metal RF Mems Switch with Dc-to-40 Ghz Performance," *IEEE 22nd International Conference on Micro Electro Mechanical Systems (MEMS 2009),* pp. 904-907, 2009, doi: Doi 10.1109/Memsys.2009.4805530.

[20] N. Vahabisani, S. Khan, and M. Daneshmand, "Microfluidically Reconfigurable Rectangular Waveguide Filter Using Liquid Metal Posts," *IEEE Microwave and Wireless Components Letters,* vol. 26, no. 10, pp. 801-803, Oct 2016, doi: 10.1109/Lmwc.2016.2605450.

[21] K. Entesari and A. P. Saghati, "Fluidics in Microwave Components," *IEEE Microwave Magazine,* vol. 17, no. 6, pp. 50-75, Jun 2016, doi: 10.1109/Mmm.2016.2538513.

[22] M. S. Anwar and A. Bangert, "3D printed microfluidics-based reconfigurable antenna," in *2017 IEEE MTT-S International Microwave Workshop Series on Advanced Materials and Processes for RF and THz Applications (IMWS-AMP)*, 20-22 Sept. 2017 2017, pp. 1-3, doi: 10.1109/IMWS-AMP.2017.8247364.

[23] N. Vahabisani, S. Khan, and M. Daneshmand, "A K-Band Reflective Waveguide Switch Using Liquid Metal," *IEEE Antennas and Wireless Propagation Letters,* vol. 16, pp. 1788-1791, 2017, doi: 10.1109/LAWP.2017.2679072.

[24] T. Palomo and G. Mumcu, "Highly Reconfigurable Bandpass Filters Using Microfluidically Controlled Metallized Glass Plates," *2014 IEEE MTT-S International Microwave Symposium (IMS),* 2014.

[25] T. Palomo and G. Mumcu, "Microfluidically Reconfigurable Metallized Plate Loaded Frequency-Agile RF Bandpass Filters," *IEEE Transactions on Microwave Theory and Techniques,* vol. 64, no. 1, pp. 158-165, 2016, doi: 10.1109/TMTT.2015.2504473.

[26] A. Dey and G. Mumcu, "Microfluidically Controlled Frequency-Tunable Monopole Antenna for High-Power Applications," *IEEE Antennas and Wireless Propagation Letters,* vol. 15, pp. 226-229, 2016, doi: 10.1109/Lawp.2015.2438863.

[27] T. Palomo and G. Mumcu, "Microfluidically Reconfigurable Microstrip Line Combline Filters With Wide Frequency Tuning Capabilities," *IEEE Transactions on Microwave Theory and Techniques,* http://doi.org/10.1109/TMTT.2017.2730181 vol. 65, no. 10, pp. 3561-3568, 2017.

[28] E. Lourandakis, R. Weigel, H. Mextorf, and R. Knoechel, "Circuit Agility," *IEEE Microwave Magazine,* vol. 13, no. 1, pp. 111-121, 2012, doi: 10.1109/MMM.2011.2173987.

[29] N. J. Kolias, "Recent advances in Ga N MMIC technology," in *Proc. IEEE Custom Integrated Circuits Conf. (CICC)*, 2015/september, pp. 1-5.

[30] G. M. Rebeiz, "RF MEMS for wireless-bands tunable networks," in *Proc. Digest of Papers. 2006 Topical Meeting Silicon Monolithic Integrated Circuits in RF Systems*, 2006/january, pp. 1-1 pp.

[31] R. L. Schmid, P. Song, and J. D. Cressler, "A compact, transformer-based 60 GHz SPDT RF switch utilizing diode-connected SiGe HBTs," in *Proc. IEEE Bipolar/BiCMOS Circuits and Technology Meeting (BCTM)*, 2013/september, pp. 111-114.

[32] R. S. Howell *et al.*, "The Super-Lattice Castellated Field Effect Transistor (SLCFET): A novel high performance Transistor topology ideal for RF switching," in *Proc. IEEE Int. Electron Devices Meeting*, 2014/december, pp. 11.5.1-11.5.4.

[33] F. Thome, M. Ohlrogge, A. Leuther, M. Schlechtweg, and O. Ambacher, "An investigation of millimeter wave switches based on shunt transistors including SPDT SWITCH MMICs up to 300 GHz," in *Proc. IEEE MTT-S Int. Microwave Symp. (IMS)*, 2016/05, pp. 1-4.

[34] M. K. Cho, I. Song, J. G. Kim, and J. D. Cressler, "An Active Bi-Directional SiGe DPDT Switch With Multi-Octave Bandwidth," *IEEE Microwave and Wireless Components Letters,* http://doi.org/10.1109/LMWC.2016.2537055 vol. 26, no. 4, pp. 279-281, 2016.

[35] G. M. Rebeiz, "Millimeter-wave SiGe RFICs for large-scale phased-arrays," in *Proc. IEEE Bipolar/BiCMOS Circuits and Technology Meeting (BCTM)*, 2014/september, pp. 56-59.

[36] A. Valdes-Garcia *et al.*, "A Fully Integrated 16-Element Phased-Array Transmitter in SiGe BiCMOS for 60-GHz Communications," *IEEE Journal of Solid-State Circuits,* http://doi.org/10.1109/JSSC.2010.2074951 vol. 45, no. 12, pp. 2757-2773, 2010.

[37] D. Rodrigo, L. Jofre, and J. Perruisseau-Carrier, "Unit Cell for Frequency-Tunable Beamscanning Reflectarrays," *IEEE Transactions on Antennas and Propagation,* http://doi.org/10.1109/TAP.2013.2281375 vol. 61, no. 12, pp. 5992-5999, 2013.

[38] G. Rebeiz, "Large-scale millimeter-wave phased arrays for 5G systems," in *Proc. IEEE 16th Topical Meeting Silicon Monolithic Integrated Circuits in RF Systems (SiRF)*, 2016/january, pp. 4-4.

[39] G. M. Rebeiz and J. B. Muldavin, "RF MEMS switches and switch circuits," *IEEE Microwave Magazine,* http://doi.org/10.1109/6668.969936 vol. 2, no. 4, pp. 59-71, 2001.

[40] P. D. Grant, M. W. Denhoff, and R. R. Mansour, "A Comparison between RF MEMS Switches and Semiconductor Switches," in *Proc. Int. Conf. MEMS, NANO and Smart Systems ICMENS 2004*, 2004/august, pp. 515-521.

[41] E. Brookner, "Recent developments and future trends in phased arrays," in *Proc. IEEE Int Phased Array Systems Technology Symp*, 2013/october, pp. 43-53.

[42] R. R. Mansour, "RF MEMS-CMOS Device Integration: An Overview of the Potential for RF Researchers," *IEEE Microwave Magazine,* http://doi.org/10.1109/MMM.2012.2226539 vol. 14, no. 1, pp. 39-56, 2013.
[43] G. M. Rebeiz, C. D. Patel, S. K. Han, C. H. Ko, and K. M. J. Ho, "The Search for a Reliable MEMS Switch," *IEEE Microwave Magazine,* http://doi.org/10.1109/MMM.2012.2226540 vol. 14, no. 1, pp. 57-67, 2013.
[44] W. H. Weedon, W. J. Payne, and G. M. Rebeiz, "MEMS-switched reconfigurable antennas," in *Proc. IEEE Antennas and Propagation Society Int. Symp*, 2001/july, vol. 3, pp. 654--657 vol.3-657 vol.3.
[45] H. Zareie and G. M. Rebeiz, "High-Power RF MEMS Switched Capacitors Using a Thick Metal Process," *IEEE Transactions on Microwave Theory and Techniques,* http://doi.org/10.1109/TMTT.2012.2226744 vol. 61, no. 1, pp. 455-463, 2013.
[46] Y. Q. Zhu, L. Han, L. F. Wang, J. Y. Tang, and Q. A. Huang, "A Novel Three-State RF MEMS Switch for Ultrabroadband (DC-40 GHz) Applications," *IEEE Electron Device Letters,* http://doi.org/10.1109/LED.2013.2269993 vol. 34, no. 8, pp. 1062-1064, 2013.
[47] N. Kingsley, D. E. Anagnostou, M. Tentzeris, and J. Papapolymerou, "RF MEMS Sequentially Reconfigurable Sierpinski Antenna on a Flexible Organic Substrate With Novel DC-Biasing Technique," *Journal of Microelectromechanical Systems,* http://doi.org/10.1109/JMEMS.2007.902462 vol. 16, no. 5, pp. 1185-1192, 2007.
[48] K. V. Caekenberghe, "RF MEMS on the radar," *IEEE Microwave Magazine,* http://doi.org/10.1109/MMM.2009.933596 vol. 10, no. 6, pp. 99-116, 2009.
[49] B. Schoenlinner, A. Abbaspour-Tamijani, L. C. Kempel, and G. M. Rebeiz, "Switchable low-loss RF MEMS Ka-band frequency-selective surface," *IEEE Transactions on Microwave Theory and Techniques,* http://doi.org/10.1109/TMTT.2004.837148 vol. 52, no. 11, pp. 2474-2481, 2004.
[50] G. M. Rebeiz *et al.*, "Wafer-Scale Millimeter-Wave Phased-Array RFICs," in *Proc. IEEE Compound Semiconductor Integrated Circuit Symp. (CSICS)*, 2014/october, pp. 1-4.
[51] P. Rantakari *et al.*, "Wide-band radio frequency micro electro-mechanical systems switches and switching networks using a gallium arsenide monolithic microwave-integrated circuits foundry process technology," *Antennas Propagation IET Microwaves,* http://doi.org/10.1049/iet-map.2010.0434 vol. 5, no. 8, pp. 948-955, 2011.
[52] William H. Hayt, Jr. and J. A. Buck, *Engineering Electromagnetics*. McGraw-Hill, 2001.
[53] D. M. Pozar, *Microwave Engineering*, 4th ed. Hoboken: Wiley,, 2012, p. 1 online resource (756 p.). [Online]. Available: http://usf.eblib.com/patron/FullRecord.aspx?p=2064708.
[54] S. Kaleem, J. Kühn, R. Quay, and M. Hein, "A high-power Ka-band single-pole single-throw switch MMIC using 0.25 µm GaN on SiC," in *Proc. IEEE Radio and Wireless Symp. (RWS)*, 2015/january, pp. 132-134.
[55] R. S. Howell *et al.*, "Advances in the Super-Lattice Castellated Field Effect Transistor (SLCFET) for wideband low loss RF switching applications," in *Proc. IEEE MTT-S Int. Microwave Symp. (IMS)*, 2016/05, pp. 1-3.
[56] D. W. Kang, J. G. Kim, B. W. Min, and G. M. Rebeiz, "Single and Four-Element -Band Transmit/Receive Phased-Array Silicon RFICs With 5-bit Amplitude and Phase Control," *IEEE Transactions on Microwave Theory and Techniques,* http://doi.org/10.1109/TMTT.2009.2033302 vol. 57, no. 12, pp. 3534-3543, 2009.

[57] B. H. Ku *et al.*, "A 77 --81-GHz 16-Element Phased-Array Receiver With Beam Scanning for Advanced Automotive Radars," *IEEE Transactions on Microwave Theory and Techniques,* http://doi.org/10.1109/TMTT.2014.2354134 vol. 62, no. 11, pp. 2823-2832, 2014.

[58] M. Sterner, N. Roxhed, G. Stemme, and J. Oberhammer, "Static Zero-Power-Consumption Coplanar Waveguide Embedded DC-to-RF Metal-Contact MEMS Switches in Two-Port and Three-Port Configuration," *IEEE Transactions on Electron Devices,* http://doi.org/10.1109/TED.2010.2048239 vol. 57, no. 7, pp. 1659-1669, 2010.

[59] C. C. Cheng, B. Lakshminarayanan, and A. Abbaspour-Tamijani, "A Programmable Lens-Array Antenna With Monolithically Integrated MEMS Switches," *IEEE Transactions on Microwave Theory and Techniques,* http://doi.org/10.1109/TMTT.2009.2025422 vol. 57, no. 8, pp. 1874-1884, 2009.

[60] Y. Luo, K. Kikuta, Z. Han, T. Takahashi, A. Hirose, and H. Toshiyoshi, "An Active Metamaterial Antenna With MEMS-Modulated Scanning Radiation Beams," *IEEE Electron Device Letters,* http://doi.org/10.1109/LED.2016.2565559 vol. 37, no. 7, pp. 920-923, 2016.

[61] G. Mumcu, A. Dey, and T. Palomo, "Frequency-Agile Bandpass Filters Using Liquid Metal Tunable Broadside Coupled Split Ring Resonators," *IEEE Microwave and Wireless Components Letters,* vol. 23, no. 4, pp. 187-189, Apr 2013, doi: 10.1109/Lmwc.2013.2247750.

[62] O. L. Chlieh, W. T. Khan, and J. Papapolymerou, "L-band tunable microstrip bandpass filter on multilayer organic substrate with integrated microfluidic channel," in *Proc. IEEE MTT-S Int. Microwave Symp. (IMS2014)*, 2014/june, pp. 1-4.

[63] D. L. Diedhiou, R. Sauleau, and A. V. Boriskin, "Microfluidically Tunable Microstrip Filters," *IEEE Transactions on Microwave Theory and Techniques,* http://doi.org/10.1109/TMTT.2015.2435704 vol. 63, no. 7, pp. 2245-2252, 2015.

[64] S. J. Mazlouman, B. C. M. Chang, A. Mahanfar, R. G. Vaughan, and C. Menon, "Beam-Steering Antenna using Bending Fluidic Actuators," *IEEE Transactions on Antennas and Propagation,* http://doi.org/10.1109/TAP.2013.2273254 vol. 61, no. 10, pp. 5287-5290, 2013.

[65] A. Dey, R. Guldiken, and G. Mumcu, "Microfluidically Reconfigured Wideband Frequency-Tunable Liquid-Metal Monopole Antenna," *IEEE Transactions on Antennas and Propagation,* vol. 64, no. 6, pp. 2572-2576, Jun 2016, doi: 10.1109/Tap.2016.2551358.

[66] A. P. Saghati, J. S. Batra, J. Kameoka, and K. Entesari, "Miniature and Reconfigurable CPW Folded Slot Antennas Employing Liquid-Metal Capacitive Loading," *IEEE Transactions on Antennas and Propagation,* vol. 63, no. 9, pp. 3798-3807, Sep 2015, doi: 10.1109/Tap.2015.2447002.

[67] A. M. Morishita, C. K. Y. Kitamura, A. T. Ohta, and W. A. Shiroma, "A Liquid-Metal Monopole Array With Tunable Frequency, Gain, and Beam Steering," *IEEE Antennas and Wireless Propagation Letters,* http://doi.org/10.1109/LAWP.2013.2286544 vol. 12, pp. 1388-1391, 2013.

[68] C. K. Y. Kitamura, A. M. Morishita, T. F. Chun, W. G. Tonaki, A. T. Ohta, and W. A. Shiroma, "A liquid-metal reconfigurable Yagi-Uda monopole array," in *Proc. IEEE MTT-S Int. Microwave Symp. Digest (IMS)*, 2013/june, pp. 1-3.

[69] A. A. Gheethan, M. C. Jo, R. Guldiken, and G. Mumcu, "Microfluidic Based Ka-Band Beam-Scanning Focal Plane Array," *IEEE Antennas and Wireless Propagation Letters,* http://doi.org/10.1109/LAWP.2013.2294153 vol. 12, pp. 1638-1641, 2013.

[70] M. Li and N. Behdad, "Fluidically Tunable Frequency Selective/Phase Shifting Surfaces for High-Power Microwave Applications," *IEEE Transactions on Antennas and Propagation,* http://doi.org/10.1109/TAP.2012.2194645 vol. 60, no. 6, pp. 2748-2759, 2012.

[71] E. Erdil, K. Topalli, N. S. Esmaeilzad, O. Zorlu, H. Kulah, and O. A. Civi, "Microfluidic Reconfigurable Nested Split Ring-Regular Ring Transmitarray Unit Cell," *2014 Xxxith URSI General Assembly and Scientific Symposium (URSI GASS),* 2014.

[72] P. Sen and C. J. Kim, "A Liquid-Solid Direct Contact Low-Loss RF Micro Switch," *Journal of Microelectromechanical Systems,* vol. 18, no. 5, pp. 990-997, Oct 2009, doi: 10.1109/Jmems.2009.2029170.

[73] G. Mumcu, "Microfluidically reconfigurable antennas," in *Electromagnetic Waves*, *Developments in Antenna Analysis and Design: Volume 1*: Institution of Engineering and Technology, 2018, pp. 203-241. [Online]. Available: https://digital-library.theiet.org/content/books/10.1049/sbew543f_ch7

[74] R. C. Gough, A. M. Morishita, J. H. Dang, W. Hu, W. A. Shiroma, and A. T. Ohta, "Continuous Electrowetting of Non-toxic Liquid Metal for RF Applications," *IEEE Access,* http://doi.org/10.1109/ACCESS.2014.2350531 vol. 2, pp. 874-882, 2014.

[75] B. J. Lei, A. Zamora, T. F. Chun, A. T. Ohta, and W. A. Shiroma, "A Wideband, Pressure-Driven, Liquid-Tunable Frequency Selective Surface," *IEEE Microwave and Wireless Components Letters,* http://doi.org/10.1109/LMWC.2011.2162942 vol. 21, no. 9, pp. 465-467, 2011.

[76] T. J. Palomo and G. Mumcu, *Microfluidically Reconfigurable Frequency-Agile RF Filters With Wide Frequency Tuning Range And High Power Handling Capability*. [Online]. Available: http://ezproxy.lib.usf.edu/login?url=http://ezproxy.lib.usf.edu/login?url=http://scholarcommons.usf.edu/etd/6124.

[77] A. Dey and G. Mumcu, "Microfluidically Controlled Metalized Plate Based Frequency Reconfigurable Monopole for High Power RF Applications," *2015 IEEE International Symposium on Antennas and Propagation & Usnc/Ursi National Radio Science Meeting,* pp. 2299-2300, 2015.

[78] A. A. Gheethan, A. Dey, and G. Mumcu, "Passive Feed Network Designs for Microfluidic Beam-Scanning Focal Plane Arrays and Their Performance Evaluation," *IEEE Transactions on Antennas and Propagation,* vol. 63, no. 8, pp. 3452-3464, Aug 2015, doi: 10.1109/Tap.2015.2436441.

[79] E. González and G. Mumcu, "Mm-Wave Beam-Steering Focal Plane Arrays with Microfluidically Switched Feed Networks," *IEEE Transactions on Antennas and Propagation,* pp. 1-1, 2018, doi: 10.1109/TAP.2018.2874488.

[80] E. Gonzalez, G. Mumcu, and IEEE, "Mm-Wave 2D Beam-Steering Focal Plane Array with Microfluidically Switched Feed Network," in *2017 IEEE International Symposium on Antennas and Propagation & USNC/URSI National Radio Science Meeting*, 2017, pp. 907-908.

[81] C. Koo, B. E. LeBlanc, M. Kelley, H. E. Fitzgerald, G. H. Huff, and A. Han, "Manipulating Liquid Metal Droplets in Microfluidic Channels With Minimized Skin Residues Toward Tunable RF Applications," *Journal of Microelectromechanical Systems,* vol. 24, no. 4, pp. 1069-1076, Aug 2015, doi: 10.1109/Jmems.2014.2381555.

[82] S. Khan, N. Vahabisani, and M. Daneshmand, "A Fully 3-D Printed Waveguide and Its Application as Microfluidically Controlled Waveguide Switch," *IEEE Transactions on Components Packaging and Manufacturing Technology,* vol. 7, no. 1, pp. 70-80, Jan 2017, doi: 10.1109/Tcpmt.2016.2631545.

[83] R. Garg, I. Bahl, and M. Bozzi, "Microstrip Lines and Slotlines, Third Edition," *Microstrip Lines and Slotlines, Third Edition,* pp. 1-589, 2013.

[84] J.-S. G. Hong and M. J. Lancaster, *Microstrip filters for RF/microwave applications* (Wiley series in microwave and optical engineering). New York ; Chichester England: Wiley, 2001, pp. xii, 471 pages.

[85] A. J. King, J. F. Patrick, N. R. Sottos, S. R. White, G. H. Huff, and J. T. Bernhard, "Microfluidically Switched Frequency-Reconfigurable Slot Antennas," *Ieee Antennas and Wireless Propagation Letters,* vol. 12, pp. 828-831, 2013, doi: 10.1109/Lawp.2013.2270940.

[86] W. H. Tu and K. Chang, "Microstrip elliptic-function low-pass filters using distributed elements or slotted ground structure," *IEEE Transactions on Microwave Theory and Techniques,* vol. 54, no. 10, pp. 3786-3792, Oct 2006, doi: 10.1109/Tmtt.2006.882896.

[87] E. Gonzalez and G. Mumcu, "Low-Loss Wideband Feed Networks for High Gain Microfluidic Beam-Scanning Focal Plane Arrays," *2016 IEEE Antennas and Propagation Society International Symposium,* pp. 645-646, 2016.

[88] C. A. Balanis, *Antenna theory analysis and design*, 3rd ed. Hoboken, N.J.: Wiley-Interscience,, 2005, pp. 1 online resource (xvii, 1117 p.). [Online]. Available: http://usf.eblib.com/patron/FullRecord.aspx?p=699934.

[89] G. D. Massa, S. Costanzo, A. Borgia, F. Venneri, and I. Venneri, "Innovative dielectric materials at millimeter-frequencies," in *2010 Conference Proceedings ICECom, 20th International Conference on Applied Electromagnetics and Communications*, Sept 2010, pp. 1-4.

[90] P. Y. Cresson *et al.*, "1 to 220 GHz Complex Permittivity Behavior of Flexible Polydimethylsiloxane Substrate," *IEEE Microwave and Wireless Components Letters,* http://doi.org/10.1109/LMWC.2013.2295230 vol. 24, no. 4, pp. 278-280, 2014.

[91] Qorvo. "TGS4302 (27 - 46 GHz Ka Band High Power SPDT Switch)." Qorvo Inc. http://www.qorvo.com/products/p/TGS4302 (accessed.

[92] Texas Instruments. "LDC1614." http://www.ti.com/general/docs/lit/getliterature.tsp?genericPartNumber=ldc1614&fileType=pdf (accessed 2016).

[93] E. González and G. Mumcu, "Integrated Actuation of Microfluidically Reconfigurable mm-Wave SPST Switches," *IEEE Microwave and Wireless Components Letters,* vol. 29, no. 8, pp. 541-544, 2019, doi: 10.1109/LMWC.2019.2925889.

[94] E. González and G. Mumcu, "Microfluidic Switches with Integrated Actuation for Mm-Wave Beam-Steering Arrays," in *2019 IEEE International Symposium on Antennas and Propagation and USNC-URSI Radio Science Meeting*, 7-12 July 2019 2019, pp. 1871-1872, doi: 10.1109/APUSNCURSINRSM.2019.8889274.

[95] M. R. Moorefield, R. C. Gough, A. T. Ohta, and W. A. Shiroma, "An Electrically Actuated DC-to-11-GHz Liquid-Metal Switch," *IEEE Access,* vol. 6, pp. 1261-1266, 2018, doi: 10.1109/ACCESS.2017.2778184.

[96] Y. Shim, Z. Wu, and M. Rais-Zadeh, "A High-Performance Continuously Tunable MEMS Bandpass Filter at 1 GHz," *IEEE Transactions on Microwave Theory and Techniques,* vol. 60, no. 8, pp. 2439-2447, 2012, doi: 10.1109/TMTT.2012.2198228.

[97] B. Min and G. M. Rebeiz, "Ka-Band Low-Loss and High-Isolation Switch Design in 0.13-μmCMOS," *IEEE Transactions on Microwave Theory and Techniques,* vol. 56, no. 6, pp. 1364-1371, 2008, doi: 10.1109/TMTT.2008.921749.

[98] M. Wang, Y. Shim, and M. Rais-Zadeh, "A Low-Loss Directly Heated Two-Port RF Phase Change Switch," *IEEE Electron Device Letters,* vol. 35, no. 4, pp. 491-493, 2014, doi: 10.1109/LED.2014.2303972.

[99] J.-S. Hong and Wiley InterScience (Online service), *Microstrip filters for RF/microwave applications*, 2nd ed. Hoboken, N.J.: Wiley,, 2011, pp. 1 online resource (xvi, 635 p.). [Online]. Available: http://onlinelibrary.wiley.com/book/10.1002/9780470937297.

[100] M. Sanchez-Renedo, R. Gomez-Garcia, J. I. Alonso, and C. Briso-Rodriguez, "Tunable combline filter with continuous control of center frequency and bandwidth," *IEEE Transactions on Microwave Theory and Techniques,* vol. 53, no. 1, pp. 191-199, 2005, doi: 10.1109/TMTT.2004.839309.

[101] T. Cheng and K. Tam, "A Wideband Bandpass Filter With Reconfigurable Bandwidth Based on Cross-Shaped Resonator," *IEEE Microwave and Wireless Components Letters,* vol. 27, no. 10, pp. 909-911, 2017, doi: 10.1109/LMWC.2017.2746679.

[102] P. Jae-Hyoung, L. Sanghyo, K. Jung-Mu, K. Hong-Teuk, K. Youngwoo, and K. Yong-Kweon, "Reconfigurable millimeter-wave filters using CPW-based periodic structures with novel multiple-contact MEMS switches," *Journal of Microelectromechanical Systems,* vol. 14, no. 3, pp. 456-463, 2005, doi: 10.1109/JMEMS.2005.844849.

[103] D. Yingjie, P. Gardner, P. S. Hall, H. Ghafouri-Shiraz, and Z. Jiafeng, "Multiple-coupled microstrip hairpin-resonator filter," *IEEE Microwave and Wireless Components Letters,* vol. 13, no. 12, pp. 532-534, 2003, doi: 10.1109/LMWC.2003.819377.

[104] T. A. Anhoj, A. M. Jorgensen, D. A. Zauner, and J. Hübner, "The effect of soft bake temperature on the polymerization of SU-8 photoresist," *Journal of Micromechanics and Microengineering,* vol. 16, no. 9, pp. 1819-1824, 2006/07/28 2006, doi: 10.1088/0960-1317/16/9/009.

[105] M. Gaudet and S. Arscott, "A user-friendly guide to the optimum ultraviolet photolithographic exposure and greyscale dose of SU-8 photoresist on common MEMS, microsystems, and microelectronics coatings and materials," *Analytical Methods,* 10.1039/C7AY00564D vol. 9, no. 17, pp. 2495-2504, 2017, doi: 10.1039/C7AY00564D.

[106] Y. K. H. Cho, Hyun Doo; Park, Dong Kyu; Vijaya Sunkara, "Method for bonding substrates ", Patent Appl. KR20120053029A·2012-05-18, 2012.

[107] M. Bahrami, M. M. Yovanovich, and J. R. Culham, "Pressure Drop of Fully-Developed, Laminar Flow in Microchannels of Arbitrary Cross-Section," *Journal of Fluids Engineering,* vol. 128, no. 5, pp. 1036-1044, 2006, doi: 10.1115/1.2234786.

[108] C. Schuster *et al.*, "Performance Analysis of Reconfigurable Bandpass Filters With Continuously Tunable Center Frequency and Bandwidth," *IEEE Transactions on Microwave Theory and Techniques,* vol. 65, no. 11, pp. 4572-4583, 2017, doi: 10.1109/TMTT.2017.2742479.

[109] B. Rohrdantz, V. Schmidt, and A. F. Jacob, "Microstrip ring resonator based frequency reconfigurable band-pass filters at K-band," in *2014 20th International Conference on Microwaves, Radar and Wireless Communications (MIKON)*, 16-18 June 2014 2014, pp. 1-4, doi: 10.1109/MIKON.2014.6899907.

[110] A. Abbaspour-Tamijani, L. Dussopt, and G. M. Rebeiz, "Miniature and tunable filters using MEMS capacitors," *IEEE Transactions on Microwave Theory and Techniques,* vol. 51, no. 7, pp. 1878-1885, 2003, doi: 10.1109/TMTT.2003.814317.

[111] Z. Yang, D. Psychogiou, and D. Peroulis, "Design and Optimization of Tunable Silicon-Integrated Evanescent-Mode Bandpass Filters," *IEEE Transactions on Microwave Theory and Techniques,* vol. 66, no. 4, pp. 1790-1803, 2018, doi: 10.1109/TMTT.2018.2799575.

[112] P. Adhikari, W. Yang, and D. Peroulis, "A 20–26.5-GHz PCB Bandpass Filter Tuned With Contactless Tuners," *IEEE Microwave and Wireless Components Letters,* vol. 29, no. 8, pp. 513-515, 2019, doi: 10.1109/LMWC.2019.2922496.

[113] K. Choi, S. Courreges, Z. Zhao, J. Papapolymerou, and A. Hunt, "X-band and Ka-band tunable devices using low-loss BST ferroelectric capacitors," in *2009 18th IEEE International Symposium on the Applications of Ferroelectrics*, 23-27 Aug. 2009 2009, pp. 1-6, doi: 10.1109/ISAF.2009.5307566.

[114] A. P. Saghati, J. S. Batra, J. Kameoka, and K. Entesari, "A Miniaturized Microfluidically Reconfigurable Coplanar Waveguide Bandpass Filter With Maximum Power Handling of 10 Watts," *IEEE Transactions on Microwave Theory and Techniques,* vol. 63, no. 8, pp. 2515-2525, 2015, doi: 10.1109/TMTT.2015.2446477.

Appendix A: Microfluidically Switched Microstrip Line Circuit Model Optimization

To validate the accuracy of the circuit model representation of the microfluidically switched microstrip line from Chapter 3, the following analysis is carried out to: (i) choose the adequate parameters that are to be optimized, and (ii) determine the circuit model topology to be used. Specifically, for creating an accurate model for the ON-state of the switch, eight different optimization cases are considered and compared to the simulated EM response of the switch geometry. These cases are variations of the circuit model shown in Figure A.1 and summarized in Table A.1. Initially before starting the optimization, the parameters C_g and C_d are calculated from

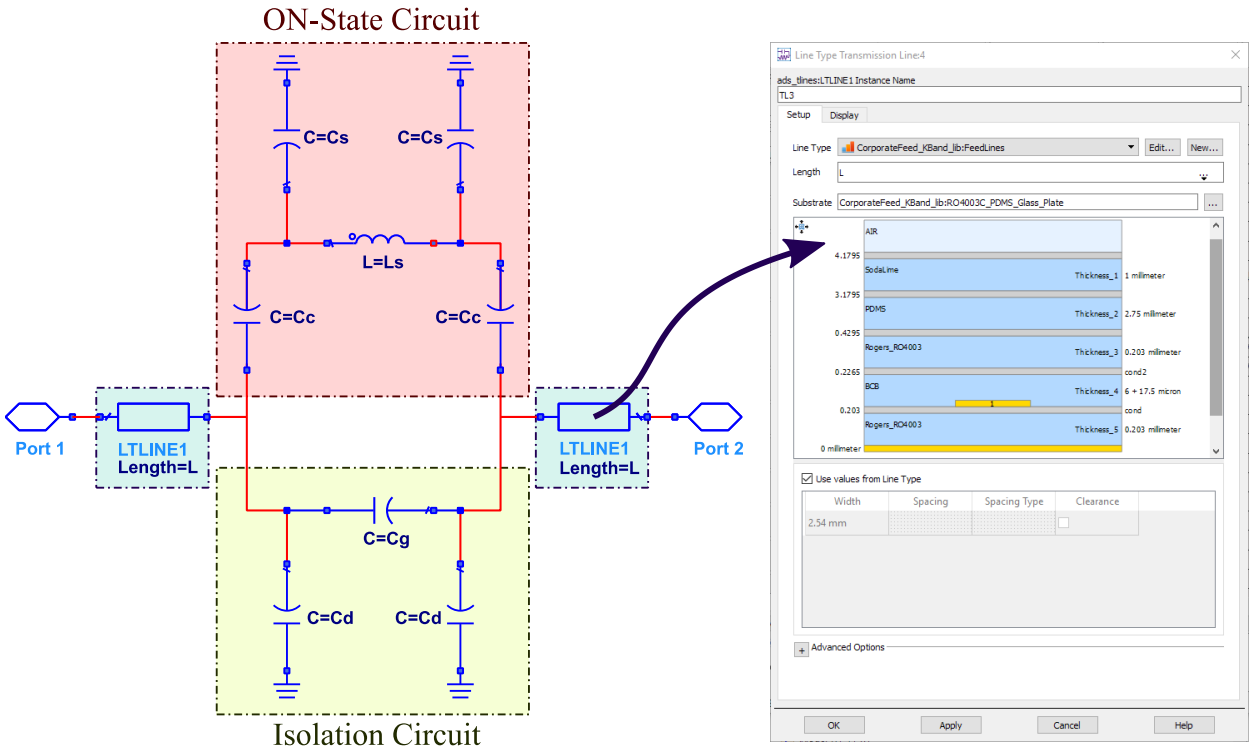

Figure A.1. General equivalent circuit model used for the optimization evaluation.

Table A.1. Optimization cases utilized for validation of circuit model accuracy.

Optimization Case	Isolation Circuit Connected	Short Length Transmission Lines at Input/Output	Parameters to be Optimized					
			C_C	L_s	C_s	C_g	C_d	L
A	No	Yes	✓	✓	✓	N/A	N/A	×
B	No	Yes	✓	✓	✓	N/A	N/A	✓
C	Yes	No	✓	✓	✓	✓	✓	N/A
D	No	No	✓	✓	✓	N/A	N/A	N/A
E	Yes	Yes	✓	✓	✓	×	×	×
F	Yes	Yes	✓	✓	✓	×	×	✓
G	Yes	Yes	✓	✓	✓	✓	✓	×
H	Yes	Yes	✓	✓	✓	✓	✓	✓

the open circuit condition of the switch (i.e. when there is no overlap between the SMP and the microstrip traces). These parameters represent the circuit in its OFF-state, and act as a representation of the switch isolation (referred to as Isolation Circuit in this Appendix). For the ON-state of the switch, the initial values for the parameters C_s and L_s are calculated from the short microstrip line equivalent circuit from [86], and C_C is calculated from the equivalent parallel plate capacitance developed between the SMP and microstrip line overlaps (as explained in Chapter 3). Additionally, a short length of transmission line (with length $L = L_{ov}$) is introduced to model the microstrip at the SMP-microstrip line overlap. This transmission line is modeled as a microstrip line in a multi-layered substrate through Keysight ADS Line Type Transmission Line component model as shown in Figure A.1. After calculating the parameters, the cases shown in Table A.1 are optimized and compared to the EM response of the switch. Primarily, the selected cases are variations of different parameter selections to be optimized, and the Isolation Circuit is either connected of disconnected from the model. The parameters C_C, L_s and C_s are always optimized because they are considered to be the main contributors to the ON-state switch behavior. The Isolation Circuit and the transmission line are either connected or disconnected and their

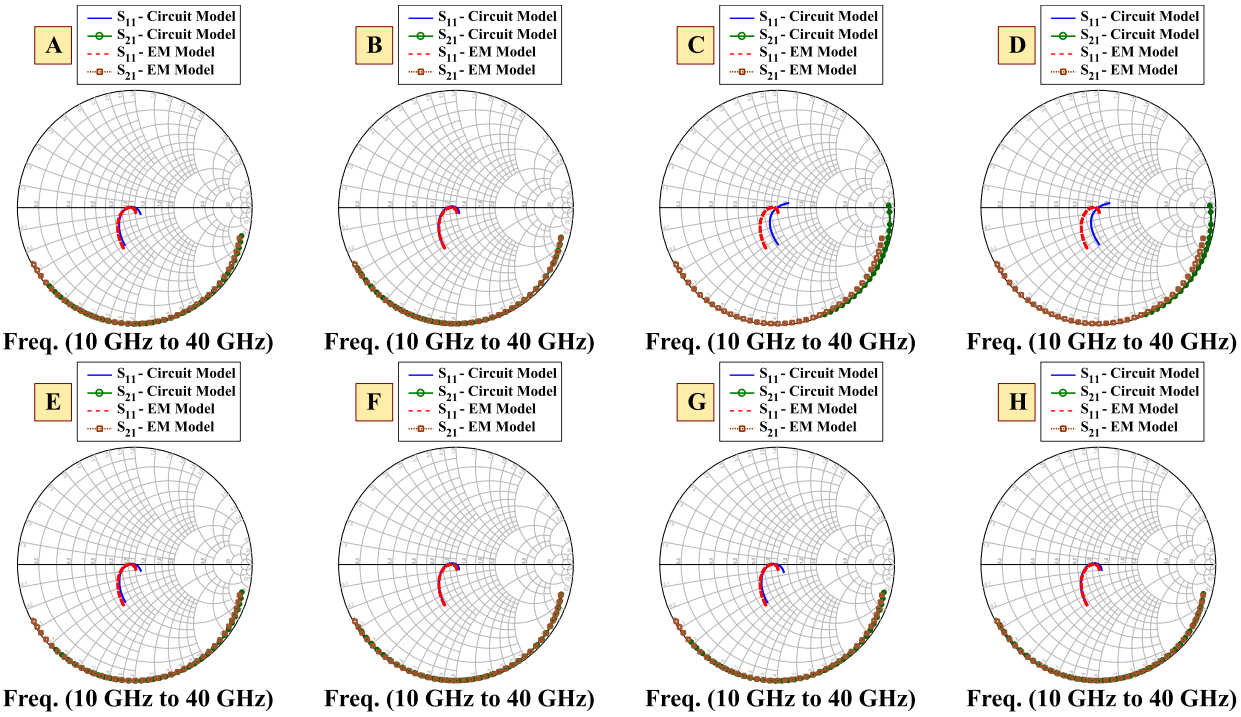

Figure A.2. Simulated responses of each optimized equivalent circuit model cases and their comparison the EM simulation of the microfluidically switched microstrip line of Chapter 3.

parameters (C_g, C_d and L) optimized or left unchanged to evaluate their contribution to the circuit model performance. The optimization is performed through the Quasi-Newton algorithm utilizing the optimization tools of Keysight ADS, and the optimization goals are to match the S-parameters of the circuit model to the EM-simulated model. The variation ($\Delta\%$) from initial calculated values to optimized values, the residual error of the optimization algorithm, and the corresponding behavior to the physical phenomena of the switch operation are considered to choose the adequate circuit model.

The optimized simulated responses of each case and their comparison to EM simulation are shown in Figure A.2 and the analysis summary is shown in Table A.2. Clearly, Case B offers minimal variations from the starting parameters values (C_c, L_s, C_s and L) after optimization, and the closest match to the EM response of the switch in its ON-state. When compared to C and D, it

can be seen that the omission of the short transmission line does not allow for accurate modeling of the switch in its ON-state. This verifies that the addition of the short length of transmission line and omitting the connection of the Isolation Circuit when the switch is in its ON-state, is the best performing model. Additionally from the results shown for Cases C, G and H, it is seen that when the Isolation Circuit is connected and C_d and C_g are optimized, the algorithm tends to bring down C_g and C_d to values close to zero. Indicating that there is no need for these parameters in the ON-state equivalent circuit of the switch. Similarly, by comparing cases B and F it is seen that C_s for case F is reduced by 95% and L increases by 44%, versus 61% and 38% for Case B. Therefore, Case B is chosen as the most accurate circuit model to represent the ON-state of the microfluidically switched microstrip line of Chapter 3. For the OFF-state, only the Isolation Circuit is used.

Table A.2. Summary of the optimization analysis for accurate circuit modeling.

	C_C (fF)	Δ%	L_s (pH)	Δ%	C_s (fF)	Δ%	C_g (fF)	Δ%	C_d (fF)	Δ%	L (mm)	Δ%	Residual Error
Initial Values	762.57	-	217.58	-	55.36	-	2.11	-	13.83	-	0.5	-	-
Optimization Cases													
A	906.86	19%	194.43	-11%	37.72	-32%	-	-	-	-	-	-	26.07
B	790.5	4%	150.38	-31%	21.32	-61%	-	-	-	-	0.69	38%	13.07
C	1032.57	35%	216.12	-1%	49.38	-11%	0.1	-95%	0.691	-95%	-	-	196.43
D	1033.16	35%	216.11	-1%	50.22	-9%	-	-	-	-	-	-	196.07
E	896.9	18%	193.94	-11%	21.61	-61%	-	-	-	-	-	-	28.42
F	780	2%	135.42	-38%	2.5	-95%	2.11	-	13.83	-	0.721	44%	12.2
G	891.86	17%	198.21	-9%	37.28	-33%	0.1	-95%	0.377	-97%	0.5	0%	32.72
H	780	2%	150.63	-31%	21.18	-62%	0.1	-95%	0.1	-99%	0.691	38%	12.79

Appendix B: Copyright permissions

Below are the permissions for the contents included in Chapters 3 through 5.

IEEE
Requesting permission to reuse content from an IEEE publication

A microfluidically switched feed network for beam-scanning focal plane arrays

Conference Proceedings: 2016 International Workshop on Antenna Technology (iWAT)

Author: Enrique Gonzalez

Publisher: IEEE

Date: Feb. 2016

Copyright © 2016, IEEE

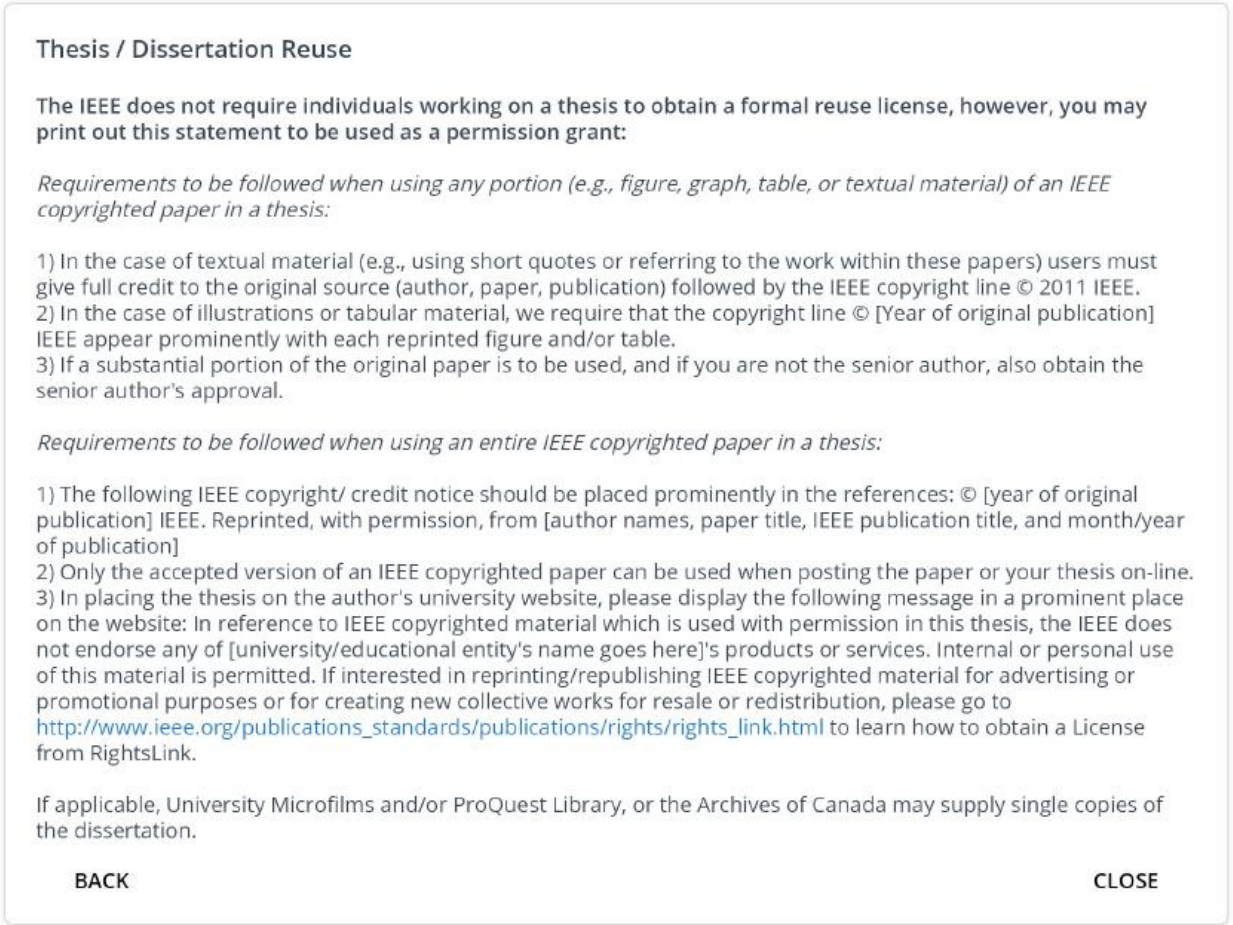

Thesis / Dissertation Reuse

The IEEE does not require individuals working on a thesis to obtain a formal reuse license, however, you may print out this statement to be used as a permission grant:

Requirements to be followed when using any portion (e.g., figure, graph, table, or textual material) of an IEEE copyrighted paper in a thesis:

1) In the case of textual material (e.g., using short quotes or referring to the work within these papers) users must give full credit to the original source (author, paper, publication) followed by the IEEE copyright line © 2011 IEEE.
2) In the case of illustrations or tabular material, we require that the copyright line © [Year of original publication] IEEE appear prominently with each reprinted figure and/or table.
3) If a substantial portion of the original paper is to be used, and if you are not the senior author, also obtain the senior author's approval.

Requirements to be followed when using an entire IEEE copyrighted paper in a thesis:

1) The following IEEE copyright/ credit notice should be placed prominently in the references: © [year of original publication] IEEE. Reprinted, with permission, from [author names, paper title, IEEE publication title, and month/year of publication]
2) Only the accepted version of an IEEE copyrighted paper can be used when posting the paper or your thesis on-line.
3) In placing the thesis on the author's university website, please display the following message in a prominent place on the website: In reference to IEEE copyrighted material which is used with permission in this thesis, the IEEE does not endorse any of [university/educational entity's name goes here]'s products or services. Internal or personal use of this material is permitted. If interested in reprinting/republishing IEEE copyrighted material for advertising or promotional purposes or for creating new collective works for resale or redistribution, please go to http://www.ieee.org/publications_standards/publications/rights/rights_link.html to learn how to obtain a License from RightsLink.

If applicable, University Microfilms and/or ProQuest Library, or the Archives of Canada may supply single copies of the dissertation.

BACK CLOSE

IEEE
Requesting permission to reuse content from an IEEE publication

Integrated Actuation of Microfluidically Reconfigurable mm-Wave SPST Switches

Author: Enrique González

Publication: IEEE Microwave and Wireless Components Letters

Publisher: IEEE

Date: Aug. 2019

Copyright © 2019, IEEE

Thesis / Dissertation Reuse

The IEEE does not require individuals working on a thesis to obtain a formal reuse license, however, you may print out this statement to be used as a permission grant:

Requirements to be followed when using any portion (e.g., figure, graph, table, or textual material) of an IEEE copyrighted paper in a thesis:

1) In the case of textual material (e.g., using short quotes or referring to the work within these papers) users must give full credit to the original source (author, paper, publication) followed by the IEEE copyright line © 2011 IEEE.
2) In the case of illustrations or tabular material, we require that the copyright line © [Year of original publication] IEEE appear prominently with each reprinted figure and/or table.
3) If a substantial portion of the original paper is to be used, and if you are not the senior author, also obtain the senior author's approval.

Requirements to be followed when using an entire IEEE copyrighted paper in a thesis:

1) The following IEEE copyright/ credit notice should be placed prominently in the references: © [year of original publication] IEEE. Reprinted, with permission, from [author names, paper title, IEEE publication title, and month/year of publication]
2) Only the accepted version of an IEEE copyrighted paper can be used when posting the paper or your thesis on-line.
3) In placing the thesis on the author's university website, please display the following message in a prominent place on the website: In reference to IEEE copyrighted material which is used with permission in this thesis, the IEEE does not endorse any of [university/educational entity's name goes here]'s products or services. Internal or personal use of this material is permitted. If interested in reprinting/republishing IEEE copyrighted material for advertising or promotional purposes or for creating new collective works for resale or redistribution, please go to http://www.ieee.org/publications_standards/publications/rights/rights_link.html to learn how to obtain a License from RightsLink.

If applicable, University Microfilms and/or ProQuest Library, or the Archives of Canada may supply single copies of the dissertation.

BACK CLOSE

IEEE
Requesting permission to reuse content from an IEEE publication

Low-loss wideband feed networks for high gain microfluidic beam-scanning focal plane arrays

Conference Proceedings:
2016 IEEE International Symposium on Antennas and Propagation (APSURSI)

Author: Enrique González

Publisher: IEEE

Date: June 2016

Copyright © 2016, IEEE

Thesis / Dissertation Reuse

The IEEE does not require individuals working on a thesis to obtain a formal reuse license, however, you may print out this statement to be used as a permission grant:

Requirements to be followed when using any portion (e.g., figure, graph, table, or textual material) of an IEEE copyrighted paper in a thesis:

1) In the case of textual material (e.g., using short quotes or referring to the work within these papers) users must give full credit to the original source (author, paper, publication) followed by the IEEE copyright line © 2011 IEEE.
2) In the case of illustrations or tabular material, we require that the copyright line © [Year of original publication] IEEE appear prominently with each reprinted figure and/or table.
3) If a substantial portion of the original paper is to be used, and if you are not the senior author, also obtain the senior author's approval.

Requirements to be followed when using an entire IEEE copyrighted paper in a thesis:

1) The following IEEE copyright/ credit notice should be placed prominently in the references: © [year of original publication] IEEE. Reprinted, with permission, from [author names, paper title, IEEE publication title, and month/year of publication]
2) Only the accepted version of an IEEE copyrighted paper can be used when posting the paper or your thesis on-line.
3) In placing the thesis on the author's university website, please display the following message in a prominent place on the website: In reference to IEEE copyrighted material which is used with permission in this thesis, the IEEE does not endorse any of [university/educational entity's name goes here]'s products or services. Internal or personal use of this material is permitted. If interested in reprinting/republishing IEEE copyrighted material for advertising or promotional purposes or for creating new collective works for resale or redistribution, please go to http://www.ieee.org/publications_standards/publications/rights/rights_link.html to learn how to obtain a License from RightsLink.

If applicable, University Microfilms and/or ProQuest Library, or the Archives of Canada may supply single copies of the dissertation.

BACK CLOSE

Microfluidic Switches with Integrated Actuation for Mm-Wave Beam-Steering Arrays

IEEE Requesting permission to reuse content from an IEEE publication

Conference Proceedings:
2019 IEEE International Symposium on Antennas and Propagation and USNC-URSI Radio Science Meeting

Author: Enrique González

Publisher: IEEE

Date: July 2019

Copyright © 2019, IEEE

Thesis / Dissertation Reuse

The IEEE does not require individuals working on a thesis to obtain a formal reuse license, however, you may print out this statement to be used as a permission grant:

Requirements to be followed when using any portion (e.g., figure, graph, table, or textual material) of an IEEE copyrighted paper in a thesis:

1) In the case of textual material (e.g., using short quotes or referring to the work within these papers) users must give full credit to the original source (author, paper, publication) followed by the IEEE copyright line © 2011 IEEE.
2) In the case of illustrations or tabular material, we require that the copyright line © [Year of original publication] IEEE appear prominently with each reprinted figure and/or table.
3) If a substantial portion of the original paper is to be used, and if you are not the senior author, also obtain the senior author's approval.

Requirements to be followed when using an entire IEEE copyrighted paper in a thesis:

1) The following IEEE copyright/ credit notice should be placed prominently in the references: © [year of original publication] IEEE. Reprinted, with permission, from [author names, paper title, IEEE publication title, and month/year of publication]
2) Only the accepted version of an IEEE copyrighted paper can be used when posting the paper or your thesis on-line.
3) In placing the thesis on the author's university website, please display the following message in a prominent place on the website: In reference to IEEE copyrighted material which is used with permission in this thesis, the IEEE does not endorse any of [university/educational entity's name goes here]'s products or services. Internal or personal use of this material is permitted. If interested in reprinting/republishing IEEE copyrighted material for advertising or promotional purposes or for creating new collective works for resale or redistribution, please go to http://www.ieee.org/publications_standards/publications/rights/rights_link.html to learn how to obtain a License from RightsLink.

If applicable, University Microfilms and/or ProQuest Library, or the Archives of Canada may supply single copies of the dissertation.

BACK CLOSE

IEEE
Requesting permission to reuse content from an IEEE publication

Millimeter-Wave Beam-Steering Focal Plane Arrays With Microfluidically Switched Feed Networks

Author: Enrique González

Publication: Antennas and Propagation, IEEE Transactions on

Publisher: IEEE

Date: Dec. 2018

Copyright © 2018, IEEE

Thesis / Dissertation Reuse

The IEEE does not require individuals working on a thesis to obtain a formal reuse license, however, you may print out this statement to be used as a permission grant:

Requirements to be followed when using any portion (e.g., figure, graph, table, or textual material) of an IEEE copyrighted paper in a thesis:

1) In the case of textual material (e.g., using short quotes or referring to the work within these papers) users must give full credit to the original source (author, paper, publication) followed by the IEEE copyright line © 2011 IEEE.
2) In the case of illustrations or tabular material, we require that the copyright line © [Year of original publication] IEEE appear prominently with each reprinted figure and/or table.
3) If a substantial portion of the original paper is to be used, and if you are not the senior author, also obtain the senior author's approval.

Requirements to be followed when using an entire IEEE copyrighted paper in a thesis:

1) The following IEEE copyright/ credit notice should be placed prominently in the references: © [year of original publication] IEEE. Reprinted, with permission, from [author names, paper title, IEEE publication title, and month/year of publication]
2) Only the accepted version of an IEEE copyrighted paper can be used when posting the paper or your thesis on-line.
3) In placing the thesis on the author's university website, please display the following message in a prominent place on the website: In reference to IEEE copyrighted material which is used with permission in this thesis, the IEEE does not endorse any of [university/educational entity's name goes here]'s products or services. Internal or personal use of this material is permitted. If interested in reprinting/republishing IEEE copyrighted material for advertising or promotional purposes or for creating new collective works for resale or redistribution, please go to http://www.ieee.org/publications_standards/publications/rights/rights_link.html to learn how to obtain a License from RightsLink.

If applicable, University Microfilms and/or ProQuest Library, or the Archives of Canada may supply single copies of the dissertation.

BACK CLOSE

Mm-wave 2D beam-steering focal plane array with microfluidically switched feed network

IEEE Requesting permission to reuse content from an IEEE publication

Conference Proceedings:
2017 IEEE International Symposium on Antennas and Propagation & USNC/URSI National Radio Science Meeting

Author: Enrique González

Publisher: IEEE

Date: July 2017

Copyright © 2017, IEEE

Thesis / Dissertation Reuse

The IEEE does not require individuals working on a thesis to obtain a formal reuse license, however, you may print out this statement to be used as a permission grant:

Requirements to be followed when using any portion (e.g., figure, graph, table, or textual material) of an IEEE copyrighted paper in a thesis:

1) In the case of textual material (e.g., using short quotes or referring to the work within these papers) users must give full credit to the original source (author, paper, publication) followed by the IEEE copyright line © 2011 IEEE.
2) In the case of illustrations or tabular material, we require that the copyright line © [Year of original publication] IEEE appear prominently with each reprinted figure and/or table.
3) If a substantial portion of the original paper is to be used, and if you are not the senior author, also obtain the senior author's approval.

Requirements to be followed when using an entire IEEE copyrighted paper in a thesis:

1) The following IEEE copyright/ credit notice should be placed prominently in the references: © [year of original publication] IEEE. Reprinted, with permission, from [author names, paper title, IEEE publication title, and month/year of publication]
2) Only the accepted version of an IEEE copyrighted paper can be used when posting the paper or your thesis on-line.
3) In placing the thesis on the author's university website, please display the following message in a prominent place on the website: In reference to IEEE copyrighted material which is used with permission in this thesis, the IEEE does not endorse any of [university/educational entity's name goes here]'s products or services. Internal or personal use of this material is permitted. If interested in reprinting/republishing IEEE copyrighted material for advertising or promotional purposes or for creating new collective works for resale or redistribution, please go to http://www.ieee.org/publications_standards/publications/rights/rights_link.html to learn how to obtain a License from RightsLink.

If applicable, University Microfilms and/or ProQuest Library, or the Archives of Canada may supply single copies of the dissertation.

BACK CLOSE

About the Author

Enrique González Carvajal was born in Valencia, Venezuela, in 1987. He received his B.Sc. degree in Electrical Engineering from the Universidad de Carabobo, Naguanagua, VE, in 2012, and his M.Sc. from the University of South Florida in 2018. He was an Instructor in the topics of Optical Communications and Guided Waves Systems Laboratory at his Alma Mater until the end of 2014, when he joined the University of South Florida. He joined USF to pursue his Ph.D. degree conducting research within Dr. Gokhan Mumcu's group. His research focus is on the realization of RF reconfigurable devices by using microfluidic technology, specifically filters, RF switches, antenna elements and antenna arrays, and filters. He has also developed around fifteen 3D visualizations for enhancing and complementing the teaching of electromagnetic theory in undergraduate courses. The visualizations cover topics of Vector Algebra, Vector Calculus and Electromagnetic Field Theory, Electrostatics and Time-Varying Fields through different interactive animations that can be displayed on 3D-enabled screens.